Experimental investigation of unconfined bluff body stabilised flames with vapourised kerosene fuels

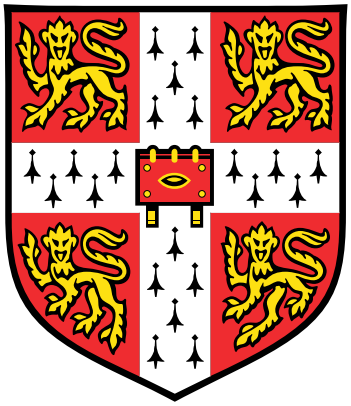

Rohit Singh Pathania

Department of Engineering
University of Cambridge

This thesis is submitted for the degree of
Doctor of Philosophy

Darwin College

March 2021

I would like to dedicate this thesis to my loving wife Tanvi Sambyal ...

Declaration

This thesis is the result of my own work and includes nothing which is the outcome of work done in collaboration except as declared in the Preface and specified in the text. I further state that no substantial part of my thesis has already been submitted, or, is being concurrently submitted for any such degree, diploma or other qualification at the University of Cambridge or any other University or similar institution except as declared in the Preface and specified in the text. It does not exceed the prescribed word limit for the relevant Degree Committee.

Rohit Singh Pathania
March 2021

Abstract

Experimental investigation of unconfined bluff body stabilised flames with vapourised kerosene fuels

Rohit S. Pathania

To achieve low emission targets, combustion technologies have increasingly implemented lean premixed flames as they facilitate low NO_x and soot emissions. In most modern transport vehicles, combustion occurs under highly turbulent conditions. However, stabilizing lean premixed flames within the high Reynolds number conditions of practical devices is difficult because they are prone to blow-off, resulting in reduced efficiency or worse, engine failure. Thus, there is a need to understand the underlying physics of lean blow-off (LBO) so that accurate, yet computationally tractable models can be developed to predict its onset.

In this dissertation, the lean blow-off limits and turbulent flame structure of unconfined, pre-vapourised liquid fuels stabilised on a bluff body burner were investigated at two conditions: far from blow-off ($\phi/\phi_{BO} = 1.20$) and close to blow-off ($\phi/\phi_{BO} = 1.01$). Four different fuels were considered, two of which comprised of a single component (ethanol and heptane) while the other two were multi-component kerosene blends (A2 and C1 from the National Jet Fuel Combustion Programme). The lean blow-off limit indicates that the ethanol and heptane flames are more resilient to blow-off than the kerosene fuels. To facilitate comparisons with gaseous-fueled flames, results were also obtained from methane flames. Furthermore, a correlation based on a Damköhler number (*Da*), which is proportional to the laminar flame speed, does not lead to the successful collapse of the different fuels, indicating that the *Da* correlations based on laminar flame speed are not applicable.

The flame structure and lean blow-off behaviour were studied with OH* chemiluminescence and high-speed (5 kHz) OH-PLIF imaging. Additionally, CH_2O-PLIF imaging was used to assess the impact of fuel composition on the CH_2O-layer thickness. As the flame approached LBO, fragmentation was observed downstream. The two sides of the flame merged at the axis, pockets of OH and CH_2O were found in the recirculation zone (RZ), and eventually, the individual fragments were extinguished. The CH_2O seemed to enter the RZ from downstream early in the LBO process, with reactants following suit at

times closer to LBO. During LBO, the integrated OH* signal decreased slowly to zero. The duration of this transition was $\sim$25 (d/U_{BO}) in the methane and ethanol flames and $\sim$60 (d/U_{BO}) in the flames operated with heptane and the two kerosenes (where d is the bluff-body diameter and U_{BO} the LBO velocity). This large difference could be due to the re-ignition of partially-quenched fluid inside the RZ during the LBO event. Additionally, for the same bulk velocity, the kerosene flames blow-off at higher equivalence ratios than the single-component fuelled flames, possibly due to the higher Lewis number and lower extinction strain rates of these fuels. The results suggest that the blow-off mechanism is qualitatively similar for each of the fuels; however, the complex chemistry associated with heavy hydrocarbons appears to result in a prolonged LBO event.

The average OH* chemiluminescence images of the ethanol and heptane flames are qualitatively similar to those of methane: the flame brushes of both exhibit an M-shape when close to blow-off. In contrast, the distribution of OH* signal in the kerosene flames is primarily concentrated in regions further downstream of the bluff body. Also, whilst close to blow-off, the flame fronts on opposite sides of the bluff body in the downstream region of the recirculation zone merge to create a seemingly closed region above the bluff body for all four flames. The OH-PLIF images of ethanol at far from blow-off display a higher intensity of OH-LIF signal along the annular jets, while the OH-LIF signal was more distributed in the heptane- and kerosene-fueled flames. Regardless of the fuel used, close to blow-off the flame becomes shorter with peak OH-LIF signal intensities lying inside the RZ. All four fuels showed a decrease in flame surface density (Σ_{2D}) and broadening of the 2-D curvature PDFs as their blow-off limits were approached. An increase in local turbulent consumption speed was observed in the downstream region at close to blow-off. No significant variation in Σ_{2D}, curvature PDF, and local turbulent consumption speed was observed between the different fuel types. The average CH_2O-layer thickness was larger than the computed laminar flame value by a factor of two and six for conditions far from and close to blow-off, respectively. Moreover, when LBO is approached, an increased amount of CH_2O-LIF signal is observed within the recirculation zone, which is consistent with prior results obtained from methane flames. Overall, the thickness and appearance of the CH_2O-layers are qualitatively similar between the single- and multi-component fuels; however, the kerosene fuels tend to exhibit wider CH_2O-layers. Additionally, these fuels tend to possess more isolated pockets of CH_2O-LIF signal within the recirculation zone, suggesting that a considerable amount of partially-combusted fluid enters it. High-speed particle image velocimetry was performed to measure the local velocity fields and place these flames on the turbulent premixed regime diagram. It was observed that, regardless of fuel type, conditions close to blow-off occupy the same region on the regime diagram.

Ultimately, this effort's results highlight the influence fuel-type has on the LBO of bluff-body stabilized flames. Moreover, this work indicates that the LBO behavior of flames produced with complex hydrocarbon fuels can not be fully understood by high-temperature chemistry concepts such as laminar flame speed.

Acknowledgements

My sincerest thanks go to Professor E. Mastorakos, who guided, motivated, and supported me throughout my Ph.D. Without a doubt, he is the best supervisor a Ph.D. student could hope for. He provided guidance and suggestions in a way that allowed me to become a free-thinking scientist. It has been a privilege to be Professor Mastorakos' student for the past three and a half years.

I wish to thank Professor Nedunchezhian Swaminathan and Professor Yannis Hardalupas (Imperial College) for taking the time to examine this work and for their insightful comments and suggestions during the viva.

My special thanks to Dr. Aaron Skiba for all of the discussions and extensive help with experiments and understanding different diagnostic techniques. The lab expertise of Ingrid and Roberto was greatly appreciated, as were the never-ending discussions about science and non-technical topics. The 1D Cantera simulations and scientific discussions would not have been possible without Savvas Gkantonas. I appreciate Jenna's willingness to jump into a kerosene discussion whenever possible. I am grateful for the conversations and emotional support I have received from colleagues and friends in the Department of Engineering. I would especially like to thank the Hopkinson lab technicians for their patience and help. The work presented here would not be possible without the efforts of contributors like you. Additionally, I wish to thank Peter Benie for all the support he provided with the electronics and computing facilities. To close, I would like to thank my fellow Ph.D. students at the Hopkinson lab, each of whom has helped me in some way, for which I am grateful.

For funding this research, I would like to thank Cambridge Trust and SERB India. If not for their generosity, none of this would have been possible. Thank you Darwin College for your help throughout my PhD.

Outside of research and academia, I am grateful to many individuals for providing support and social life at Cambridge. Thank you Zeynep, LuzMa, and Mirlinda for all your support

and delicious food. Thanks to Shivankar and Khemka for a wonderful trip to Scotland. Thanks to Mona, Arjun, Kanwar, Shikar, and Swapan for helping me out when I needed it.

I can never express enough appreciation to the love of my life, Tanvi, for the support and help you have provided and the love you have shown me. This would not have been possible without your support. I must thank you most of all for believing in me, especially when I had little to no confidence in myself. Tanvi, I am grateful and I love you very much for everything you did and for everything you do.

My parents, Rasal Singh and Vijay Kumari, deserve my deepest thanks for their love and support throughout my life. You've both given me the courage and strength to pursue my dreams. It was my mother-in-law, Neeru Sambyal, who motivated me and taught me the importance of remaining positive in difficult times. To my father-in-law, Sukhdev Singh Sambyal, for all the love and faith you shared with me, which has positively impacted my life. Your presence in our lives will continue even though you are not with us anymore.

To conclude, I would like to thank all my cousins, my older brother (Satish), and my sister-in-law (Mamta) who believed in me. Thank you for being part of my life, my little niece Akristi. Dixit Sambyal, thanks for teaching me about finance. Thank you, Bhumika Singh, for all the discussion we had about life. I'd like to thank my dear brother-in-law Abhyuday for his love. My high school and college friends are also to be thanked for all their support. I wish to thank Manish Sharma, Sanjeev, Ishan Mahajan, Ishan Jasrotia, Sahil Sharma, Amit Thakur, Deepak, Govind, Ashish, Mukesh and many others for their loyalty. I always think about you, even though I may not see you regularly.

List of publications

The results of this dissertation has been published in journals and presented at conferences.

Journal Papers:

- Rohit S. Pathania, Aaron W. Skiba, Epaminondas Mastorakos, Experimental investigation of unconfined turbulent premixed bluff-body stabilized flames operated with vapourised liquid fuels. *Combustion and Flame*, 2021.
- Rohit S. Pathania, Aaron W. Skiba, Roberto Ciardiello, Epaminondas Mastorakos, Blow-off mechanisms of turbulent premixed bluff-body stabilized flames operated with vapourised kerosene fuels. *Proceedings of the Combustion Institute*, 2020.
- Rohit S. Pathania, Aaron W. Skiba, Jenni A. M. Sidey-Gibbons, Epaminondas Mastorakos, Lean blow-off scaling of turbulent premixed bluff-body flames of vapourised liquid fuels. *Journal of Propulsion and Power*, 2020.

Conference Proceedings and Presentations:

- Rohit S. Pathania, Aaron W. Skiba, Jenni A. M. Sidey-Gibbons, Epaminondas Mastorakos, Blow-off mechanism in a turbulent premixed bluff-body stabilized flame with pre-vaporized fuels. *AIAA Scitech Forum*, 2019.
- Rohit S. Pathania, Aaron W. Skiba, Epaminondas Mastorakos, Experimental study of turbulent premixed pre-vapourised bluff body stabilised flames: Flame-front features near lean blow off. *11th Mediterranean Combustion Symposium*, 2019.
- Rohit. S. Pathania, Aaron W. Skiba, Roberto Ciardiello, Ingrid El Helou, Epaminondas Mastorakos, Aerodynamic features of bluff-body stabilised premixed flames near extinction. *13th International ERCOFTAC symposium, ETMM*, 2020. To be presented.

Table of contents

List of figures

List of tables

Nomenclature

Roman Symbols

$\bar{c}$	Mean progress variable
D	Diameter (mm)
d	Bluff body diameter (mm)
Da	Damköhler number (Eq. 1.1)
Da_{bo}	Damköhler number at blow-off (Eq. 2.1)
D_C	Characteristic dimension
E	Energy
S_{lam}	Extinction strain rate
F_c	Degree of Fragmentation
K	Karlovitz stretch factor $(0.125(u'/S_L)^2(Re_t)^{-1/2}$)
Ka	Karlovitz number (Eq. 1.9)
L_r	Recirculation zone length
L_T	Integral length scale
m_{air}	Mass flow rate of air
u'_{max}	Contour of maximum velocity fluctuations
p	Pressure
ϕ_{ext}	Blow-off fuel-air ratio
Re_T	Turbulent Reynolds number (Eq. 1.8)
$\bar{S}_{max}$	Contour of maximum shear layer
S_L	Laminar flame speed
$S_{L,bo}$	Laminar flame speed at blow-off
$S_{T,LC}$	Local turbulent consumption speed
T	Temperature
T_{ad}	Adiabatic temperature
t_B	Critical ignition delay time
T_{inlet}	Inlet temperature
u	Axial velocity
$u^{'}$	Velocity fluctuations
U_b	Bulk velocity
U_{bo}	Blow-off velocity
V	Volume of the combustion zone
v	Radial velocity
z	Progress variable

Greek Symbols

δ_l	Laminar flame thickness
$\delta(l)_{CH_2O}$	Laminar CH_2O thickness
$\delta(l)^*_{CH_2O}$	Corrected laminar CH_2O thickness
D_T	Turbulent diffusivity defined as $u'L_T$

$\eta*$	Kolmogorov length scale
κ	Local curvature
λ	Taylor microscale
λ_{length}	Wave length
D^*	Molecular diffusivity
ν	Kinematic viscosity
ϕ	Equivalence ratio
ϕ_{bo}	Equivalence ratio at blow-off
$\delta_{RZ,L}$	Laminar reaction layer thickness
Σ_{2D}	2-D FSD
τ_{chem}	Chemical time scale (Eq. 1.7)
$\tau_{\eta}*$	Kolmogorov time scale
τ_{flow}	Flow time scale
τ_{ext}	Extinction duration

Subscripts

$2D$	Two dimensional
b	Bulk
bo	Blow-off
ext	Extinction
l	Laminar
p	Particle
T	Turbulent

Acronyms / Abbreviations

ATJ	alcohol-to-jet
BP	Bandpass filter
CCD	Charge-coupled device
CMOS	Complementary metal–oxide–semiconductor
DCN	Derived cetane number
DNS	Direct numerical simulation
DRZ	Distributed reaction regime
FSD	Flame surface density
HRR	Heat release rate
ICCD	Intensified charge-coupled device
LBO	Lean blow-off
Le	Lewis number
LES	Large-eddy simulation
LIF	Laser-induced fluorescence
mfc	Mass flow controller
PDA	Phase Doppler Anemometry
PDF	Probability density function
PID	Proportional-integral-derivative
PIV	Particle image velocimetry
PLIF	Planar laser-induced fluorescence
PMT	Photomultiplier tube
PSF	Point spread function
RANS	Reynolds-averaged Navier-Stokes
RMS	Root mean square
RZ	Recirculation zone
SNR	Signal to noise ratio
UV	Ultra-Violet

Chapter 1

Introduction

1.1 Motivation

Stabilisation of lean premixed flames is of considerable importance for next-generation gas turbine combustors [1–3].This is due to the fact that lean that lean premixed flames operate at lower temperatures than richer premixed or non-premixed flames, which facilitates a substantial reduction in total NOx production [4]. However, because premixed flames are prone to blow-off, this renders the design and development of practical devices that can robustly stabilise premixed flames over a broad range of conditions [5]. One common way to stabilise these flames is by creating a wake or recirculation zone (RZ) behind a bluff body. RZ facilitates combustion within high-speed flows by 1) creating a region of relatively low velocity and 2) providing a continuous source of burnt products to back-support the flames [6, 7]. Stabilisation of the flame using a bluff body has been used in various propulsion and industrial applications. Some of the common applications are in industrial burners, steam generators, and turbojet afterburner systems. Additionally, they are used in characterisation of the turbulent flame or in computational studies [8–15]. Fig. 1.1 shows the structure of the flow field behind a conical bluff body, where 'd' is the bluff body diameter, and 'D' is the annular diameter. The flame stability also depends on the flow velocities and mixture equivalence ratio. The process by which the flame anchors behind the bluff body involves continuous interaction of hot products in the RZ with the combustible mixture in the shear layer. Flame extinction (blow-off) is observed when the flow velocities or equivalence ratios are extended beyond stable operating conditions [16].

In gas turbine engine configurations, the lean blow-off limit plays a critical role in its diverse operating range. Thus, a gas turbine engine designed for low NOx production needs to be operated with a controlled lean fuel/air ratio [7, 17]. A significant amount of research has been done to study the blow-off of single-component fuels [18–21], which is a long-

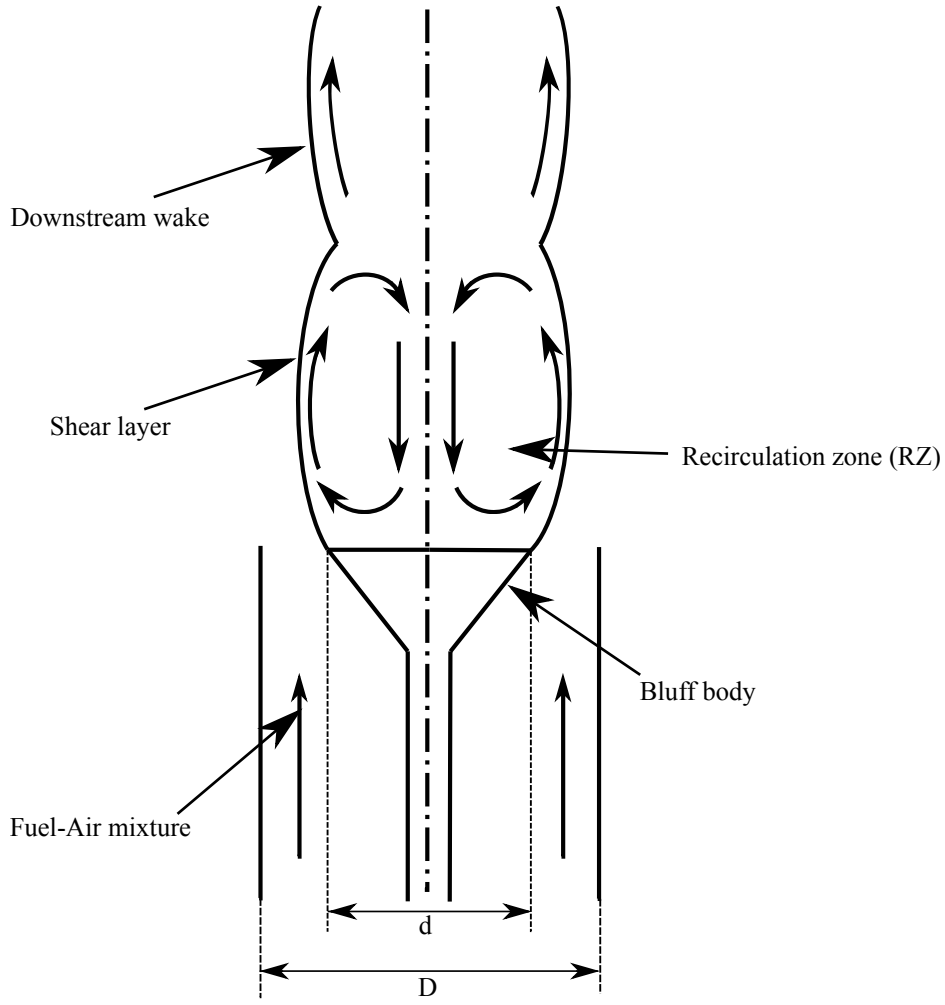

Fig. 1.1 Schematic showing the structure of flow field around a typical conical bluff-body burner.

standing issue within the premixed combustion community [22, 23]. Early lean blow-off (LBO) investigations with gaseous fuels in bluff body burner configurations focused on the development of empirical and semi-empirical co-relations, correlating blow-off limits as a function of flow velocity, equivalence ratio, fuel type, blockage ratio, bluff body shape, pressure, and temperature [24, 23, 25, 26]. These theories associated blow-off as a balance of energy and mass with hot recirculating gaseous [26, 27] or longer chemical time scale compared to the fluid mechanical time scale. The comprehensive review by Shanbhogue et al. [23] on the LBO of bluff body stabilised flames summarises the blow-off phenomenon into two stages: localized extinction and wake alteration. They discuss the blow-off dynamics at various Reynolds numbers. A correlation is formulated based on the blow-off data in the literature showing the dependence of blow-off on Damköhler number (Da) correlations

based on laminar flame speed (S_L). Kariuki et al. [28] validated the *Da*-based correlation in bluff body premixed flame with methane for various bluff body diameters and bulk velocities. They found that the correlation based on *Da* collapses well for bluff body stabilised methane flames, indicating blow-off depends on the laminar flame speed.

Further understanding of the structure of turbulent premixed flames near blow-off and the transient behavior of such flames during blow-off have been extensively studied via OH* chemiluminescence and planar laser-induced fluorescence (PLIF) imaging of OH and CH_2O [17, 23, 29–32]. From these experimental studies, it can be deduced that the flame changes shape as it approaches blow-off. The experiments of Kariuki et al. [17, 29] suggested that reactions occur within the recirculation zone (RZ) just before blow-off. Dawson et al. [32] and Kariuki et al. [29], who investigated methane flames, noticed significant extinction in the downstream region of the RZ, which led to the eventual advection of partially-burnt and unburnt reactants into the RZ, further destabilising flame-fronts near the shear layer.

Local extinction and other structural features of turbulent premixed flames have been extensively investigated [8, 33–35]. Several bluff body geometries have been studied, including conical, rod stabilized, and disc shape [17, 29–32, 36, 37]. Kariuki et al. [17, 29, 36] studied the flame structure in a conical bluff-body burner. As their flames approached blow-off [29], they found that the flame fronts on either side of the burner merged at the axis. After such merging, fresh reactants were observed to enter the RZ from downstream locations. Additionally, as LBO was approached, the flame fronts were observed to retreat to the RZ, which is likely a consequence of reduced burning rate and enhanced local extinction. In the same burner, Kariuki et al. [36] estimated the heat release rate (HRR) via the pixel-by-pixel multiplication of OH- and CH_2O-PLIF images. They observed fragmentation of heat release (HR) regions in the downstream areas of the RZ. Furthermore, they demonstrated that regions void of OH within the RZ are often filled with CH_2O, and HRR is found on the boundary of isolated OH pockets. Chaudhuri et al. [31] observed a similar flame structure in their disc-shaped bluff body burner operated with propane. They also reported the flame's recession into the RZ, but this time due to extinction in the shear layer due to local high strain rates.

While most of the studies mentioned above considered simple gaseous fuels, practical combustion engines typically operate with complex liquid fuels. For this reason, recent studies have begun to investigate the influence of turbulence and fuel effects on heavy hydrocarbon-fueled flames. For example, Carbone et al. [38] experimentally studied the effect of fuel properties on the global and local flame structure. They considered hydrocarbon fuels ranging from C_1 to C_8 with *Le* from 0.97 to 3.13 at very high *Ka*. They speculated that the lower *Le* of lean methane flames results in higher reactivity, rendering such flames more resilient to quenching than flames with higher *Le*. The effect of *Le* was also studied by

Trabold et al. [39] in turbulent premixed vaporised jet-flames with alcohol fuel from C_1 to C_4. They found that the stability of alcohol flames increases with the decreasing molecular weight of the fuels. Additionally, a recent DNS study [40] found that flame-front wrinkling was suppressed in high-*Le* flames, resulting in a considerable reduction of the turbulent flame speed.

Understanding of turbulent-flame interactions has been primarily derived from studies of gaseous fuels. Yet, as mentioned above, recent experimental, LES, and DNS results highlight differences between flames produced by burning simple and more complex fuels [38, 40, 41]. Moreover, knowledge of the fuel type influencing the LBO behaviour of turbulent premixed bluff body stabilised flames is lacking. Thus, there is a need to experimentally study flames produced by heavy hydrocarbons with complex chemistry and $Le > 1$. Additionally, the main constituents of kerosene fuel are saturated alkanes, cycloalkanes, aromatics, olefins, and branched-chain paraffins, as well as ring-shaped cycloparaffins. In contrast, single-component fuels are only composed of alkanes or alkyls [42].

The kerosenes used in this work were standardised fuels coded as "A2", which is Jet-A and "C1", an alternative Gevo ATJ kerosene, from the National Jet Fuel Combustion Program led by the Federal Aviation Administration, the U.S. Air Force Laboratory, and NASA. The program's objectives are to streamline the process of ASTM jet fuel certification for alternative aviation fuels and develop testing and modeling capabilities that can improve the understanding of the impact of alternative fuel chemical composition and physical properties on combustion [43]. The deployment of alternative jet fuels relies on the successful approval of the specification of the fuel by ASTM International. The specification includes the production process of the fuels, along with laboratory, combustor rig, and engine testing of these fuels. The following three combustion features define the process of testing these fuels in engines: lean blow-out (LBO), altitude relight, and cold start.

Alternative jet fuels, also called drop-in fuels, are composed of hydrocarbons produced from alternative sources, such as bio-derived feedstocks. The drop-in fuel can be used in the current engines as they provide identical performance to petroleum-derived fuels. Also, alternative jet fuels produce low emissions, especially concerning particulate matter. Thus, reducing the aviation contribution to climate change and surface air quality [44]. Because of the above-stated benefits of alternative fuels, U.S government has set a goal of carbon-neutral growth for U.S. jet aviation using 2005 emissions as a baseline by 2020 [45]. The University of Cambridge is contributing to the area of bluff body stabilized flames.

With the increasing emphasis on the use of alternative jet fuels [43], it is becoming very important to obtain a stable flame with these fuels and find the lean global blow-off limits in a turbulent flow. This work meets that need by considering premixed vapourised kerosene

flames stabilised by an unconfined bluff-body burner similar to that in Refs. [29, 31**?** , 32, 36]. This dissertation results help identify the extent to which previous findings on simple fuels can be extrapolated to more complex ones.

1.2 Outline

This dissertation aims to study the influence of fuel type on flame structure, and the LBO behaviour of turbulent premixed bluff body stabilised flames.

The content of this dissertation is organised as follows:

Chapter I: Motivation, Literature review and Objectives This chapter focuses on discussing the blow-off studies and describing the dissertation objectives. Before discussing the blow-off studies of turbulent bluff body stabilised flames, a brief review of the laminar premixed flame's properties is provided. After that, a review of the studies relevant to the present work is discussed. Finally, the chapter concludes with the specific objectives of this dissertation.

Chapter II: Experimental details and methodology The purpose of this chapter is to introduce the experimental techniques used in this study. First, details regarding the critical dimensions of the burner and vaporiser are provided. Then the optical diagnostics techniques used to characterise the flow-field and flame structure are presented. Lastly, routines employed to process the images to obtain meaningful information from the flame structure images are discussed. The method employed to obtain flame surface density (FSD), 2D-curvature, and velocity data is presented.

Chapter III: Laminar flame simulation The results from the unstrained and strained laminar flame simulation are presented in this chapter. The calculated laminar flame speed, flame thickness, CH_2O-layer thickness, and species distribution in the laminar flame with methane, ethanol, heptane, A2, and C1 are presented. Additionally, the extinction strain rates calculated from the twin flame simulation for all five fuels mentioned above are presented. The results from laminar flame simulation were used in Chapter IV, V, and VI.

Chapter IV: Lean blow-off limits and scaling The stability limits for methane, ethanol, heptane, A2, and C1 are presented. The stability limits are correlated with the *Da* correlation based on laminar flame speed. Additionally, the extinction strain calculated from the twin flame configuration is plotted against the blow-off velocities. The extinction strain rates obtained from the twin strained flame simulation are used to calculate the Karlovitz stretch factor, and the role of extinction and *Le* is explored in governing the LBO in this section.

Chapter VI: Blow-off duration and mechanism In this Chapter, the blow-off mechanism and blow-off duration is presented. Firstly, the flame structure during blow-off is reported with OH*-imaging. The OH* images were used to calculate the blow-off duration. The rest of the Chapter presents the species distribution inside the RZ during blow-off with A2 flame. The OH-PLIF, CH_2O-PLIF, and Fuel-PLIF were used to capture the species distribution inside RZ. A2 flame is considered as it is the most complex of all fuels considered in this study. Lastly, results obtained are contrasted against those obtained from methane and ethylene flames in previous works [32, 29, 36, 17], highlighting differences between the flame structures near LBO.

Chapter V: Flame structure In this chapter, the detailed flame structure was investigated with 5 kHz OH* chemiluminescence, OH-PLIF imaging, and 10 Hz CH_2O-PLIF imaging. Two conditions were investigated: far from blow-off ($\phi/\phi_{BO} = 1.20$) and close to blow-off ($\phi/\phi_{BO} = 1.01$) at a bulk airflow velocity of 23.5 m/s. Four different fuels were considered, two of which comprised a single component (ethanol and heptane), while the other two were multi-component kerosene blends (A2 and C1). The Chapter is organised as follows: i) Instantaneous and averaged OH*chemiluminescence images are presented with all four fuels. The results are compared with previous studies then Abel transformed images are presented. ii) The flame structure obtained from OH-PLIF images is reported, and the effect of turbulent intensities on the flame structure is discussed. From the OH-PLIF images, average reaction progress variable images were calculated and discussed. These images were used to evaluate the flame surface density (FSD)and 2-D curvature at far from and close to blow-off conditions. The local estimate of the average consumption speed was also reported in this Chapter. iii) The CH_2O-thickness was evaluated from CH_2O images, and the results have been complied into PDF. Lastly, the chapter presented the velocity field's global features in non-reacting and vapourised heptane flames under stable and near blow-off conditions. Additionally, turbulent intensity and turbulent length scale L_T are evaluated at different locations from the burner exit.

Chapter VII: Discussion In this chapter, the results obtained from OH*, OH-PLIF, CH_2O-PLIF, and Fuel-PLIF images are discussed. Firstly, four steps in the blow-off mechanism are discussed in detail. The structural features of the A2 flame are compared with methane flame during blow-off. The higher degree of CH_2O-layer broadening in the kerosene flame and its implications to the blow-off duration and blow-off mechanism are discussed. Finally, the current flame and flames from Refs. [29, 17, 30, 46–51] were plotted on the theoretical regime diagram [52].

Chapter VIII: Final Remarks The conclusions of this dissertation as well as recommendations for future work are provided.

1.3 Blow-off theories

The flame blow-off process has been studied since the late 1940's, though it is still not well understood [19, 29, 53]. Early studies analysed the bluff body's role, inflow velocity, and various operating conditions on blow-off. In those studies, blow-off curves were reported as a function of the inflow velocity [24, 27, 54]. Several theories were proposed based on the observed data. In these theories, blow-off is hypothesized when the heat required by the fresh reactants for ignition exceeds the heat supplied by the hot products. Longwell et al. [27] suggested that the bluff body flame's stability depends on the residence time of the hot product gases inside the recirculation zone. The residence time is dependent on the velocity of the flow and the size of the stabilizer (bluff body). The velocity of the flow controls the rate at which the mass of air enters the recirculation zone (RZ), and the size of the RZ is dependent on the size of the stabilizer (bluff body). Therefore, the entrainment rate is dependent on d/U_B, where d is the diameter of the bluff body and U_B is bulk velocity [23]. A similar idea of the heat exchange balance between hot products and fresh reactants is reported in Refs. [55, 56].

Zukoski [26] defined blow-off as when the contact time scale between fresh reactants and hot products in the shear layer is less than the chemical time scale. The ignition of the incoming fresh, unburned mixture occurs in the shear layer, where it mixes with combustion products from the recirculation zone behind the bluff body. The flame remains anchored as long as this feedback process continues. He defines a "critical ignition delay time" (t_B) that must be less than the time of contact between the incoming reactants and the hot wake.

$$t_B = \frac{L_r}{U_B} \tag{1.1}$$

Where L_r is the recirculation zone length and U_B is the flow velocity.

The two commonly used correlations to predict the extinction limits of premixed flames are from DeZubay [57] and King [58]. The DeZubay empirical relationship was based on a series of experiments in a disc-shaped flame holder in a circular duct [57]. The correlation relates the fuel-air ratio at blow-off (ϕ_{ext}) with velocity, pressure, and temperature. The correlation is given in Eq. 1.2.

$$\phi_{ext} \propto \frac{U_b}{p^{0.95} D^{0.85}} \tag{1.2}$$

U_b is the bulk velocity, p is the pressure, and D is the disk's diameter. King developed an empirical correlation at elevated inlet temperature [58]. A single flame holder geometry was considered, and experiments were done for the velocity range of 122 to 198 m/s and pressure from 0.35 to 0.85 atm. The correlation was independent of the geometry as given in Eq. 1.3.

$$\phi_{ext} \propto p^{0.324} T^{1.07} (750 - U_b)^{0.252} \tag{1.3}$$

Ballal and Lefebvre [59] proposed a correlation for air/fuel ratio at lean blow-off as a function of air flow rate, pressure, and temperature. The correlation is based on the notion that flame extinction occurs when the heat required for the ignition of a fresh reactant exceeds the heat liberated by combustion.

$$\phi_{ext} = \left[\frac{U}{p^{0.25} T_{inlet} exp(T_{inlet}/150) D_c (1 - B_g)} \right]^{0.16} \tag{1.4}$$

Where U is velocity, T_{inlet} is inlet temperature, B_g is the blockage ratio, p is pressure and D_c is the characteristic dimension. Eq. 1.4 can be expressed in the more general form [60]:

$$\phi_{ext-1} \propto \left[\frac{m_{air}}{p^n V exp(T_{inlet}/b)} \right]^x \tag{1.5}$$

Where m_{air} is the flow rate of air, n is the reaction order, V is the volume of the combustion zone, and x is the constant determined experimentally. Ballal and Lefebvre [59] determined the optimum value of constants n, x, and b based on the experimental results obtained from the bluff body stabilized propane-air flame.

A significant issue with the above theories is the unknown chemical time scale. Radhakrishnan et al. [61] formulated a blow-off correlation of a bluff body stabilized premixed turbulent flame and compared the predictions with the experimental data. They assumed that laminar flame propagation takes less time than the characteristic fluid mechanics time. Thus, two characteristic timescales were dominant flow time and the shear layer mixing time. The extinction was defined when the chemical time scale λ / S_L is greater than the mixing time scale $RL_t / u^{'}$ where S_L is the laminar flame speed, L_t the integral length scale, $u^{'}$ the characteristic large-scale turbulent velocity, R is a constant, λ can be defined as the Taylor microscale and can be written as $\lambda = (15/A)^{1/2} l (u^{'} l / \nu)^{-1/2}$ where ν is the kinematic viscosity. These characteristic times are used to develop the correlation for blow-off. Radhakrishnan assumed that $u^{'} \propto U_b$ where U_b is the bulk air velocity at blow-off and $l \propto d$ where d is the length of the recirculation zone. The correlation of Radhakrishnan can be written in the form of

Eq. 1.6.

$$\frac{1}{Da} = \left[\left(\frac{C_1}{C_2}\frac{15}{A}\right)\left(\frac{U_b}{d}\frac{\nu}{S_L^2}\right)\right]^{1/2} \tag{1.6}$$

Its validation was based on extensive data sets with fully premixed flames in an afterburner-type geometry without swirl in the original paper. The comprehensive review of Shanbhogue et al. [23] on the lean blow-off of bluff body stabilized flames summarizes the blow-off phenomenon into two stages: localized extinction and wake alteration. They discuss the blow-off dynamics at various Reynolds numbers. A correlation is formulated based on the blow-off data in the literature showing the dependence of the blow-off Damköhler number (Da) on the Reynolds number. They summarized that the Damköhler number (Da) explains the essential physics behind blow-off and can be defined as the ratio of the flow time scale to the chemical time scale.

$$Da = \frac{\tau_{flow}}{\tau_{chem}} \tag{1.7}$$

The flow time scale τ_{flow} is estimated by choosing a characteristic length scale and a characteristic velocity scale. Three different chemical time scales τ_{chem} are considered: 1) the inverse of the extinction strain rate, 2) the “blow-off residence time" of a perfectly well-stirred reactor, and 3) the ratio of laminar premixed flame thickness to the flame speed. Additionally, they showed that the scaling based on unburnt gaseous velocities rather than burnt gaseous velocities provides a better collapse of the data than the scaling in Ref. [61]. Their comprehensive analysis showed that the simple correlation in Eq. 1.6 can be implemented to achieve consistent results across a wide range of conditions and geometries, hence demonstrating that for simple gaseous fuels, a blow-off correlation can be obtained without the need for empirical fits or adjustable constants. Kariuki et al. [29] validated this correlation over several bluff body diameters and a range of U_b. They found that Eq. 1.6 collapses LBO data from methane flames, indicating that blow-off is strongly linked to laminar flame speed.

The ability of Eq. 1.6 to predict blow-off in a swirl stabilized premixed, non-premixed, and spray flames was reported in Ref. [20]. They found that all three flames extinguished at the same critical Da, providing support for using Eq. 1.5 to estimate blow-off in swirling flames. Recently, Allison et al. [62] evaluated the LBO limits with complex fuels such as kerosene spray flames. They found that kerosene flames are less stable than simpler fuels. They used a $1/Da$ scaling equation (see Eq. 1.5) and found that laminar flame speed plays a dominant role in scaling. Furthermore, they reported that this correlation could be used as a good approximation for spray flames. The kerosenes used in that work were standardised fuels coded as “A2”, which is Jet-A, and “C1”, an alternative Gevo ATJ kerosene, described in Ref. [43]. On comparing kerosene fuels, the kerosene flames with a high derived cetane

number (DCN) are more stable than those with a low DCN [62–64]. The spray characteristics near blow-off of alternative fuels were compared to A2 in Ref. [65]. Rock et al. [63] showed through CH* images that the flames produced with high DCN have more re-ignition events, making them resilient to blow-off.

While these prior studies have provided significant insight into the LBO limits and structure of gaseous fuels, recent studies have reported that flames with heavy hydrocarbons or complex fuels show a substantial difference in LBO and flame structure [62, 63]. Tambold et al. [66] showed that alcohol flames blow-off at higher equivalence ratios than methane. Carbone et al. [38] observed changes in the flame's global properties with complex fuels and suggested re-examining their scaling parameters. Additionally, in Refs. [38, 66], flames with a high Lewis number (*Le*) are more susceptible to extinction than those with a low *Le*. It is clear that, from a fundamental viewpoint, the LBO of turbulent premixed flames has focused on simple gaseous fuels, and the LBO scales with the square of the laminar flame speed in gaseous fuels. Previous work concerning the LBO of kerosene-fueled flames has focused on spray flames, where it may be difficult to isolate fuel chemistry effects from those associated with the atomization and evaporation of different fuels. To meet this, the LBO limits were evaluated with vapourised kerosene fuel in Chapter 4, and the results were compared with the methane flame.

1.4 Laminar premixed flames properties

Prior to discussing the structure of the bluff body stabilized turbulent premixed flame, it is helpful to discuss the laminar premixed flame's structure. As the most popular combustion model for the turbulent premixed flame is based on the assumption [67, 68] that flames that are not strongly distorted by turbulence, the local flame structure retains the attributes of a laminar flame.

Fig 1.2, illustrates the structure of a laminar premixed flame, highlighting its principal features. Laminar premixed flames consist of three principle features; i) preheat zone, ii) reaction zone, and ii) equilibrium zone. In the preheat zone, the decomposition of fuel occurs due to the conduction of heat from the reaction zone. A negligible reaction occurs in this region because of the low temperature and high activation energy of the fuel consumption reactions. Most chemical reactions occur in the reaction zone. The thickness of the reaction zone is typically of the order of 1 mm, and the temperature is high enough to overcome the activation energy of the important reactions. In the equilibrium zone, the balance is attained between the formation and dissociation rates of species, resulting in chemical equilibrium.

Compared to the reaction zone, the equilibrium zone has a larger thickness, and most of the heat release occurs in this region.

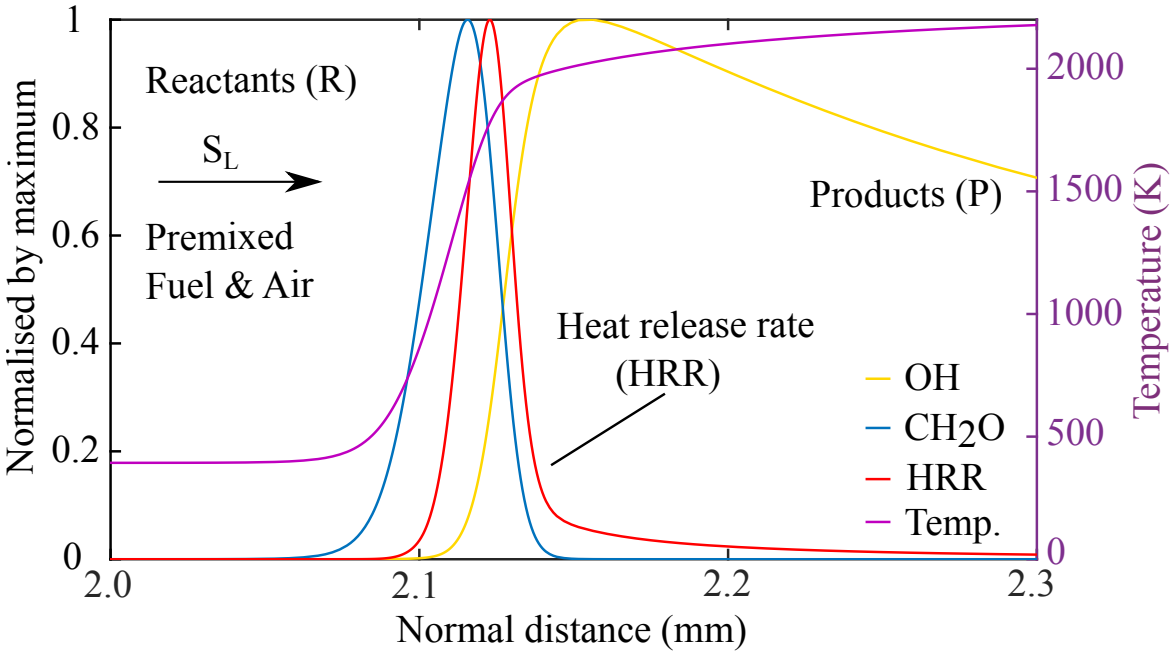

Fig. 1.2 Profile of temperature, heat release rate, OH and CH_2O obtained from the Cantera simulation of methane premixed flame at $\phi = 1$. Detail of the simulations can be found in Chapter 3.

The key parameter of the laminar premixed flame is the characteristic velocity and length scales. Laminar flame speed (S_L) represents the velocity scale. S_L represents the propagation of the premixed flame normal to itself and consumes the available reactants. There are three characteristics length scale defined based on the thickness of the flame. The length scales include preheat layer thickness (CH_2O), reaction layer thickness (HRR), and total flame thickness (includes both preheat and reaction layer thicknesses). Fig. 1.2 illustrates the definition and relationship between different length scales discussed above. As well as, the profiles of the temperature and OH-species profile as a function of normal distance.

1.5 Blow-off studies on bluff body stabilised turbulent premixed flames

One of the earliest experimental investigations into the turbulent flame structure during blow-off was performed by Nicholson and Field [54]. They employed shadowgraphy and schlieren

photography to visualise the flame and flow field patterns. They observed flame extinguishes in the downstream wake and then moved upstream (close to the bluff body). Similar behaviour in the blow-off mechanism was reported by Ref. [27]. Their investigations reported that the flame became more resilient to blow-off with an increase in inlet air temperature. On the other hand, increasing bulk velocity (U_b) and decreasing bluff body diameter (d) reduce flame stability. Whereas, varying pressure from 0.2 to 3.2 bar has a negligible effect on the lean blow-off limit (LBO). Williams et al. [56] performed a detailed investigation into the effect of fuel type, bluff body diameter, and shape on the blow-off dynamics. They observed RZ's shortening before blow-off, and the flame propagation in the downstream wake is independent of the stabilization mechanism close to the bluff body. Moreover, they noticed a residual flame in the RZ during blow-off. Similar to Ref. [54, 27, 56], Russi et al. [69] showed an increase in bluff body temperature broadens the stability limit. They suggested that a higher temperature of the bluff body leads to an increase in RZ's temperature, helping in flame stabilization.

To investigate the effect of flame holder temperature on flame stabilization. Zukoski [26] used a water-cooled bluff body and combustion chamber. They maintained the bluff body and combustion chamber temperature at reactant temperature (≈339 K). Furthermore, they measured the temperature of the RZ using probes. They found that the RZ temperature is independent of the shape and size of the bluff body. Prior to the blow-off, they noticed a small temperature drop of RZ. However, they attributed this drop in temperature due to experimental error, as the uncertainty of the measuring equipment was 45 ^{0}C. The effect of blockage ratio (BR) on the blow-off limits was reported by Ref. [70]. Their results agree with the Zukoski [26], showing that the average RZ width is not dependent on the flow velocity and equivalence ratio (ϕ). However, stability limits increase with an increase in BR up to a critical value of BR. Moreover, as blow-off was approached, they found residual flame and a decrease in the RZ length. They also reported the entrainment of cold reactants into the RZ from downstream. The experiments of Filippi and Fabbrovich-Mazza [71] suggested chemistry affects the stability limits significantly. They studied the effect of fuel injection, oxidant, fuel-air mixture, and inert gas on the stability limit. Their results suggest that the stability limit improves with an injection of fuel-air mixture into the RZ.

The studies in Ref. [26, 27, 54, 69] suggested that heat and mass exchange between the free stream and RZ is crucial for the stability of the flame. However, very few researchers focus on this exchange process [70, 72]. Winterfeld [72] experimentally determined the residence time (τ_r) of the gas inside the RZ. τ_r was observed to be independent of the bluff body geometry and increased in the presence of flame compared to isothermal conditions. As observed by Zukoski [26], they also noticed no change in RZ temperature before blow-off.

Lefebvre et al. [3] experimentally estimated the entrainment of fresh air from the blulk flow into the RZ. They noticed entrained mass from the bulk flow decreased with the increase in blockage ratio. Attempts were made to measure the RZ concentration using a probing technique [73, 74]. Before blow-off, Walburn [74] observed changes in the concentration of the burnt gases in the RZ while traversing the probe along the axis of RZ. On the other hand, no change in concentration of the RZ gases was observed at constant equivalence ratio and fixed location from the bluff-body in Ref. [73]. They did not study the conditions just before the blow-off. The result suggested that the assumption of a homogeneous well-stirred chemical reactor may be valid in RZ for conditions far from blow-off.

The experimental studies discussed above associated blow-off with the fluid-mechanical timescale is small enough compared to the chemical timescale. Other theories include when the chemical time scale is smaller than the contact time between the hot product in RZ and the free stream fresh reactants [26]. Longwell [27] proposed flame stability increases with an increase in resident time of hot gases in RZ. On the contrary, Yamaguchi et al. [75] suggested the onset of blow-off is because of local extinction due to excessive stretch on the flame, which leads to the entry of cold reactants into the RZ, reducing the temperature of the RZ. A cylindrical rod stabilized propane flame was studied for Reynolds number (Re_d) varying from 12000 to 20000. At far from blow-off, the flame is in a cylindrical shape. As the blow-off approached, the flame shape change was observed with the flame lying inside the RZ. The observation of Yamaguchi et al. [75] agrees with the results of Ref [26, 27] discussed above, as they noticed that the flame abruptly blow-off in the attachment region, failing to propagate into a downstream wake.

Further understanding of the structure of turbulent premixed flames near blow-off and the transient behavior of such flames during blow-off was achieved with recent advancements in high-speed imaging of OH* chemiluminece and planar laser-induced fluorescence (PLIF) imaging of OH and CH_2O [17, 23, 29**?** –32]. From these experimental studies, it can be deduced that the flame exhibits transient characteristics near blow-off as observed by Nair and Lieuwen [76] in a pilot, swirl, and bluff body stabilized flame. They showed that flames occur in two distinct stages before blow-off. The first stage is localized extinction, which is the formation of holes along with the flame; the hole formation is due to the instantaneous stretch rate exceeding the extinction stretch rate. During this stage, the flame can persist indefinitely, and overall, the flame and wake seem to be unaltered. The second stage is marked by the alteration of wake dynamics, the flame front's violent flopping, an asymmetric mode of flame shape oscillations, and even larger straining of the flame. The flame and flow interaction with a propane flame close to blow-off was studied by Chaudhuri et al. [77], using time-resolved chemiluminescence imaging, simultaneous particle imaging velocimetry, and

OH planar laser-induced fluorescence imaging. The high-speed OH* chemiluminescence images showed that the flame switches from varicose to sinuous mode close to blow-off. A similar structure of the flame was reported in Ref. [78]. They found the mean OH profile changed from bi-modal to uni-modal near blow-off. The joint PIV and OH-PLIF images reveal that the flame front and the convecting Kelvin Helmholtz vortices overlap with the shear layer, resulting in the local strain rate exceeding the extinction stretch rate in the local extinction of the flame along the shear layer. This localized extinction leads to the formation of a large number of holes in the flame, which can couple with instabilities, leading to the large flapping of the flame and its eventual extinction. They also observed that the fresh reactants enter the recirculation zone near blow-off. However, no considerable change in the velocity profile is observed except shortening of the recirculation zone close to blow-off. Yamaguchi et al. [75] suggested that the excessive stretching of the flame leads to local extinction and the onset of blow-off. The sudden inflow of cold reactants into the recirculation zone from the downstream end of the recirculation zone leads to the drop in temperature of the recirculation zone below the critical value. Refs. [17, 28, 30] reported similar results of excessively stretching the flame close to blow-off.

The mechanism of the fresh reactants entering into the recirculation zone from the forward stagnation zone with a methane flame was observed by Dawson et al. [32]. A significant fragmentation occurred, with the flame anchored to the bluff body close to blow-off. Near blow-off, the flame length was about 2d long, where d is the bluff body's diameter. Kariuki et al. [29] found that methane flames change from cylindrical to "M-shaped" as they approach LBO. Their results suggested that the near blow-off flame lasted longer than the residence time in the recirculation zone and supported the well-stirred reactor's underlying assumption. Also, the regions of peak heat release were marked by the presence of OH, which was found to be continuous and thin under conditions far from blow-off. They found that the duration of the blow-off transient was an order of magnitude greater than the characteristic residence time d/U_b in the burner for all blow-off conditions investigated. The experiments of Kariuki et al. [17, 29] suggested that reactions occur within the recirculation zone (RZ) just prior to blow-off. Namely, blow-off was found to begin in the downstream region due to local extinction, which led to the flow of partially-burnt and unburnt reactants into the RZ, further destabilising flame-fronts near the shear layer. Results from Refs. [31, 78] of propane flames suggested that as blow-off is approached, the degree of interaction between the shear layer and the flame-front increases. They also observed that localised regions of high strain rate caused flame-front extinction within the shear layer, forming a hole that facilitated fresh reactants' entrainment into the RZ. In contrast, Dawson et al. [32] and Kariuki et al. [29], who investigated methane flames, did not notice significant extinction in the shear layer;

rather, they observed it to occur in the downstream region of the RZ, which leads to the eventual advection of cold reactants into the RZ. This was further confirmed using joint planar laser-induced fluorescence (PLIF) imaging of OH and CH_2O, Kariuki et al. [36] imaged heat release (HR) layers in their methane flames as LBO was approached. Breaks in the HR regions, which were interpreted as local extinction events, were observed along with their flame shear layers. However, no apparent connection between the cold reactants in the RZ and the annular reactant jet was observed, suggesting that reactants did not enter the RZ from the sides. Their findings were consistent with OH-PLIF images presented in Refs. [29, 32], which suggested the presence of reactions within the RZ during the LBO transient. A significant accumulation of CH_2O was found inside the RZ close to LBO [36]. The difference in the flame behaviour at LBO between Refs. [31, 78] and Refs. [29, 32] could be attributed to the different burner geometries [8] and the Lewis number (Le). Namely, the propane flame in Refs. [31, 78] has $Le > 1$, rendering it more susceptible to local extinction due to strain than a methane flame with $Le \approx 1$. Yet, for methane, extinction events appear to result from flame-flame touching and hence incomplete combustion primarily.

Most of the aforementioned studies emphasized the role of local extinction in dictating global blow-off. Various experimental investigations were conducted to study the flow field (e.g., turbulence level and length scale) of turbulent premixed bluff body stabilized flames [29, 79, 80]. Kariuki et al. [29] studied the flow field of non- and reacting methane flames at conditions far and close to blow-off. The height of the RZ is approximately 1 bluff-body diameter (d) under non-reacting conditions, yet in reacting conditions this height increases to $1.5 - 2 \times d$. Also, they observed that the turbulent intensity increases when moving away from the burner towards the downstream regions of the flame. A similar rise in turbulent intensity was observed in disc-shaped bluff body flames [79, 80]. Chaudhuri et al. [79] associated an increase in turbulent intensity with local extinction of flamelets in the shear layer. Kariuki et al. [29] determined the turbulent Reynolds number (Re_T), Karlovitz number (Ka) and Damkhöler number (Da) along the flame front at conditions far from and close to blow-off. They found Ka to increase and Da to decrease by a factor of three as their flames approached blow-off. Here, Ka and Da are defined following Peters [52]:

$$Re_T = \frac{u' l}{\nu} \tag{1.8}$$

$$Ka = \frac{\tau_{chem}}{\tau_{\eta *}} = \left(\frac{\delta_L}{\eta *}\right)^2 = \left(\frac{u'}{S_L}\right)^{3/2} \left(\frac{\delta_L}{L_T}\right)^{1/2} \tag{1.9}$$

$$Da = \frac{S_L L_T}{u' \delta_L} \tag{1.10}$$

where $\tau_L = \delta_L/S_L$ and $\tau_\eta*$ and $\eta*$ are the Kolmogorov time and length scales, respectively. In Eq. 1.9 and 1.10, δ_L is the laminar flame thickness, S_L is the laminar flame speed, u' is the magnitude of the velocity fluctuations, and L_T is the integral length scale. $Ka < 1$ indicates that the chemical time scale is shorter than the Kolmogorov scales and the turbulence is not able to affect the inner flame structure. That is the inner structure of the flame is still close to the laminar flame. On the other hand, $Ka > 1$ and $Da > 1$ the turbulent integral time scale is larger than the chemical time scale, but the Kolmogorov scales are smaller than the flame thickness and may modify the internal flame structure [81].

Karuki et al. [16] noticed the increase in Ka in the downstream region of the flame. redThey observed a maximum value of Ka of the order of 10 at a distance of 1.2d, where the flame closes from opposite sides of the RZ at a condition close to blow-off. Ka significant variation suggested that the flame is more susceptible to extinction where it bends parallel to the bluff body. In general, extinction occurs when the flame stretch is higher than S_L/δ_L [52]. An increase in local extinction was observed by Chowdhury et al. [80] with increased free stream turbulent intensities (u'/U_b). The flame structure alters as the turbulence intensity increases from 4 to 14 %. They observed unburnt mixture fingers inside the hot product without discontinuities in the heat release front. At high turbulence intensity (24%), the local flame structure was strongly modified, with flamelet merging, localized extinction along the shear layer, and flame fragmentation. The flame's general shape was observed to change from varicose to sinus mode as observed in Refs. [23, 76, 77]. The broadening of the preheat zone with the turbulence was observed. Similarly, preheat zone broadening was observed by Karuki [16], in methane flame close to blow-off. As the turbulence intensity was further increased to (30%), the flame front was found to feature four characteristics: flamelet merging, localized extinction, pocket formation, and fragmentation of the flame segments. The experimental results of Kheirkhah and Gülder [82] showed that the flame front is weakly wrinkled at low turbulence intensity $(4-6\%)$. However, strong wrinkling, localized quenching, and pockets of reactants have been found using the laser tomography technique at higher turbulence intensity. An increase in flame thickness and flame-front wrinkling were found to increase with u'/U_b [37].

Tamadonfar and Gülder [83] studied the effect of Ka on the inner structure of the methane/air turbulent premixed flame. All experimental conditions were located in the thin reaction zone regime as the variation Ka is from 1.2 to 20.7. The temperature and velocity fields were investigated using Rayleigh scattering and particle image velocimetry (PIV). With an increase in Ka, the normalized preheat and reaction zone thickness decreased, indicating an increase in stretch rate is the controlling mechanism. The study with piloted methane-air flames subject to extreme turbulence levels [33] (e.g. $Ka > 100$) exhibited continuous

reaction layers with little localised extinction [46–50]. Skiba et al. [50] observed a similar broadening of preheat regions in their high Ka methane flames. They noticed an increase in preheat region with an increase in axial distance from the burner exit and suggested that local extinction was rare even for their flames with $Ka > 100$; yet, this is primarily a consequence of the large pilot-flame employed in their study. Zhou et al. [47, 49] reported that the flames with $Ka > 126$ have a CH layer 10 times larger than the laminar CH layer. In their flame images, the CH and HCO were observed to penetrate deep into the OH layers, further supporting that the flame is a distributed reaction regime (DRZ).

An important feature of turbulent premixed flames is the flame surface density (FSD). It is commonly used to model the averaged or filtered reaction rate term in RANS or LES simulations, respectively [5, 84, 85]. Additionally, it can be used to determine local and global consumption speeds of turbulent premixed flames [8]. The variation of FSD in a conical bluff-body stabilised methane flame at stable condition and close to blow-off was investigated by Kariuki et al. [29].

FSD has also been studied for premixed V-shaped flames in several previous studies [30, 37, 86]. Chowdhury et al. [80] observed local extinction of the flame with an increase in turbulent intensity (u'/U_b), leading to a decrease in FSD. Kheirkhah et al. [37] reported a similar reduction in FSD with increasing u'/U_b. In all of these studies, the FSD exhibited an inverse parabolic distribution when presented in average progress variable ($\overline{c}$) space. While most of these studies focused on the influence of turbulence on FSD, recently, Chowdhury et al. [80] also considered the effects of fuel-type on FSD. Namely, they considered methane-, ethylene-, and propane-fueled flames stabilized on a disc-shaped bluff body and found FSD to depend on the unstrained laminar flame speed.

Trabold et al. [39] computed the integrated 2-D FSD for alcohol fuels. The integrated 2-D FSD was found to change at the same rate up to a height of four times the jet diameter for all flames. It was postulated that the turbulent shear flow influenced the flame structure up to that height. In the downstream regions, they observed a larger increase in the value of the integrated 2-D FSD for methanol, ethanol, and methane. The higher value is linked to intense wrinkling and small volume as the flame length was smaller for these fuels in lean conditions.

Beyond being an important intermediate combustion species, CH_2O is also often used as a marker of the preheat region of premixed flames [17, 50]. The preheat layer was measured in many previous studies using fuels such as methane, ethylene, and propane [17, 30, 50]. In all of these studies, preheat-layer broadening was observed with an increase in normalised turbulence level (u'/S_L^0). Kariuki et al. [17] applied CH_2O-PLIF imaging to ethylene in a conical bluff body flame and found that the flames close to blow-off displayed broad regions

of CH_2O, with a significant amount of it being located within the recirculation zone. This broadening of CH_2O-layer can be related to an increase in (u'/S_L^0) because of the decrease in equivalence ratio. Moreover, flames close to blow-off tended to demonstrate a high degree of fragmentation (i.e. localised extinction), particularly in regions far downstream of the bluff body [29, 17]. The broadening of the preheat layer with an increase in (u'/S_L^0) has also been reported in several numerical studies [87, 88]. The preheat layer thickness can be as high as ten times the laminar flame thickness [47, 48, 50]. Recently, numerical efforts have been performed to understand the impact of turbulence and heavy hydrocarbon fuel properties on premixed flame features, including preheat layers [89–91]. For example, the direct numerical simulation (DNS) study of Aspden et al. [40] suggested that high Lewis number (Le) flames such as dodecane are more suspected of turbulent mixing and result in the broadening of the preheat zone.

Recent advancement in numerical methodologies have made it possible to simulate these laboratory-scale flames [8–15]. Massey et al. [9] studied the structure of premixed methane flame at far from and close to blow-off using Large Eddy Simulations (LES) and compared their results with the experimental results of Ref. [16]. They were able to capture the inner share layer and RZ accurately. Additionally, a recent DNS study [40] found that flame-front wrinkling was suppressed in high-Le flames, resulting in a considerable reduction of the turbulent flame speed. The increased flame front thickness with Ka was observed by ref [92]. The turbulence effect on the preheat and reaction zone of a turbulent methane-air slot bunsen flame was investigated using direct numerical simulation (DNS) [15]. They observed a broadening of the preheat regions and claimed turbulent structures are responsible for this broadening. A similar broadening of the preheat regions was observed in Ref. [93].

While such studies of single-component hydrocarbons have provided significant insight into the turbulent premixed flame structure [18, 29, 32**?** , 77**?**], there have been relatively few investigations into the fundamental aspects of turbulent premixed flames operated with heavy hydrocarbon fuels. Heavy hydrocarbon fuels have lower resistance to cracking, and they can decompose into small fragments in the preheat zone [38, 94, 95]. Also, the experimental studies of Dinkelacker et al. [96] and Chen and Bilger [97] reported that the turbulence affects the preheat zone, thus affecting the type of reactants supplied to the reacting zone.

Since heavy hydrocarbon fuels decompose readily, the prolonged exposure to high temperatures in the preheat zone could modify the type of hydrocarbon fragments reaching the reaction zone. The effect of fuel at different equivalence ratios on the local and global flame is studied in Ref. [38]. They studied straight-chain (paraffin and olefin), branched, cyclo, and aromatic C1-C8 hydrocarbons. The behavior of the methane/air flame deviates significantly from that of liquid fuels. The appearance of isolated fluid pockets emitting

notable chemiluminescence is found to increase with fuel molecular weight. However, the difference between the flame structure and the preheat zone for gaseous fuels (methane, ethylene, and propane) is minimal compared to large molecular weight fuels, such as dodecane. The high Lewis number of heavy hydrocarbon flames acts to suppress wrinkling of the flame, resulting in lower turbulent flame speed compared to low molecular weight fuels[40]. Also, broadening of the thermal profile of the flame is observed with an increase in turbulence intensity. The high Lewis number dodecane fuel response is quite different from the single-component fuel [40]. The local flame speed with dodecane fuel is enhanced in the region of negative curvature. The positive curvature experiences a defocusing of heat through diffusion and results in a decrease in reaction rate. This increase and the decrease in the flame speed result in a decrease in the local Damköhler number and an increase in the local Karlovitz number and make the flame more susceptible to turbulent mixing, which mixes the partially reacted reactants into the preheat zone and results in the broadening of the preheat zone. The effect of turbulence is studied on n-heptane fuel for unity Lewis number and large Lewis number using DNS [98]. They performed the simulation at unity and non-unity Le to isolate the differential diffusion effects. They found that the differential diffusion effects were present in high Ka flame leading to lower fuel consumption and heat release. In another study [99], they considered multiple fuels with $Le > 1$. They observed similar turbulent flame speeds for all fuels at a fixed reaction zone Ka in the absence of differential diffusion. Since flames with heavy hydrocarbon fuels have a very complex chemical pathway and distinctly different diffusivities than those with methane and hydrogen, it remains unclear how turbulence influences their chemistry [40]. It is important to understand the effect of fuel composition on the local and global extinction processes. In the past, fuel effects were consolidated under one fundamental flame property: the laminar flame speed [38].

Although extensive work has been done to understand the blow-off mechanism in a premixed single component fuel, few studies have concentrated on the blow-off mechanism of heavy hydrocarbon fuels. The numerical simulation with DNS reported that the high-intensity turbulence affects the flame dynamics of heavy hydrocarbon fuel as it broadens the preheat zone. Also, heavy hydrocarbon fuels have a very complex chemical pathway and distinctly different diffusivities than those with methane and hydrogen; it remains unclear how turbulence influences their chemistry [38]. It is important to understand the effect of fuel composition on the local and global extinction processes. In this dissertation, the effect of fuel composition on the flame dynamics was studied using ethanol, heptane, and kerosene fuel.

1.6 Summary and specific objectives

The blow-off mechanism in premixed flame has been studied extensively in literature with single component gaseous fuels such as methane, propane, and ethylene [29, 100, 18]. The effect of bluff body diameter (blockage ratio) on lean stability curves was studied with methane [28], and the results were evaluated with the correlation of Radhakrishnan et al. [61]. This correlation was validated on swirl stabilized premixed, non-premixed, spray flames by Ref. [20], and they found that all three flames extinguished at the same critical *Da*. Moreover, Allison et al. [62] evaluated this on spray kerosene flame [62] and observed S_L plays a dominant role in blow-off. Therefore, it is clear that LBO in simple premixed gaseous fuel and kerosene spray flame scales with the square of the laminar flame speed [20, 29, 61, 62]. Furthermore, previous studies on LBO with kerosene on spray flame [62, 63] reported that DCN plays a crucial role in blow-off. Flames with higher DCN are more resilient to blow-off, as they have re-ignition events. This enhanced re-ignition behaviour of kerosene flames prolongs the blow-off duration. A recent study with vapourised alcohol premixed flame [66] showed that alcohol flames blow-off at higher equivalence ratios than methane. The changes in the flame's global properties with complex fuels were observed by Ref [38] and suggested re-examining their scaling parameters, as in the past, fuel effects were consolidated under one fundamental flame property; namely, the laminar flame speed [38]. Additionally, it was observed that flames with a high Lewis number (*Le*) are more susceptible to extinction than those with a low *Le* [38, 66, 87]. Besides, previous work concerning the LBO of kerosene-fueled flames has focused on spray flames, where it may be difficult to isolate fuel chemistry effects from those associated with the atomization and evaporation of different fuels. In Chapter 4 of this dissertation, the effect of fuel composition and *Le* on the LBO is studied with methane, vapourised ethanol, heptane, and two kerosenes (A2 and C1).

Understanding of turbulent-flame interactions has been primarily derived from studies of gaseous fuels. Yet, as mentioned above, recent experimental, LES, and DNS results highlight differences between flames produced by burning simple and more complex fuels [38, 40, 41]. The DNS study of Aspden et al. [40] reported that flame-front wrinkling is suppressed due to high *Le*, which leads to reduced turbulent flame speeds. Such results suggest that the LBO process for heavy hydrocarbon fuels may be different from that associated with simpler gaseous fuels. There have been very few studies concentrating on the blow-off mechanism and flame dynamics of bluff-body flames with multi-component heavy hydrocarbon fuels. Since heavy hydrocarbon liquid fuels are more commonly used in practice, there is a need to study turbulent, premixed, heavy hydrocarbon flame structures. For this reason, recent studies have begun to investigate the influence of turbulence and fuel effects on heavy hydrocarbon-fueled flames. Different, more complex chemical pathways

are available for heavy-hydrocarbon fueled flames. Additionally, such fuels exhibit slow oxidation at low $(T < 650K)$ to intermediate $(650K < T < 1000K)$ temperatures [101], and this leads to broad CH_2O regions. A recent DNS study [40] found that flame-front wrinkling was suppressed in high-Le flames, resulting in a considerable reduction of the turbulent flame speed. In Chapters 5 and 6, the structure and transient aspects of turbulent, lean, unconfined bluff-body stabilised premixed flames (non-swirling) of vapourised liquid fuels were investigated at stable and close to blow-off. It has been suggested that the low-temperature chemistry characteristics of fuel may correlate with its LBO condition [38], which further motivates the comparison between the fuels performed here. Moreover, this work meets that need by considering premixed vapourised heavy hydrocarbon fueled flames stabilised by an unconfined bluff-body burner similar to that in Refs. [29, 31**?** , 32, 36].

The specific objectives of this dissertation are:

1. To measure the LBO limits of flames with various vapourised liquid fuels and evaluate the scaling parameters based on laminar flame speed.

2. To provide a detailed comparison between flame behaviour with various fuels during LBO in terms of structure and blow-off duration.

3. To provide comparisons between the structural features of such flames using high-speed OH-PLIF imaging, and low-speed (10 Hz) PLIF imaging of CH_2O.

4. To measure the 2-D FSD, flame front curvature, and local turbulent consumption speed at stable conditions and close to blow-off.

5. To investigate the effect of fuel properties on the spatial distribution of CH_2O-layer thickness.

As mentioned above, the change in flame shape was observed as blow-off approached [32, 29, 36, 31]. Kariuki et al. [29] observed local extinction in the downstream regions due to an increase in local Karlovitz number. Simultaneous measurement of OH and PIV in Ref. [31] suggested localised extinctions of the flame due to locally high strain rates. In Chapter 7, high-speed velocity measurements were performed.

The objectives of Chapter 7 are:

6. Evaluate the global features of the velocity field in non-reacting and reacting premixed vapourised heptane flames under stable and near blow-off conditions.

7. Calculate the turbulent intensity and turbulent length scales at different locations relative to the flame. To discuss flames with different fuels in the context of the regime diagram.

Chapter 2

Experimental methods

The details of the experimental apparatus are provided in Section 2.1. The schematic and photographs of the burner and vapouriser are provided, along with operating conditions and flow rates. The experimental conditions are provided in Table 2.2. In the second part of this section (2.2), the experimental procedure and diagnostics are discussed. The details regarding the method used to determine the blow-off limits for all five are provided. High-speed imaging of OH*-chemiluminescence and planar laser-induced fluorescence (PLIF) imaging of OH and CH_2O is presented. The particle image velocity (PIV) system used to measure the velocity field in the non reacting and reacting cases is presented.

Lastly, details of the image processing routines used to analyse the images acquired from the separate diagnostic techniques and details of the measurement methods used to evaluate the flame surface density (FSD) and 2D-Curvature are presented. The method used to process the PIV data is also presented in this Chapter.

2.1 Apparatus

2.1.1 Burner and fuels

A bluff body burner, similar to that used in Ref. [29], was employed to study turbulent premixed flames behavior close to blow-off. A schematic of this burner is presented in Fig. 2.1a (left). The burner consists of a 300-mm long outer tube with an internal diameter of 35 mm. This tube was mounted to a small plenum, and a small section of honeycomb was fitted within its center to facilitate flow straightening. To ensure smooth flow separation at the tube's exit, its edge was tapered and filed to a sharp point. A conical-shaped bluff body was mounted at the center of the outer tube via a small rod (outer diameter of ~ 6.5 mm) that was positioned at the center of the tube. The bluff body possessed a 45° half-angle and its widest diameter, which aligned with the exit of the outer tube, measured 23 mm, providing a blockage ratio of 43%. The picture of the burner (top view) is shown in Fig. 2.1a (right).

Figure 2.1b splits the flame into different regions to facilitate later discussions: the "anchoring" region is defined by $x < 15$ mm, while the "downstream" region corresponds to $x > 15$mm, where x is axial distance from the bluff body. Both areas include the RZ as well as the shear layers and the annular jet.

Table 2.1 Chemical composition of the kerosene fuels studied [43].

Name	Composition	Avg. Mol. Form.	Cetane number
Jet A (A2)	15% 1,2,4-trimethylbenzene (C_9H_{12}) + 30% iso-dodecane ($iC_{12}H_{26}$) + 20% n-undecane ($nC_{11}H_{24}$) + 35% pentyl-cyclohexane ($MC_{11}H_{22}$)	$C_{11}H_{22.1}$	48.3
Gevo ATJ (C1)	85% iso-dodecane ($iC_{12}H_{26}$) + 15% isohexadecane ($iC_{16}H_{34}$)	$C_{12.6}H_{22.7}$	17.2

The fuels considered here included two kerosene blends, ethanol and n-heptane (referred to as heptane). The kerosene fuels were procured from USA National Jet Fuel Combustion Program [43]. The kerosene fuels considered were a conventional Jet-A blend, referred to as A2, and an alternative Gevo alcohol-to-jet (ATJ) kerosene, referred to as C1. Table 2.1 presents the chemical composition of each kerosene fuel used. The details of chemical composition and physical properties of kerosene can be found in Ref. [43]. The primary difference between the two kerosene was the derived cetane number (DCN); namely, A2

possesses a DCN of 48.8 while the DCN for C1 is 17.1 [43]. Ethanol and heptane were considered as they consist of a single component. Additionally, ethanol contains one hydroxyl group, and it will be interesting to see where alcohol lies on the blow-off curve compared to kerosene fuels.

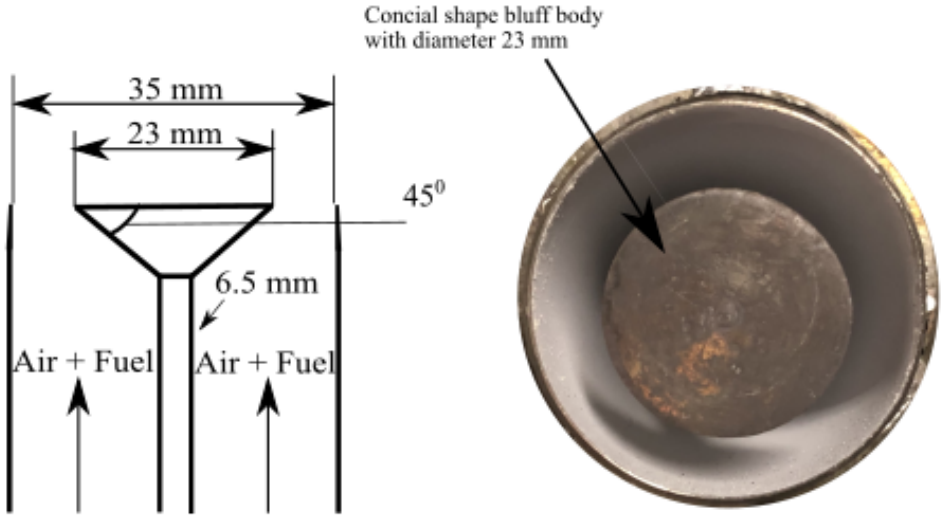

(a) Schematic of the bluff body burner (left), top pictorial view of the burner.

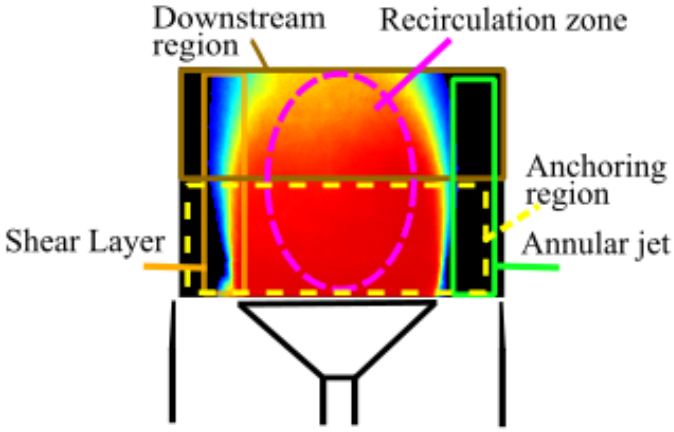

(b) Different regions of the flame.

Fig. 2.1 (a) Schematic of bluff body burner with bluff body diameter of 23 mm, the photograph of the burner (left) shown the top view of burner and (b) OH-PLIF image showing different regions of the flame.

2.1.2 Experimental conditions

The blow-off limits were evaluated with methane, heptane, ethanol, A2, and C1 for the range of velocity shown in Section 4. Two conditions were investigated with fast imaging and laser diagnostics: stable burning $\phi/\phi_{bo} = 1.20$ and close to blow-off $\phi/\phi_{bo} = 1.01$, where ϕ is the equivalence ratio and ϕ_{bo} the equivalence ratio at blow-off. The bulk velocity U_b at the annular opening was 23 m/s for all these experiments. For some comparisons, and since each fuel was globally extinguished at different equivalence ratios at the same velocity, the A2 and C1 flames were also studied at a constant ϕ of 0.75. The velocity field measurement was performed for non-reacting and reacting conditions. A summary of the experimental conditions is given in Table 2.2.

Table 2.2 Experimental conditions at inlet mixture temperature of 393 K. The error in $\phi/\phi_{bo} = \pm 0.01$.

Fuel	velocity (m/s)	ϕ	ϕ_{bo}	ϕ/ϕ_{bo}
Ethanol	23.5 $\pm$1	0.75	0.625	1.20
		0.63	0.625	1.01
Heptane	23.5 $\pm$1	0.75	0.63	1.20
		0.638	0.63	1.01
Jet-A	23.5 $\pm$1	0.82	0.68	1.20
		0.688	0.68	1.01
C1	23.5 $\pm$1	0.85	0.71	1.20
		0.72	0.71	1.01

2.1.3 Vapourizer configuration

The liquid fuel was vapourised before entering the burner. Figure 2.2 shows a schematic of the vapouriser. The vapouriser used in this study is a scaled-up version of the one employed in Ref. [38]. The vapouriser is designed to provide a maximum air flow rate of 1000 liters per minute at a temperature of 150 ^{o}C.

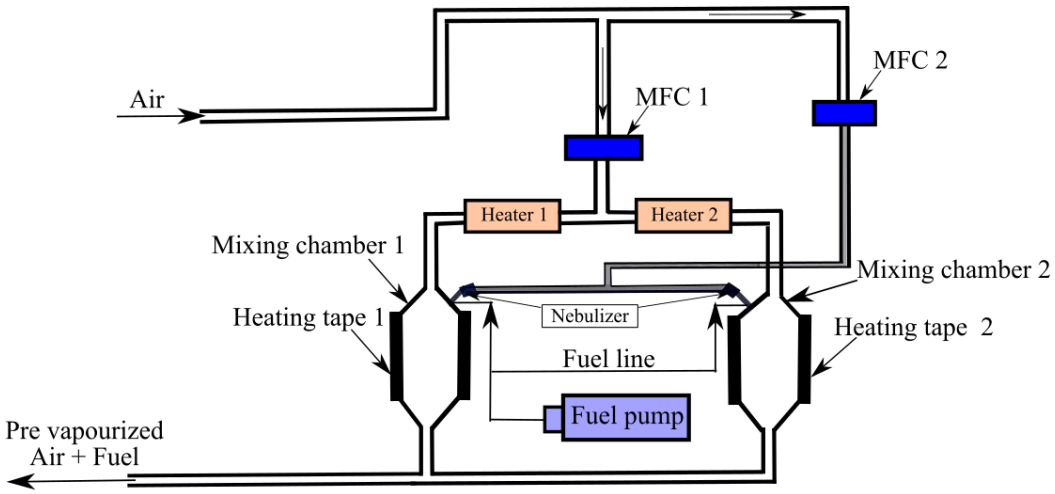

(a) Schematic of vapouriser.

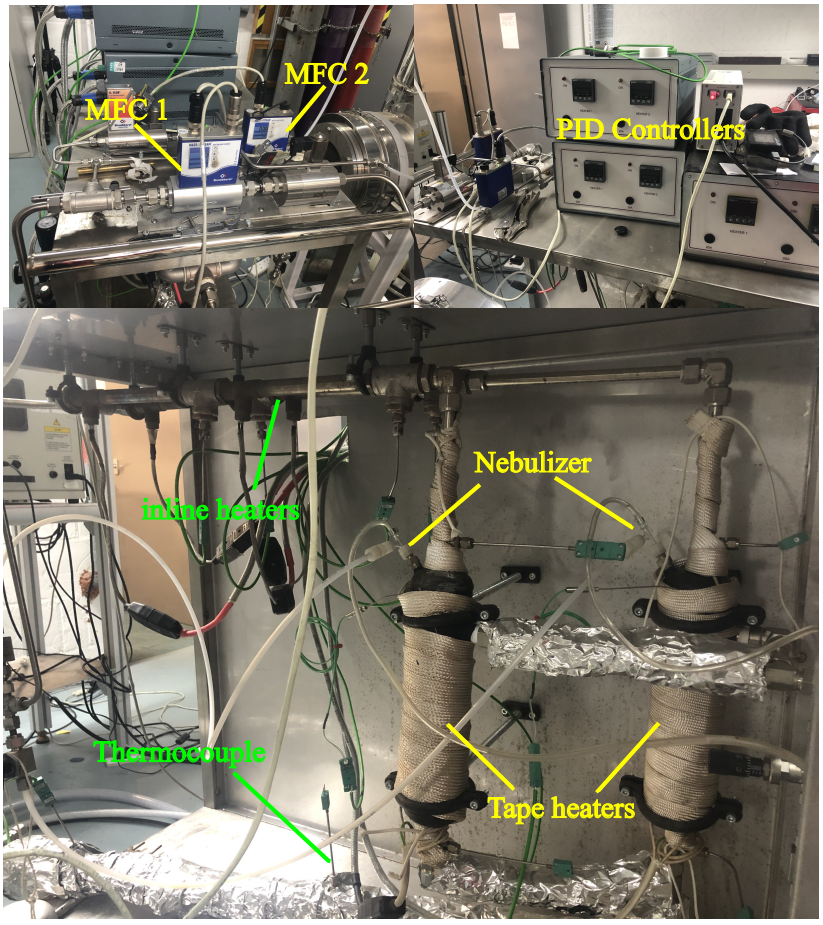

(b) Photograph of vaporiser.

Fig. 2.2 Vapourising system (a) Schematic of the vapouriser. (b)Photograph of the vapouriser.

The inlet air is heated using four inline air heaters, and the power of heaters was controlled with a proportional-integral-derivative (PID) controller. In Fig. 2.2b, inline heaters and PID controller is marked with a green and yellow label, respectively. The heated air is passed through two separate mixing chambers where the fuel is injected through nebulizers (Meinhard, TR-30-A10). The function of the nebulizers is to atomize the fuel and facilitate efficient evaporation. The mixing chambers are wrapped in the heating tape as shown in Fig. 2.2 to minimize heat loss to the walls. The details of the heater power are given in Table 2.3.

To ensure the mixture exiting the burner was fully vapourised, a series of Mie scattering and Phase Doppler Anemometry (PDA) measurements were made before the primary experimental campaign. Results from these measurements indicate that the vapouriser system vapourises 99.9 % of fuel. The temperature of the mixture was measured with a K-type thermocouple at the exit of the vapouriser and the burner. The temperature at the exit of vapouriser was monitored to ensure that it did not fall below the mixture's saturation temperature. A solenoid valve was installed on the fuel line to shut down the fuel supply in case of an emergency. The photograph is shown in Fig. 2.2b.

Table 2.3 Number of heater and power of heaters used in the vapourizer to preheat the air.

Heater	Number of Heaters	Power (W)
Inline	4	3000
Heating tape	2	1500

The vapourizer is designed to operate with different fuels at various equivalence ratios. Figure 2.3 shows the maximum equivalence ratio at which the vapourizer can be operated at a particular air flow rate with different fuels. The vapourizer can be operated with a maximum air flow rate of 1000 lpm at a $\phi = 0.8$ with ethanol. However, with heptane, A2, and C1, it can be operated to a maximum $\phi = 1.4$ for the same air flow rate. The maximum heat required to vapourize the fuel is calculated based on the latent heat of vapourization and flow rate of fuel as shown in Fig. 2.4.

2.1.4 Operating temperature and controller

The mixture temperature was kept above the saturation temperature in the mixing chambers and at the burner exit. The saturation temperature depends on the vapour pressure of the liquid. Vapor pressure and the corresponding saturation temperature were calculated from each liquid's properties and the amount of heat required to convert the liquid fuel into the

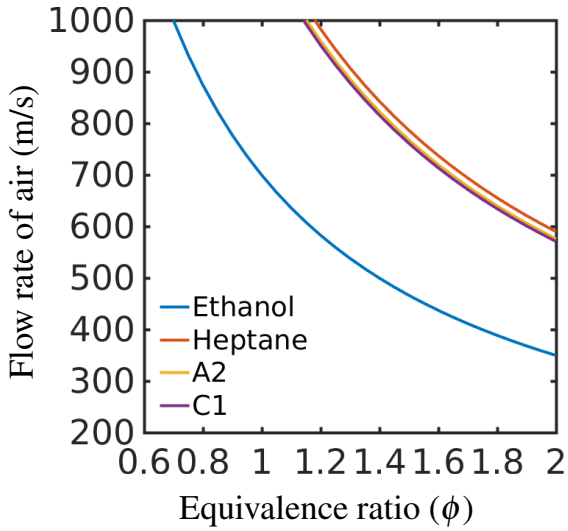

Fig. 2.3 Maximum operating equivalence ratio with different fuels at particular air flow rate.

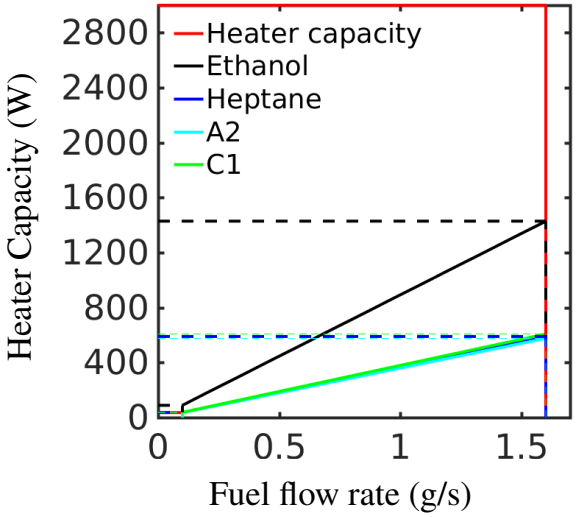

Fig. 2.4 Heating capacity of the vapourizer and maximum amount of heat required to vapourize the fuel.

vapor phase (the latent heat of vapourization). The saturation temperature at a particular equivalence ratio with different fuels is shown in Fig. 2.5.

A closed-loop PID controller is built to control the temperature of the air. The PID controllers were designed in such a way that they provide continuous power to the heaters. The amount of power provided by the PID controller is based on the difference between the temperature of the air and the set value of the temperature in the controller. An individual PID controller is used to control the heaters, and the temperature of the air is monitored to avoid the formation of hot spots.

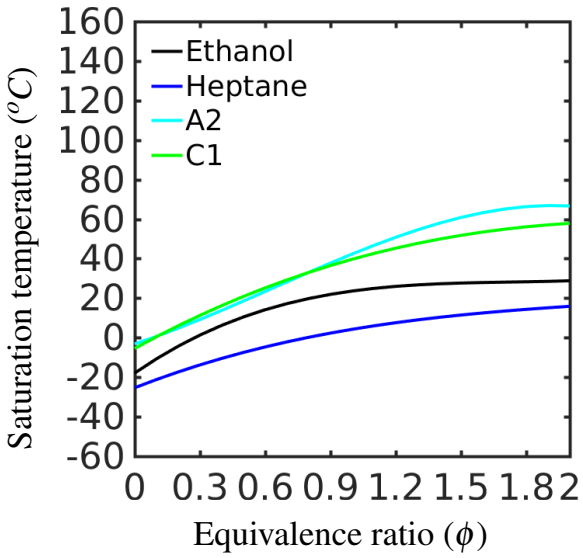

Fig. 2.5 Saturation temperature of different fuel at various equivalence ratios.

Table 2.4 Flow meter accuracy and maximum flow rate.

Type	Fluid	Maximum flow rate	Accuracy (%)
Bronkhorst	Air	1000 lpm	± 1.5
Bronkhorst	Air	50 lpm	± 1.5
Bronkhorst	Liquid	1.6 g/s	± 1.25

2.1.5 Flow rate measurements

The Bronkhorst flow controllers are used to control the air and fuel flow rate. The maximum flow rate and the accuracy of the flow controllers are given in Table 2.4. A compressed air system was used to supply the air; the airline pressure was set at 5 bar with pressure regulator and filtered with particulate and coalescent filters. A primary air flow meter (MFC 1) controls the air flow rate through the heaters and the mixing chamber. A secondary air flow controller (MFC 2) is connected with the nebulizer as shown in Fig. 2.2 and is set at a constant air flow rate. The air from MFC 2 is used to atomize the fuel. The nebulizer uses the share force to atomize the fuel into a very fine mist. A Bronkhorst Coriolis flow controller was used to inject the fuel. The flow controller has an integrated proportional integral derivative (PID) controller, which provides the controller on the liquid fuel rates. The nebulizers are connected to the fuel tank through a gear fuel pump with a transparent silicon fuel line. The silicon fuel lines were used to avoid any fuel line rust due to the different fuels used in the study. Before starting the experiments, the fuel lines are checked for air pockets and leaks.

2.2 Experimental procedures and diagnostics

2.2.1 Determination of blow-off point

The LBO was defined as the lowest equivalence ratio(ϕ) at which the flame remained visible for a given bulk velocity. The LBO was measured for a range of bulk velocities by igniting a stable fuel-air mixture (i.e. one at an ϕ of 0.9) and then reducing the ϕ in steps of 1.5 % every 20 seconds until the flame was no longer visible. The effect of reducing the fuel flow rate influences the bulk velocity by no more than 3%, which is within the uncertainty of flow controllers. The procedure was repeated five times for each fuel and flow-rate combination. The LBO points were typically within $\pm 2\%$ of each other in terms of equivalence ratio, which is within the instruments uncertainty.

The blow-off curves from different fuels were evaluated using Eq. 1.6. The term $\left(\frac{C_1}{C_2}\frac{15}{A}\right)$ in Eq. 1.6 is considered to be a constant of the order of 1, thus Eq. 1.6 can be rewritten as

$$U_{bo} = Da_{bo}^{-2}\left(\frac{S_{L,bo}^2 d}{\nu}\right), \tag{2.1}$$

where ν was evaluated at a pressure of 1 atm and the temperature of the air utilized for each condition. The $S_{L,bo}$ was also computed by considering these mixture temperatures and the specific equivalence ratio at blow-off. The mechanism used for each fuel and the corresponding $S_{L,bo}$ is given in Table 3.1.

2.2.2 OH* Chemiluminescence measurements

Chemiluminescence in turbulent flames has been widely used in various combustion applications due to its natural occurrence in the flame, avoiding external light sources. Chemiluminescence due to excited radicals (OH*, CH*, C2*, CO2*, and others) can be related to some characteristics of the flame. OH* chemiluminescence is used to obtain the information of heat release roughly and determine the location of reaction zones of fully premixed flames [29]. The electronically excited molecules emit radiations while returning to the low energy state. The emitted radiation is of a particular wavelength, and intensity can be directly related to the excited molecule concentration.

The measurement facility consists of a monochrome CMOS high-speed camera make by Photron SA1.1 and LaVision IRO high-speed two-stage intensifier with a spectral range of 190 to 800 nm. The measurements were done far from blow-off at an equivalence ratio of 0.75 and close to blow at ϕ/ϕ_{BO} = 1.01. The blow-off event is measured at 5.4 kHz with an

intensifier gated at 140 microseconds. A UV band-pass filter (270-370 mm) is fitted to the camera lens to measure the OH* chemiluminescence from the flame.

Chemiluminescence measurements are much more convenient to apply since they do not require a costly laser pump source. Still, the main limitation is that they cannot capture fine structures in flames since the signal is integrated through the depth of the flame So the interpretation of chemiluminescence data can sometimes be ambiguous, and that is why the extinction process is also examined on the burner axis by Planar Laser-Induced Fluorescence (PLIF).

2.2.3 Duration of the blow-off event

The OH* emission collected from the combustion zone using OH* chemiluminescence imaging was used to obtain the blow-off duration. Five blow-off events were measured with methane, ethanol, heptane, A2, and C1. The blow-off duration was evaluated based on the spatially integrated OH* signal decay from 50% to 5%. The 50 % upper limit was selected based on an average of five blow-off events with each fuel. As the signal drops below 50 %, it never grows back. The method was employed in Ref [29, 32] and referred to as natural blow-off to measure the blow-off duration. The premixed mixture of fuel and air was ignited at a condition far from blow-off to obtain a stable flame, and the bulk air flow rate was kept constant. The mass flow rate of fuel flow was reduced gradually such that the decrease in ϕ was in steps of approximately 0.01 every 20 seconds until the blow-off was attained. A monochrome CMOS high-speed camera (details are mentioned in Section 2.2.2) was used to record OH emission from the flame at a sampling rate of 5kHz during the blow-off and subsequently stored for post-processing.

2.2.4 Planar laser-induced fluorescence

Laser-based techniques (LIF) are very advantageous as they provide non-intrusive measurements. As the introduction of prob into the flow will disturb the flow, ultimately distorting the physics of experiments. LIF has become popular to obtain the concentration of particular molecular species in turbulent combustion since the 1980s as they provide high spatial and temporal resolution [102]. LIF is the excitation of specific molecules by laser light of a particular wavelength and then detecting the emitted photons by the excited species [103]. LIF is a point-based technique in which species information is collected from a single point with each pulse. Planar laser-induced fluorescence (PLIF) is a derivative of LIF and is a two-dimensional measurement technique. PLIF measurement involves the illumination of the flow with a laser sheet. Therefore, LIF and PLIF essentially operate on the same principles.

The difference between the two techniques the way the fluorescence signal is collected. In the LIF system, the fluorescent signal can be collected by using a photomutipler. PLIF required two-dimensional imaging equipment such as intensified CCD (ICCD) camera or intensifier fitted with a CMOS camera.

PLIF is a species and concentration-sensitive technique for the molecules being investigated. The fluorescence signal depends on the laser light's wavelengths and emission patterns for a particular species. Therefore, choosing the specific molecule to be investigated depends on the molecule's ability to provide good insight into the experiment objectives, its spectroscopy, ease of excitation, abundance, and detected fluorescence signal of a sufficient intensity [103]. In the current study, PLIF measurement of OH, CH_2O, and fuel were performed, and the details are provided in the next sections.

OH-PLIF system

Planar laser-induced fluorescence (PLIF) imaging of OH was performed to identify the product region of high temperature and subsequently visualize the 2-D topological structure of the flames considered here. OH is the most crucial species in chemical kinetic models and is found in relatively high concentration in flame. OH is a relatively long-living intermediate at a higher temperature. It can be found in regions with no high reaction rates and provide a strong signal. Therefore OH radial is the most common chosen radial in PLIF imaging. Moreover, OH can be used as a boundary to distinguish between the burnt and unburnt regions. Previous experiments with premixed flame [29, 28, 36, 20] and non-premixed used OH-PLIF imaging to study the structure of stable and transient nature of blow-off. Ref. [29] used OH-PLIF imaging with methane and ethylene in a similar burner configuration. Other studies [30, 36] used OH-PLIF imaging to study the structure of propane flame. The OH-PLIF imaging in the present work is used to investigate the flame structure at conditions far from and close to blow-off with four fuels. OH-PLIF imaging was also used to identify the hole or local extinction of the flame. Due to 2D imaging of the flame identifying the hole and local extinction is difficult due to the out-of-plane motion. Therefore caution should be paid while interpreting the local extinction events from the 2D images. In the current study, extinction is defined when the OH-LIF signal completely disappears.

The quenching (or collisional quenching) rate is of primary importance to obtain an accurate LIF measurement. Quenching represents energy loss of the molecule by some pathways other than the fluorescence. The different possibilities include dissociation, collision with other molecules, ionization, chemical reaction, or transitions to unmonitored molecular energy states. To avoid errors introduced by unknown quenching rates, generally saturated LIF is performed, which involves excitation with a high-intensity laser. The quenching rate

is low compared to absorption and stimulated emission rates. This also has the advantage of maximizing the fluorescence signal strength. A distinctive feature of planar LIF is that the imaging resolution is controlled not only by the camera and its associated collection optics but also by the laser beam optics. For instance, the thinner a laser beam is focused, the higher the resolution.

To conduct these measurements, a SIRAH Credo high-speed dye laser was pumped by a solid-state Nd:YAG laser (model JDSU Q201-HD), which output radiation at 532 nm with a power of 14 W at 5 kHz and a pulse duration of 18 ns. The tunable dye laser produced a beam near 566 nm, which was then frequency doubled using a BBO crystal to produce a beam near 283 nm with an average power of 300 mW at 5 kHz (60 μJ/pulse). The frequency-doubled output was tuned to excite the $Q_1(6)$ line in the $A^1\Sigma - X^2\Pi$ (v' = 1,v" =0) band of OH. A wavelength (λ_{length}) calibration for the OH-PLIF laser was performed at the start of each experiment by maximizing the signal from a stable flame. Shifts in λ_{length} were not apparent during the measurements as the signal-to-noise ratio (SNR) remained constant for each of the stable flames considered during a measurement campaign. Sheet forming optics were used to produce a sheet with dimensions 32 (tall) $\times$ 0.2 (thick) mm^2. Assuming the laser sheet has a Gaussian profile, the laser sheet thickness was measured by scanning a knife-edge through it and monitoring the power and position of the knife edge.

A similar camera/IRO configuration to that for the OH* measurements was used for collecting OH-PLIF images, the only difference being that here the lens was fitted with a narrow bandpass filter of 310 ± 10 nm (Edmund, 34980), and the IRO was operated with a gate of 300 ns. The camera was mounted perpendicular to the laser sheet.

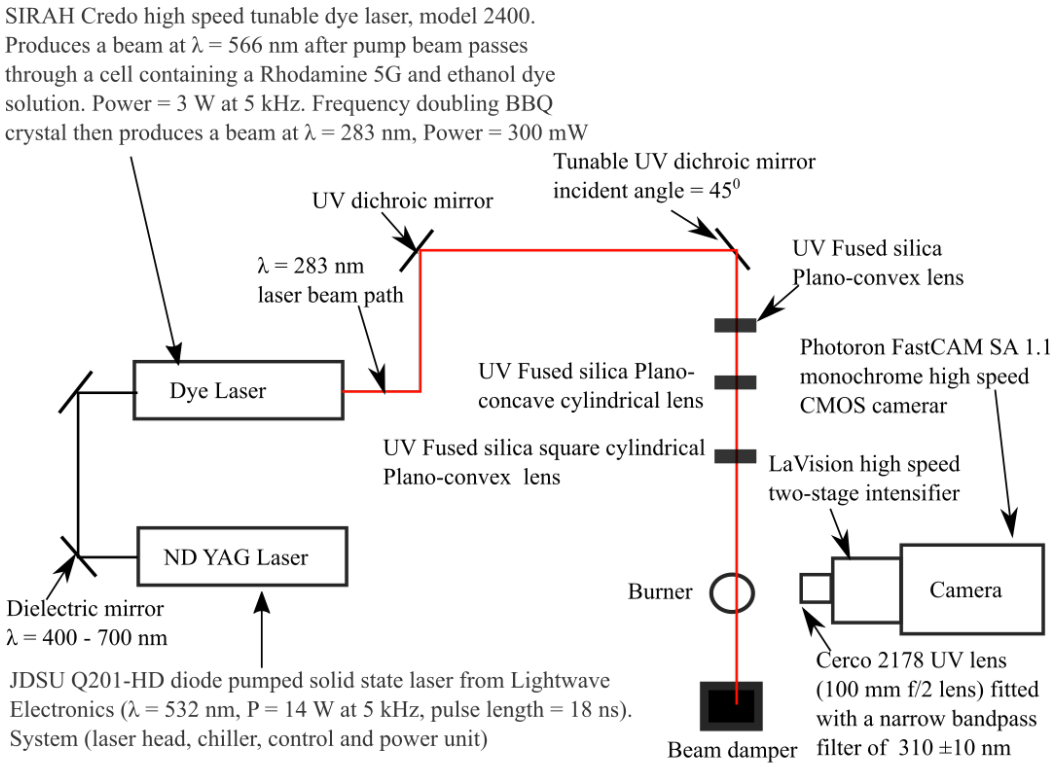

(a) Schematic of OH-PLIF system

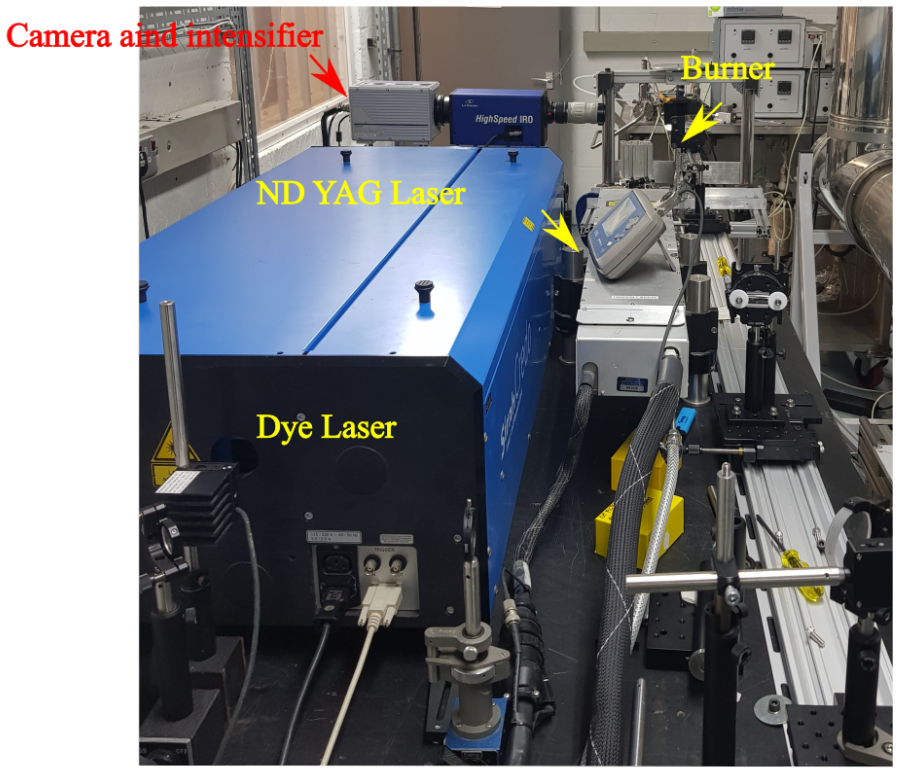

(b) Photograph of OH-PLIF system

Fig. 2.6 Details of OH-PLIF system. (a) Schematic of OH-PLIF system, showing the details of laser, camera and optical setup. (b) Pictorial view of the OH-PLIF system.

The FOV is 40 (tall) $\times$ 40 (wide) mm^2, giving a pixel projected size of $\sim$46 μm. By implementing a *scanning-knife-edge* technique [104, 105] the actual in-plane resolution was determined to be 280 μm. The images were cropped to remove portions of the frame void of laser radiance, resulting in an imaged area of 32 $\times$ 40 mm^2. The OH-PLIF images were corrected for the non-uniformities in the laser sheet by dividing each instantaneous OH-PLIF image with the average laser-sheet profile as shown in Fig. 2.7, which was obtained by imaging the laser sheet as it passed through a cell containing an optically dense mixture of Rhodamine and ethanol. Note that wavelength (λ_{length}) calibration was performed at the start of each day by maximizing the signal from a stable flame, and shifts in λ_{length} were not apparent during the measurements as the signal-to-noise ratio (SNR) remained constant ($\approx$ 6:1). Here, SNRs were computed as in [106] by dividing the average signal within a region by the standard deviation of the signal within that region.

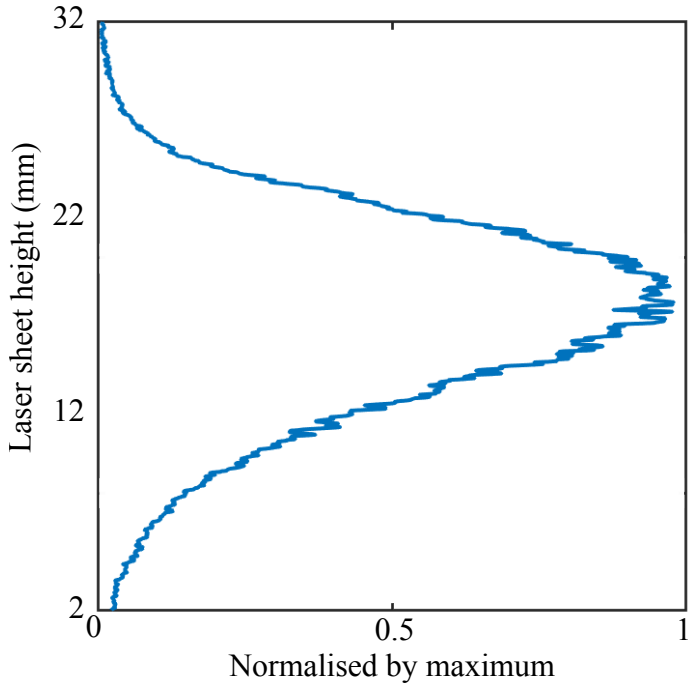

Fig. 2.7 Normalized laser profile with OH-PLIF system. Y-axis represents the height of the laser sheet.

CH_2O-PLIF system

PLIF imaging of CH_2O was performed as a means to visualize the preheat regions of the flame [50, 47–49, 107–110]. Specifically, the experimental and numerical results of Li et al. [111] suggested that in methane-air flame CH_2O-LIF signal can serve as the marker of preheat regions. This is further corroborated with the simulation results of 1D flame

presented in Fig. 3.3. Fig. 3.3 demonstrated that the CH_2O concentrations lies upstream of the reaction layer.

The frequency-tripled output (near 355 nm) from a low speed (10 Hz) Nd:YAG laser (Continuum Surelite, Electro-optics, INC) with pulse energies of ∼100 mJ was used to excite multiple transitions within the 4_0^1 band of the $A^2A_1 \longleftarrow X_1A^14_0^1$ system of CH_2O. Sheet forming optics (a 38−mm cylindrical concave lens and a 500−mm spherical biconvex lens) were used to produce an expanded sheet with dimensions 52 (tall) × 0.25 (thick) mm^2. The laser sheet thickness was measured using the same method to determine the 283-nm sheet thickness (see Section 2.2.4).

Fluorescence was collected by an intensified CCD camera (LaVision, Nanostar) that was mounted perpendicular to the laser sheet. The camera was operated with a gate of 100 ns and was equipped with a Zeiss 100 mm f/2 lens, which was fitted with a multi-band filter (FF01-CH2O-50). The pixel array was binned 2 × 2 before read-out, yielding a final sensor size of 512 (tall) × 640 (wide) $pixels^2$. This array imaged a 47 (tall) × 59 (wide) mm^2 region, giving a pixel projected size of ∼92 μm. This imaging system's resolution (full width at half maximum of the line spread function) was determined to be ∼ 240 μm using the scanning knife-edge technique [104, 105].

As shown by Orain et al. [112], components of kerosene fuels tend to emit broadband fluorescence when excited via a UV laser source. Thus, the fluorescence resulting from passing a 355-nm laser sheet through the kerosene flames is likely to result from CH_2O as well as un-reacted components of the fuel. Therefore, the present technique for CH_2O-PLIF imaging in the kerosene flames results in ambiguous LIF signals. To crudely assess LIF signals' influence resulting from unburned fuel, the frequency-quadrupled (near 266 nm) output from the same laser system employed for the CH_2O-PLIF imaging was used to facilitate vapourized fuel fluorescence imaging. Further details of this assessment are provided in Section 2.3.3.

It should be stressed that the PLIF results obtained here are purely qualitative. Rendering such quantitative measurements is a formidable task that requires knowledge of the local temperature and the surrounding concentrations of major species. As in most studies, such quantities were unavailable here. Thus, to facilitate fair comparisons between measured and simulated results, the CH_2O mole fractions from the latter were corrected to account for Boltzmann fraction distributions, collisional quenching effects associated with the finite resolving power of the PLIF-imaging system. The results of these corrections are provided in Section 3.1.

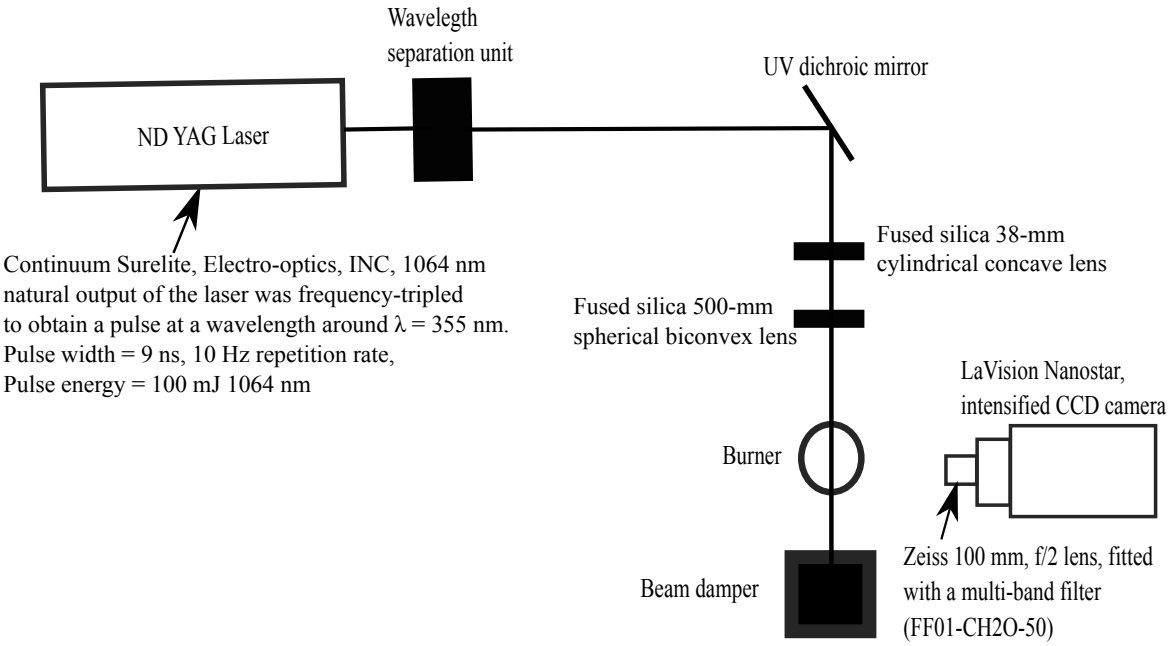

(a) Schematic of the CH_2O-PLIF laser.

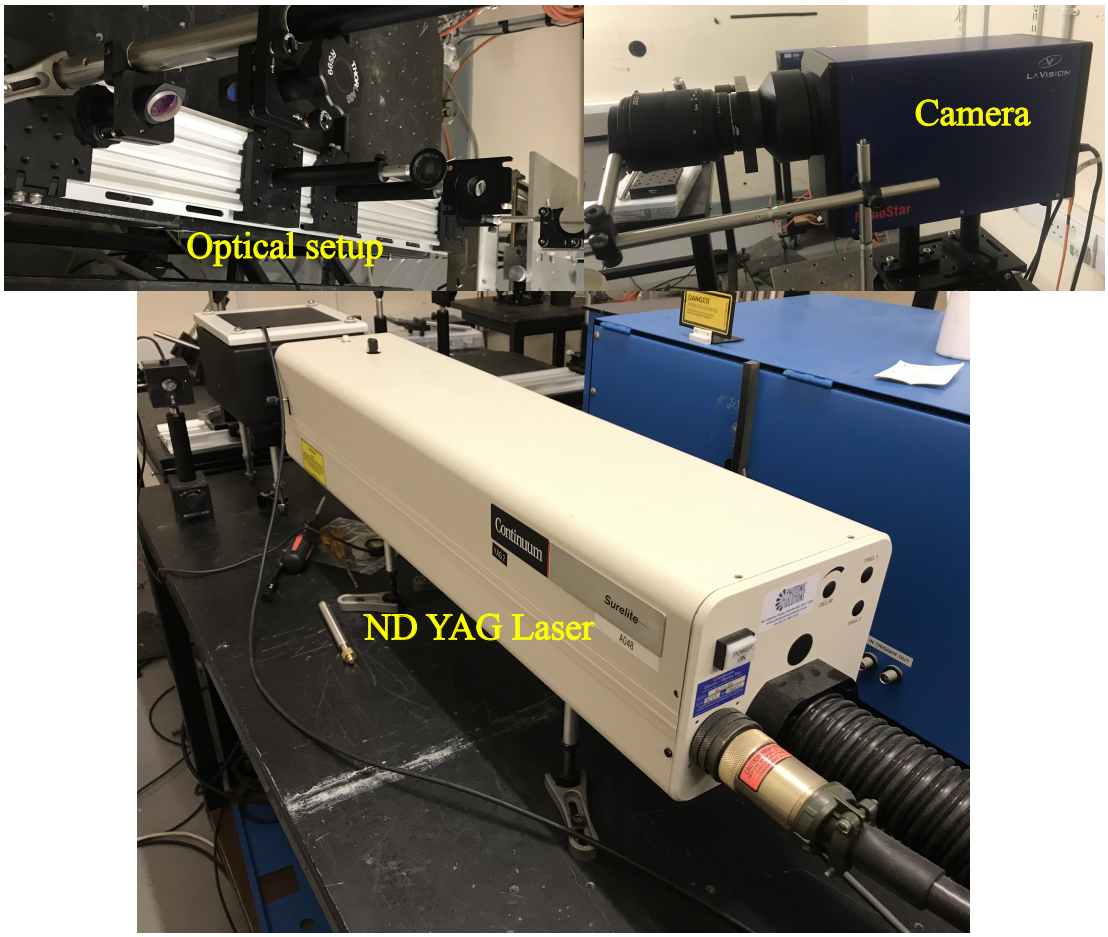

(b) Pictorial view of the CH2O-laser setup..

Fig. 2.8 Details of CH_2O-PLIF system. (a) Schematic of CH_2O-PLIF system, showing the details of laser, camera and optical setup. (b) Pictorial view of the OH-PLIF system..

Fuel-PLIF system

The same laser setup was used to obtain Fuel-PLIF images from the A2 flames. The only difference from the OH-PLIF was that the laser beam was detuned from the $Q_1(6)$ line to avoid the OH radical's excitation. For Fuel-PLIF, the same high-speed camera as for the OH* imaging was used. The IRO was gated at 300 ns. Since fuel fluoresces over a broad spectral range ($\sim$300 - 420 nm) [112], a long pass filter of 320 nm was instead employed for the Fuel-PLIF measurements.

2.2.5 Particle image velocimetry system

Particle image velocimetry (PIV) is an optical measurement technique used to capture flow field information. PIV system consist of several subsystems. In most applications of PIV, tracer particles are added to flow. These tracer particles are illuminated twice by using a light source. The scattered light is capture by using a recording device such as a camera. The PIV recording is used to determine the displacement of the particle between the two laser pulses.

The PIV system consisted of a solid-state diode-pump (SSDP) Nd:YLF dual oscillator/single head laser (Quantronix Darwin-Duo), which outputs radiation at 527 nm with a power of $\approx$ 27 W at 2.5 kHz (i.e. $\sim$10 mJ/pulse). The laser was operated in dual pulse mode with a pulse width of 120 ns and a pulse separation of 12 μs. A 38-mm cylindrical concave lens and a 500-mm spherical biconvex lens were used to produce a collimated laser sheet with a height of 55 mm and a thickness of $\approx$ 700 μm. To avoid reflection along the laser beam/laser sheet path, an iris and a rectangular slit were used to block the reflections.

Mie scattering from the incident laser light was collected with a high-speed camera (Photron SA1.1) operated in a frame-straddling mode with an imaging rate of 5 kHz. The camera was mounted perpendicular to the laser sheet and was equipped with 105-mm f/2.8 lens (Nikon) lens fitted with $527 \pm 20m$m filter. The 1024 $\times$ 1024 pixel^2 sensor of the camera imaged a 65 $\times$ 65 mm^2 region, yielding a projected pixel size of $\sim 63\mu$m.

The accuracy of the PIV measurement depends on how closely the tracer particle follows the flow. For this reason, to attain high accuracy in the measurements, the flow was seeded with Al_2O_3 particles with a nominal diameter of 0.3μm. The Al_2O_3 particles have a high melting point of 2323 K, and a high refractive index ($\approx$ 1.8), therefore it can scatter incident light without any adverse effect on the flame, such as quenching. The Stokes number associated with these particles is 0.001. Thus they can trace the flow fluctuations in the range of 0.9 MHz, which is within the range of the small-scale turbulent motions expected in this flow. The PIV system was applied to non- and reacting flow fields. 1000 image pairs

were collected. Vapourised heptane was used as the fuel in the reacting conditions, which considered two cases: far from and close to lean blow-off.

2.3 Image processing and data analysis

2.3.1 OH* chemiluminescence

High-speed OH* chemiluminescence was used to characterize the flame shape. OH* can be used to roughly estimate the localized heat release in flames [113]. The average flame shape was obtained by averaging 5400 instantaneous OH* chemiluminescence images. Since the overall flame was axisymmetric, as shown in section 6.1, The average OH* images were Abel transformed with an assumption of axisymmetry to provide an approximate location of the mean reaction rate. The mean images were chosen as the axisymmetry assumption is not valid on instantaneous images.

2.3.2 OH-PLIF

The OH-PLIF images were analyzed by employing a detailed image processing routine. First, the average pixel offset (i.e., the sensor dark current), laser background, and flame chemiluminescence emissions were subtracted, on a pixel-by-pixel basis, from each image. Following this subtraction, the instantaneous images were corrected for laser sheet inhomogeneities. The images were then median filtered with a kernel size of 5×5 pixels^2 to increase the signal-to-noise ratio (SNR) to 6:1 (here, as in Ref. [106], SNR is defined as the ratio of the average to signal intensity to its RMS within a small region). Figure 2.9a shows a sample of the raw image. Different values of the threshold are applied to the raw images to obtain the optimal thresholding value. Figure 2.9b displays the binary images with 10 %, 20 %, 30 % and 40 % threshold. The signal in the OH-PLIF images started disappearing with a threshold value of more than 30 %. Therefore, 20 % threshold is used in this study. Additionally, a similar binarization method (i.e., one based on the 20% contour) was employed in Ref. [29, 114].

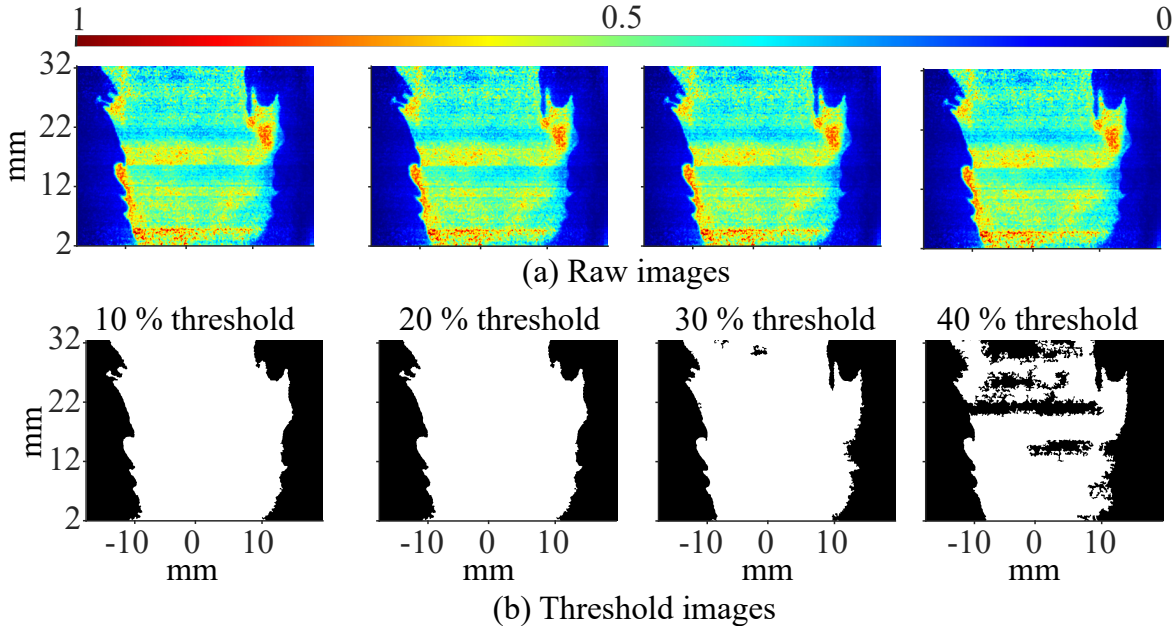

Fig. 2.9 Images showing the instantaneous raw OH-PLIF image (row 1) and binarized image (row 2) at different thresholding value with A2 flame at $U_b = 23 \pm 1.5$ m/s and $\phi = 0.75$.

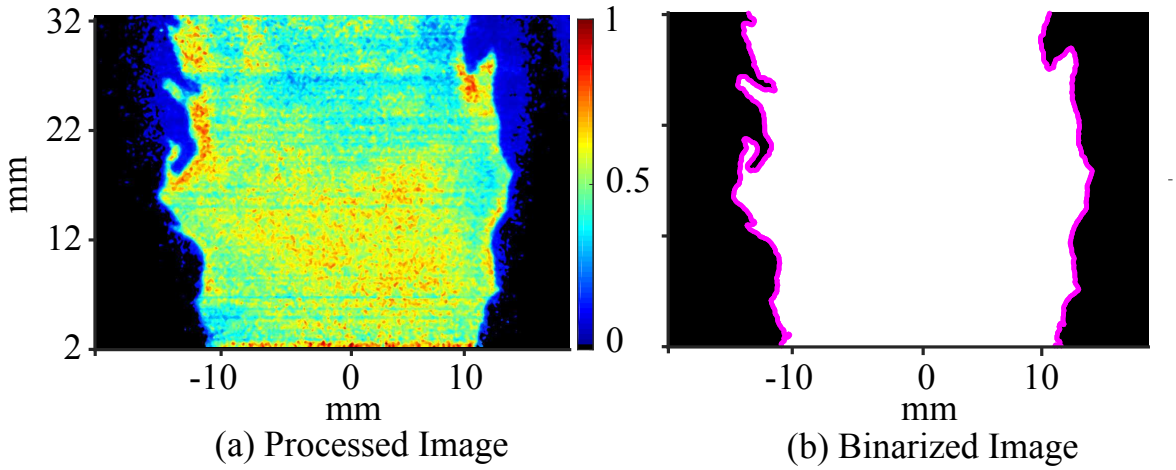

Fig. 2.10 Images showing the instantaneous OH-PLIF image after correction, binarized and edge image with A2 flame at $U_b = 23 \pm 1.5$ m/s and $\phi = 0.75$.

A sample OH-LIF image that was subjected to the aforementioned correction process is displayed in Fig. 2.10a. The processed images were then binarized based on their 20% contour, assuming that the regions with intensities greater than 20% of maximum correspond to burnt gas and all other regions represented unburnt gas. The edges corresponding to these contours were extracted from each image and are marked by the magenta lines superimposed on a sample binary image in Fig. 2.10b. The mean progress variable $(\bar{c})$ was determined by

averaging the complete data set of binarized images as shown in section 6.3. These binarized edge images and progress variable maps were used to obtain flame surface density (FSD) and 2-D flame-front curvature information. Further details of which are provided in section 6.4 and 6.5.

2.3.3 CH_2O-PLIF

Formaldehyde LIF (CH_2O) was used to study the effect of fuel composition on the CH_2O layer, but the images were not used to quantify CH_2O concentrations. Similar background corrections to those applied to the OH-PLIF images were also applied to the CH2O-PLIF images. The images were then median filtered with a kernel size of 3×3 pixels^2 to increase the SNR to 5:1. Sample images from before and after this correction process are displayed in Figs. 2.11a and 2.11c, respectively. Note, the laser sheet used for the CH_2O-PLIF measurement was well expanded, and the vertical variation in the energy was negligible [115]. Thus, no laser sheet corrections were performed on the CH_2O-images.

Note that additional low-level fluorescence was observed in the reactant region of the flames in the case of the kerosene fuels. This low-level signal is attributed to fuel fluorescence [112, 116], which was confirmed by implementing Fuel-PLIF imaging via excitation near 266 nm. A sample Fuel-PLIF image acquired from an A2 flame is provided in Fig. 2.11b. Additionally, Fuel-PLIF images showed a uniformly distributed signal which confirms that most of the fuel in the mixture was fully vapourised. It was noted that the flourance signal from C1 fuel was less than half of A2 at the same conditions. It may be due to the presence of single-ring and two-ring aromatic content in A2 compared to the near single-component iso-parrafin C1 [112, 116]. However, no flourance signal was observed in the case of ethanol and heptane flame.

Ideally, one would perform the CH_2O- and Fuel-PLIF measurements simultaneously to properly separate the signals; however, such measurements were unavailable here. Instead, by comparing CH_2O-LIF profiles obtained from flames that do not produce fuel-LIF signals (i.e., methane, ethanol, and heptane) to those that do (i.e., A2 and C1), the low-level fuel-LIF signal found within the latter was determined to be on the order of 2% of the maximum CH_2O-LIF signal in each image. Thus, an additional 2% of the maximum signal in each image was subtracted from those obtained for two kerosene fuels. However, the subtraction does not influence the results drastically though there was room for error as there was no simultaneous measurement available in the current experiment for Fuel-PLIF and CH_2O-PLIF.

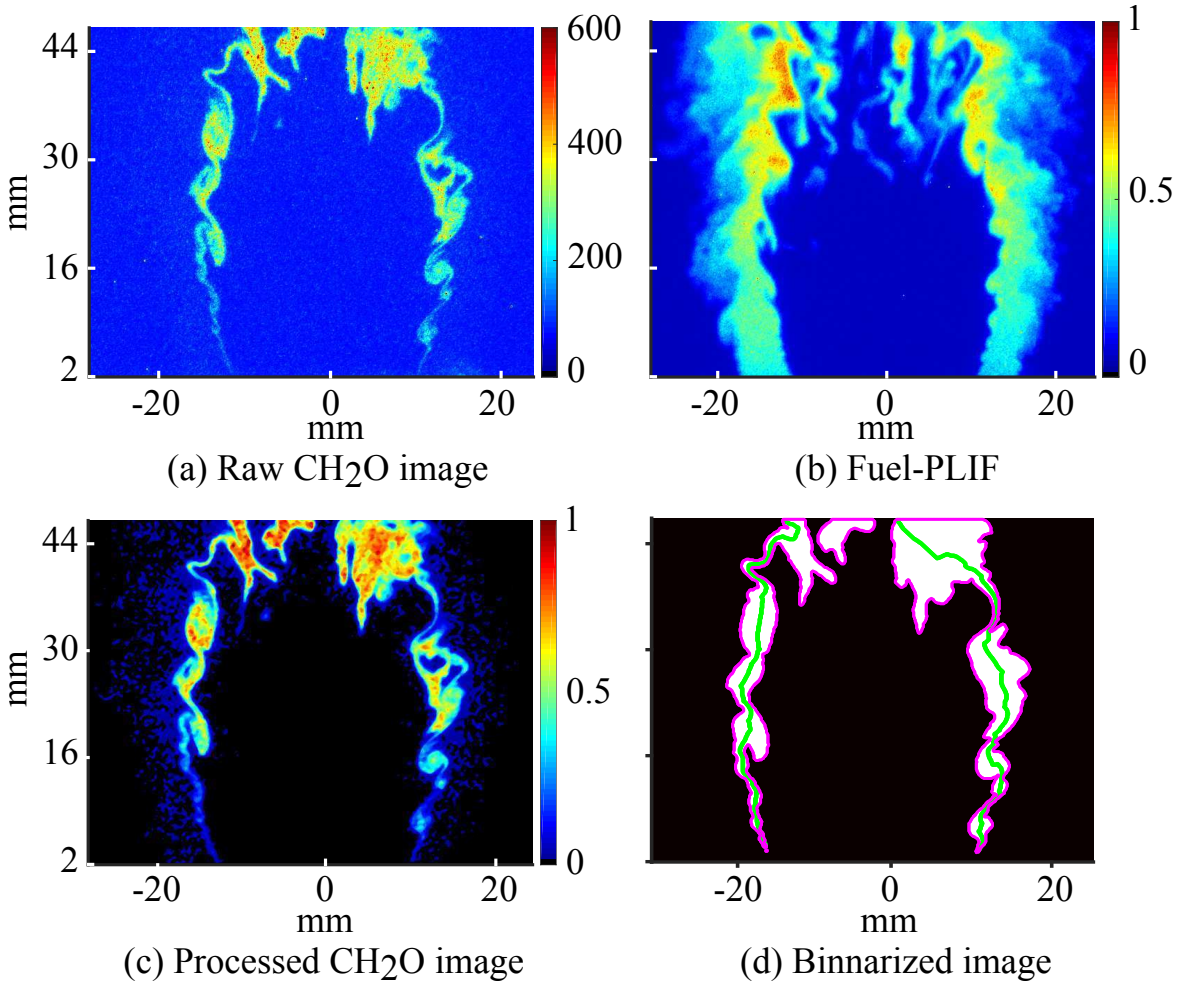

Fig. 2.11 Images showing the instantaneous CH_2O before and after correction and Fuel-PLIF image with A2 flame at $U_b = 23 \pm 1.5$ m/s and $\phi = 0.75$.

Figure 2.12 shows profiles of CH_2O-LIF signal extracted from a region ∼12 mm downstream of the burner for heptane and A2 flames under stable burning conditions. The two peaks in the plot represent the flame edge, and the laser sheet propagation is from left to right. The background signal associated with dark sensor current, non-rejected laser-light scattering, and chemiluminescence emissions (marked by the blue line) is the same for both flames. As highlighted by the blue circles in Fig. 2.12, the signal from the A2 flame starts rising before (i.e. at more considerable radial distances from centerline) that is associated with the heptane flame. As discussed in the paper section 3.6.3, this small amount of signal in the A2 flame is attributed to fuel-fluorescence and is fuel-specific [112]. It is removed by subtracting an additional 2% from the CH_2O-PLIF images collected from the kerosene-fueled flames.

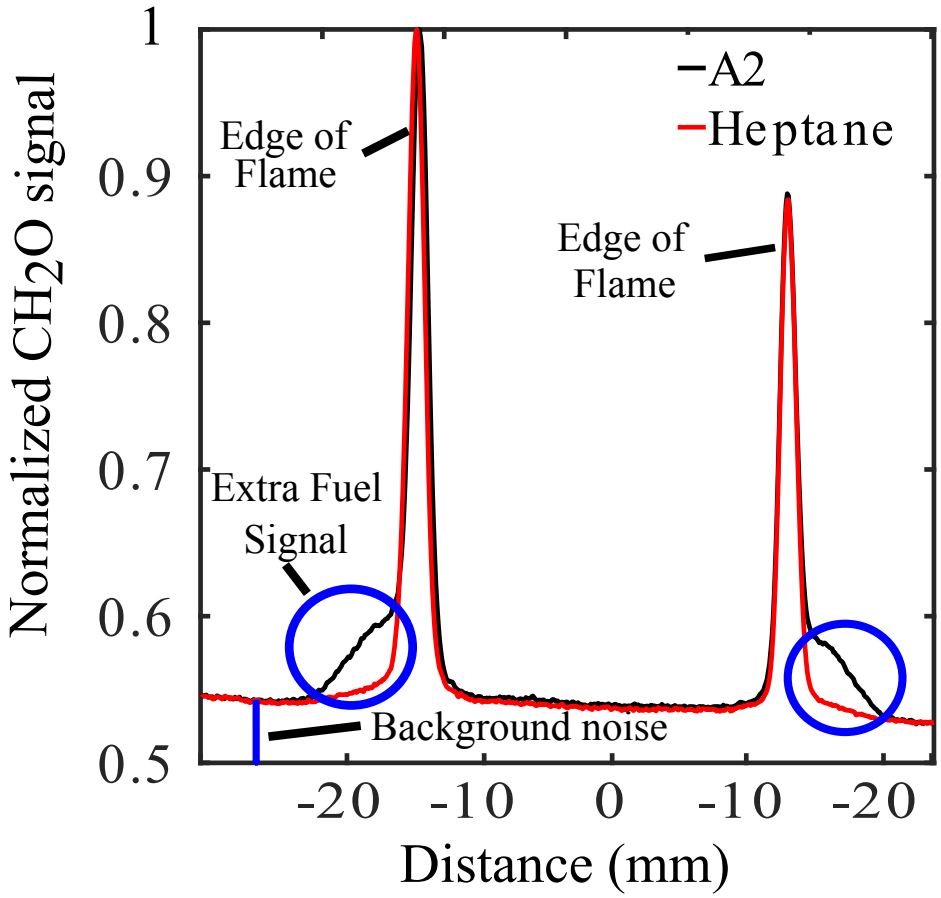

Fig. 2.12 Plot showing the average CH_2O profile with heptane and A2 flame along the horizontal axis of the burner at a distance 10-13 mm from the burner exit. The axis of the burner is represented by '0' on the plot.

The CH_2O thickness was calculated from the corrected CH_2O-PLIF images following the scheme implemented in Ref. [50]. In particular, to estimate the CH_2O-layer thickness from the instantaneous images, a dynamic thresholding scheme was performed. Following this thresholding, a contour of 10% (magenta line in Fig. 2.11d) was extracted from each image. Based on these contours, each image was binarized, and the skeleton of each binarized layer was identified. A sample binarized image with its skeleton overlaid (green line) is shown in Fig. 2.11d. As in Ref. [50], the distance from each skeletal point to the nearest edge point (10% contour) was determined and multiplied by a factor of two to give the full width at 10% of maximum at each skeletal location. Subsequently, this information was compiled into probability density functions (PDFs) of thickness that were normalized by their respective values of simulated laminar flame thickness, $\delta(l)^*_{CH_2O}$ (see Table 3.1).

2.3.4 Flame surface density

The 2-D FSD (Σ_{2D}) represents the amount of flame surface area per unit volume at a given point and instant within the reacting flow field [86]. In the present work, Σ_{2D} represents a 2D estimate of the full 3D-FSD. As shown by Bell et al. [117] and Veynante et al. [118], the 3D-FSD is expected to be $\sim$1.3 times larger than that of the 2-D FSD; however, this does not invalidate comparisons between the separate flames considered here. The 2-D FSD was calculated by using the method of Shepherd [86], which was also employed in other studies [29, 37]. The method introduced by Shepherd [86] provides an estimate of Σ_{2D} and is defined as:

$$\Sigma(\bar{c}) = \frac{L(\bar{c})}{A(\bar{c})}, \tag{2.2}$$

where $A(\bar{c})$ and $L(\bar{c})$ are flame zone area and total flame-front length, respectively. In the current study, $A(\bar{c})$ was calculated from the average progress variable image $\bar{c}$, shown in Figs. 6.7a and b. Namely, the $A(\bar{c})$ maps were divided into 10 sectors that corresponded to 10 specific values of $\bar{c}$ (referred to as $\bar{c^*}$). Each sector was centered about these $\bar{c^*}$ values such that they were defined as: $\bar{c^*} \pm \Delta\bar{c}/2$, where $\Delta\bar{c}$ = 0.05, which was selected as it provided the best balance between the noise and resolution in the computed FSD-field [37]. $L(\bar{c})$ was then determined by summing all 5400 edge-images and determining the total flame length occupying the area covered by each individual $\bar{c}$-sector.

2.3.5 2-D curvature

The 2-D flame-front curvature was evaluated along the iso-contours of instantaneous edge images. The flame edge coordinates, corresponding to the 20% contour of the OH-PLIF images, were obtained from each image and were subjected to 1-D wavelet-based filtering to remove artifacts associated with the discrete nature of the images. A sample OH-PLIF image with its extracted edge is shown in Fig. 2.10b. The 2-D curvatures of these edges were measured by calculating the first and second derivatives in the x and y direction along with them (as in Ref. [29, 119]). Eq. 2.3 was used to calculate the local curvature (κ).

$$\kappa = \frac{(\dot{x}\ddot{y} - \dot{y}\ddot{x})}{(\dot{x}^2 + \ddot{y}^2)^{3/2}} \tag{2.3}$$

where $\dot{x} = dx/ds$ and $\ddot{x} = d^2x/ds^2$. The flame segments that are convex towards the reactants are defined with positive curvature and vice versa. The laser sheet thickness used to evaluate the curvature was $\approx 200\mu$m, and the resolving power of the imaging system is $\sim 280\mu$m. Thus, the minimum curvature that could be resolved based on the imaging system is estimated to be ~ 2 mm^{-1}.

2.3.6 PIV processing

Vector calculation of the images was performed with commercial software (Davis 8.3). Prior to processing, the average pixel offset (i.e., the value without laser-light present) was removed from each image. A multi-pass cross-correlation algorithm was used with an initial interrogation window size of 24 $\times$ 24 pixel^2 with 50% overlap and a final window size of 12 $\times$ 12 pixel^2 with 75% overlap. Such processing yields a vector spacing of $\sim$189μm and an interrogation window size of $\sim$760μm. Based on an estimated integral time scale of 0.22 ms and imaging frequency of 2.5 kHz. The total number of independent samples was $\approx$ 920. This leads to maximum relative errors of convergence in the mean and variance of $\approx$ 1% and $\approx$ 4% [120].

2.4 Summary

Three different PLIF measurements were used to study the structure of the flame. For convenience, a summary of three PLIF diagnostic techniques is provided in Table 2.5. Table 2.5 presents in-and out-of-plane resolutions and signal-to-noise ratios (SNRs) estimations for the images gathered in this study. The SNR was determined for PLIF images by applying the median filtering and the average signal in the particular region was divided by the standard deviation of that signal within that region.

Table 2.5 Diagnostics details of PLIF systems. The in-plane resolutions represent the FWHM of the line spread functions (LSFs) associated with each imaging system (prior to the application of filters). The out-of-plane resolutions represent the thickness (FWHM) of the laser sheets, which were determined via a scanning knife-edge method. "PPS" stands pixel projected size.

Diagnostics	Rate	PPS	In-plane	Out-of-plane	SNR
OH-PLIF	5.0 kHz	46μm	240 μm	0.22 mm	6.1
Fuel-PLIF	5.0 kHz	46 μm	240 μm	0.20 mm	6.1
CH_2O-PLIF	10 Hz	92 μm	240 μm	0.25 mm	5:1

For the PIV measurements, the laser sheet thickness was $\approx$ 700 μm and the imaging system at full resolution yielded a pixel projected size of $\approx$63μm. At the frequency of 2.5 kHz, the total number of independent samples was $\sim$ 920 with the maximum relative errors in estimating the mean and variance of $\approx$ 1 % and $\approx$ 4 %.

Chapter 3

Laminar flame simulation

An analysis of unstrained and strained (counterflow premixed twin flame) laminar flame simulations using Cantera [121] is presented in this chapter. Simulations were conducted at the same pressure and temperature as the experiments, i.e., at a reactant pressure of 1 bar and a temperature of 393 K. A description of the mechanism is provided in Table 3.1. The fuels used are methane, ethanol, heptane, A2, and C1. Simulations were performed to obtain laminar flame speeds, extinction strain rates, and laminar flame structure for interpretation of blow-off curves and flame images in the following chapters.

For the laminar premixed flame calculations, the adiabatic temperature (T_{ad}) across a flame, and for twin-premixed flame calculations, extinction strain rates are obtained for various equivalence ratios for all five flames. Extinction strain rates of only premixed twin flames were obtained, not counterflow premixed flames stabilized in a strained flow field, with opposite flow formed from equilibrium products, as these flames had unrealistic extinction strain rates.

3.1 Laminar flame speed

One-dimensional, premixed, and freely propagating laminar flame calculations were performed using Cantera [121]. These simulations were performed at a reactant pressure of 1 bar and a temperature of 393 K. The detailed chemistry details and transport properties to obtain the laminar flame speed, S_L, and to compute the laminar flame structure in terms of profiles of temperature T, species mole fraction, especially the mole fraction of OH and CH2O (the PLIF of the two radicals is measured in the following experiments). The fuels used are methane, ethanol, heptane, A2, and C1.

The detailed mechanisms used in the laminar flame simulation are provided in Table 3.1. For methane flame simulation, USC Mech II [122] high-temperature oxidation kinetic model (111 species and 784 reactions) was used. Marinov [123] proposed a kinetic model with 56 species and 351 reversible reactions for ethanol. Heptane flames were simulated using a detailed kinetic model by Smallbone et al. [124] with 955 reactions and 130 species. To simulate the kerosene (A2 and C1) flame chemistry model based on a hybrid approach proposed by Ref. [125, 126] was used. In the hybrid chemistry approach, the fuel's kinetics of thermal and oxidative pyrolysis are modeled using lumped kinetic parameters.

Table 3.1 Freely propagating laminar flame simulation results. The composition of A2 and C1 are provided in Table 2.1

Fuel	Mechanism	ϕ	S_L (cm/s)	$\delta(l)_{CH_2O}$ (mm)	$\delta(l)^*_{CH_2O}$ (mm)	δ_l (mm)
Methane	USC Mech II [122]	0.75	39.37	0.57	0.8	0.48
		0.61	23.28	1	1.1	0.68
Ethanol	Marinov [123]	0.75	44.97	0.46	0.60	0.41
		0.641	31.70	0.6	0.8	0.51
Heptane	Smallbone et al. [124]	0.75	43.50	0.50	0.70	0.42
		0.635	30.43	0.65	0.8	0.52
A2	HyChem (POSF10325) [125]	0.75	40.09	0.52	0.75	0.44
		0.68	33.07	0.68	1	0.48
C1	HyChem (POSF11498) [126]	0.75	36.91	0.54	0.70	0.46
		0.71	33.43	0.71	0.8	0.48

Figure 3.1 presents the unstrained flame speed (S_L) for methane, ethanol, heptane, A2, and C1. The computed S_L values were around the experimental values given in Refs [7, 127, 122–126] and within. The trend in S_L with ϕ is captured well for different fuels. Ethanol and

heptane exhibit higher values of S_L than the other three fuels. A2 and methane displayed almost the same S_L, and C1 showed the lowest S_L. At $\phi \approx 1$, the difference in S_L is more prominent than lean and rich conditions. In lean conditions at $\phi < 0.75$, the difference in S_L for separate fuels is not huge, as shown in Fig. 3.1. Figure 3.1b represents the adiabatic flame temperature (T_{ad}) with separate fuels studied here. The T_{ad} curves align close to each other for separate fuels. The T_{ad} peaks around $\phi \approx 1.1$, with maximum value of $T_{ad} \approx 2300$ K. At $\phi \approx 1$, the ethanol and methane showed a lower value of T_{ad} compared to heptane, A2 and C1. The range of ϕ studied in the current flame heptane, A2 and C1 showed almost equal T_{ad}. In lean and rich conditions, the difference in T_{ad} decreases between separate fuels.

Table 3.1 shows the calculated value of S_L, laminar flame thickness (δ_l) and laminar CH_2O thickness ($\delta(l)_{CH_2O}$) at ϕ = 0.75 and at ϕ/ϕ_{BO} = 1.01 (based on the results presented in Chapter 4). The δ_l is computed based on the relation $(T_{max} - T_{min)}/(max(\delta T/\delta x))$, where T is the temperature. The thickness of the simulated CH_2O profiles ($\delta(l)_{CH_2O}$), was defined here as the full width at 10% of maximum. It can be seen from Table 3.1, S_L decrease, δ_l, and $\delta(l)_{CH_2O}$ increases as blow-off is approached. At blow-off, A2 and C1 had the highest S_L, methane showed the lowest value, where as ethanol and heptane showed S_L in between. In lean conditions, it was noticed that methane had the highest value $\delta(l)_{CH_2O}$ and both kerosene (A2 and C1) showed the lowest value.

To facilitate fair comparisons between the simulated and measured CH_2O-layer thicknesses, the former were corrected to account for Boltzmann fraction distributions, collisional quenching, and effects associated with the finite resolving power of the PLIF-imaging system. Namely, the formulation put forth in Kyritsis et al. [128] was used to account for the temperature dependence resulting from the population distribution of the ground laser-coupled state of CH_2O. Additionally, as in Refs. [129–131], the collisional quenching cross-sections were assumed to have a temperature dependence of $T^{-0.5}$ such that the total collisional quenching rate was proportional to T^{-1}. Finally, as in Refs. [132, 133], a Gaussian filter with a standard deviation corresponding to that of the measured line spread function associated with the imaging system ($\sim$250 μm) was applied to the temperature-corrected, simulated CH_2O profiles to account for the blur induced by the finite resolution of the imaging system. The corrected laminar CH_2O-layer thicknesses are referred to as $\delta(l)^*_{CH_2O}$. The results of these corrections are presented in Table 3.1. The intent of obtaining the corrected laminar CH_2O thicknesses ($\delta(l)^*_{CH_2O}$) was to normalize the experimentally obtained CH_2O-layer thicknesses ($\delta(l)_{CH_2O}$) as shown in Chapter 5.

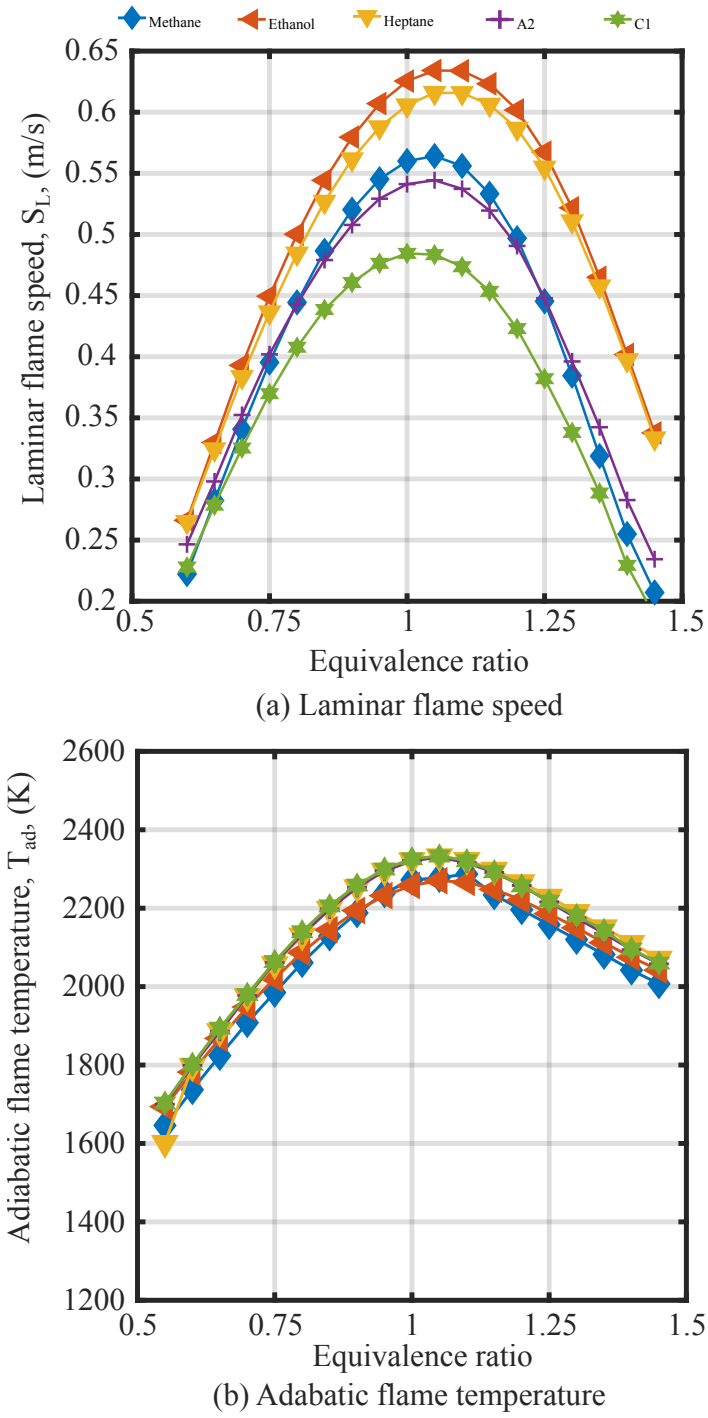

(a) Laminar flame speed

(b) Adabatic flame temperature

Fig. 3.1 Laminar flame speed with different fuels. The simulation were run at 393 K and 1 bar atmospheric pressure.

3.2 Species distribution in laminar flame structure

Figure 3.2 the mole fraction of OH and CH_2O computed from the laminar flame simulation with progress variable (z). The z is defined based on the temperature. Ethanol showed the highest value of OH and CH_2O, which is likely due to ethanol's chemical composition. Namely, each ethanol molecule contains OH through a single bond, which likely breaks away from the rest of the molecule as the fuel cracks, resulting in locally higher concentrations. A2 and C1 showed almost the same mole fraction of OH. On the other hand, A2 showed a lower mole fraction of CH_2O compared to methane and other fuels.

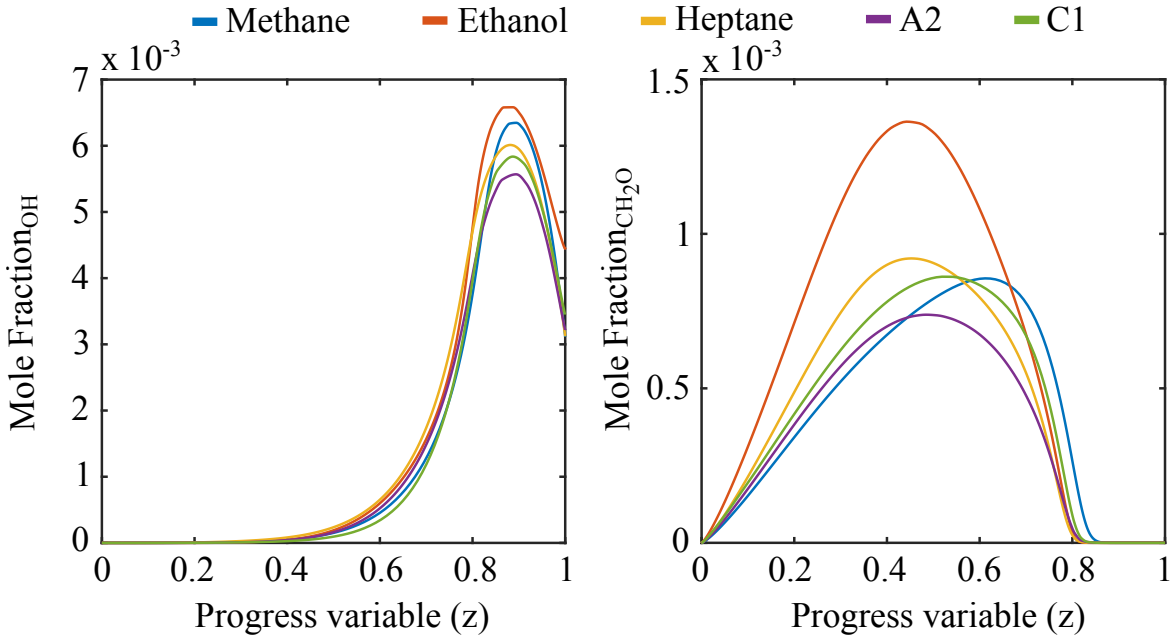

Fig. 3.2 Plot showing the mole fraction of OH and CH_2O (phi=0.75) with different fuels. The progress variable (z) is defined based on the temperature.

As expected, CH_2O is produced in the preheat zone/low-temperature regions see Fig. 3.3, peaks in the mid-temperature range (1200 K to 1400 K), and consumed in the high-temperature regions ($>$ 1700). On the contrary, OH is produced in the high-temperature regions where CH_2O decreases and the amount of OH is high in the post flame region. The trends in OH and CH_2O are in agreement with Refs. [36, 134]. The peak CH_2O was observed to occur at 1200 K for methane. In contrast, for kerosene (A2 and C1), the peak value of CH_2O occurs at a higher temperature, around 1400 K. This may be due to the chemical models employed to calculate the laminar flame simulation and further investigation of the reaction pathway is required, which is out of the scope of this dissertation.

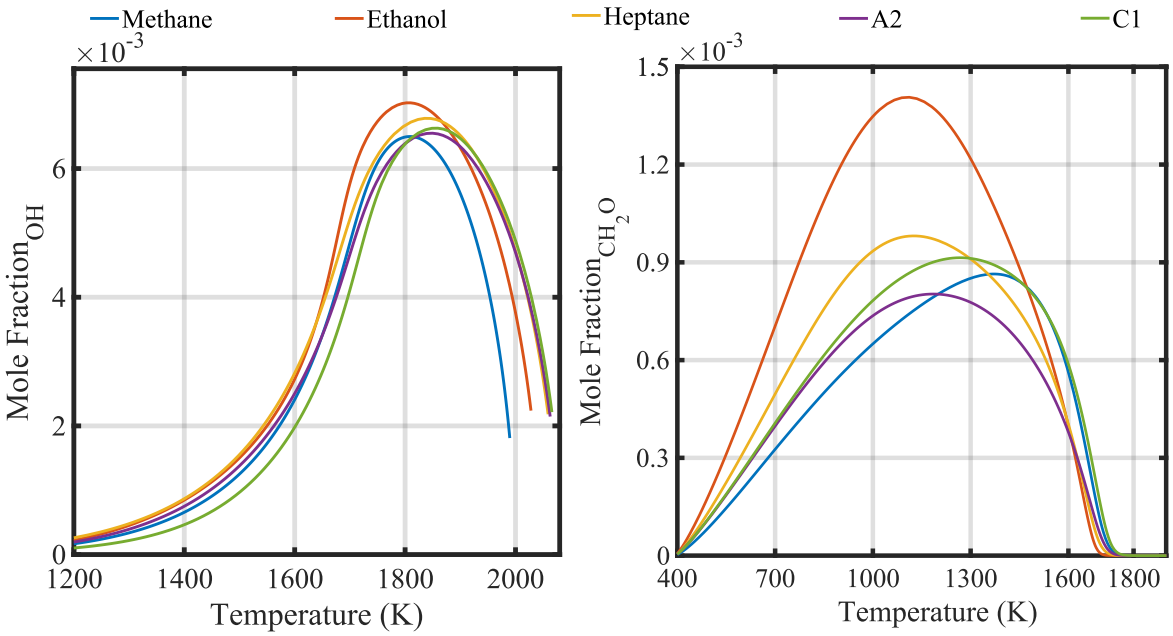

Fig. 3.3 Plot showing the mole fraction of OH and CH_2O (phi=0.75) with methane, ethanol, heptane, A2 and C1. The x-axis represents the temperature.

3.3 Structure of laminar twin flame

Counterflow twin premixed flame simulations were performed with methane, ethanol, heptane, and A2 in Cantera [121] at a range of strain rates until extinction. The same mechanisms were used here as in laminar flame simulation, and the details can be found in Table 3.1. As shown in Fig. 3.4, the premixed fuel-air mixture jets were injected from the opposite side at the same velocity. Figure 3.4 presents the profile of temperature, OH and CH_2O with A2 at strain rate = 100 s^{-1}, x-axis represents the distance between the two flames. It can be seen that CH_2O is presented in the preheat regions and OH starts to increase in the preheat regions and is present in the post-flame region. The temperature was observed to reach equilibrium between the two flames. This configuration is of particular interest, as reported in previous studies [29] that blow-off triggers in a bluff-body methane flame in the downstream regions due to flame-flame merging. A similar observation of flame-flame merging in the burner's downstream regions is reported in Chapters 5 and 6.

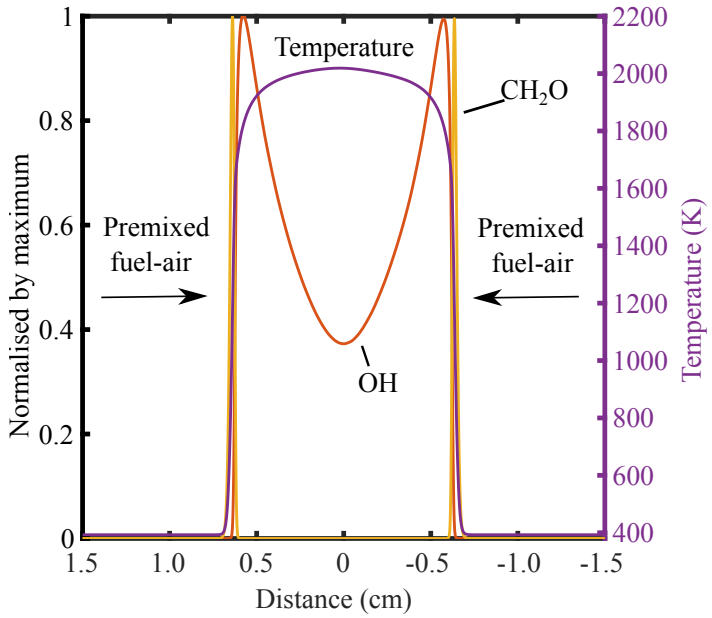

Fig. 3.4 Profile of temperature, OH, and CH_2O obtained from strained twin flame simulation with A2 at strain rate = 100 s^{-1}. The OH and CH_2O were normalised by their maximum.The total distance between the injection point is 3 cm.

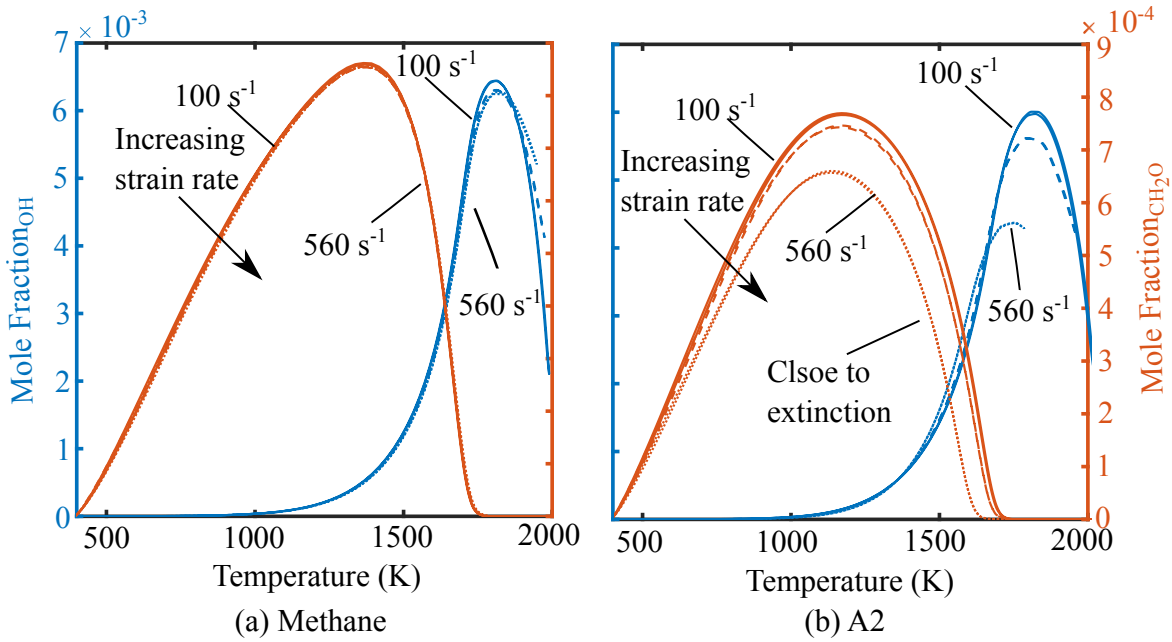

Fig. 3.5 Plot showing the mole fraction of OH and CH_2O (phi=0.75) with methane and A2 at strain rate = 100, 390, 560 s^{-1}. For A2 strain rate = 560 s^{-1} is close to extinction as the flame extinguishes above this strain rate. The x-axis represents the temperature.

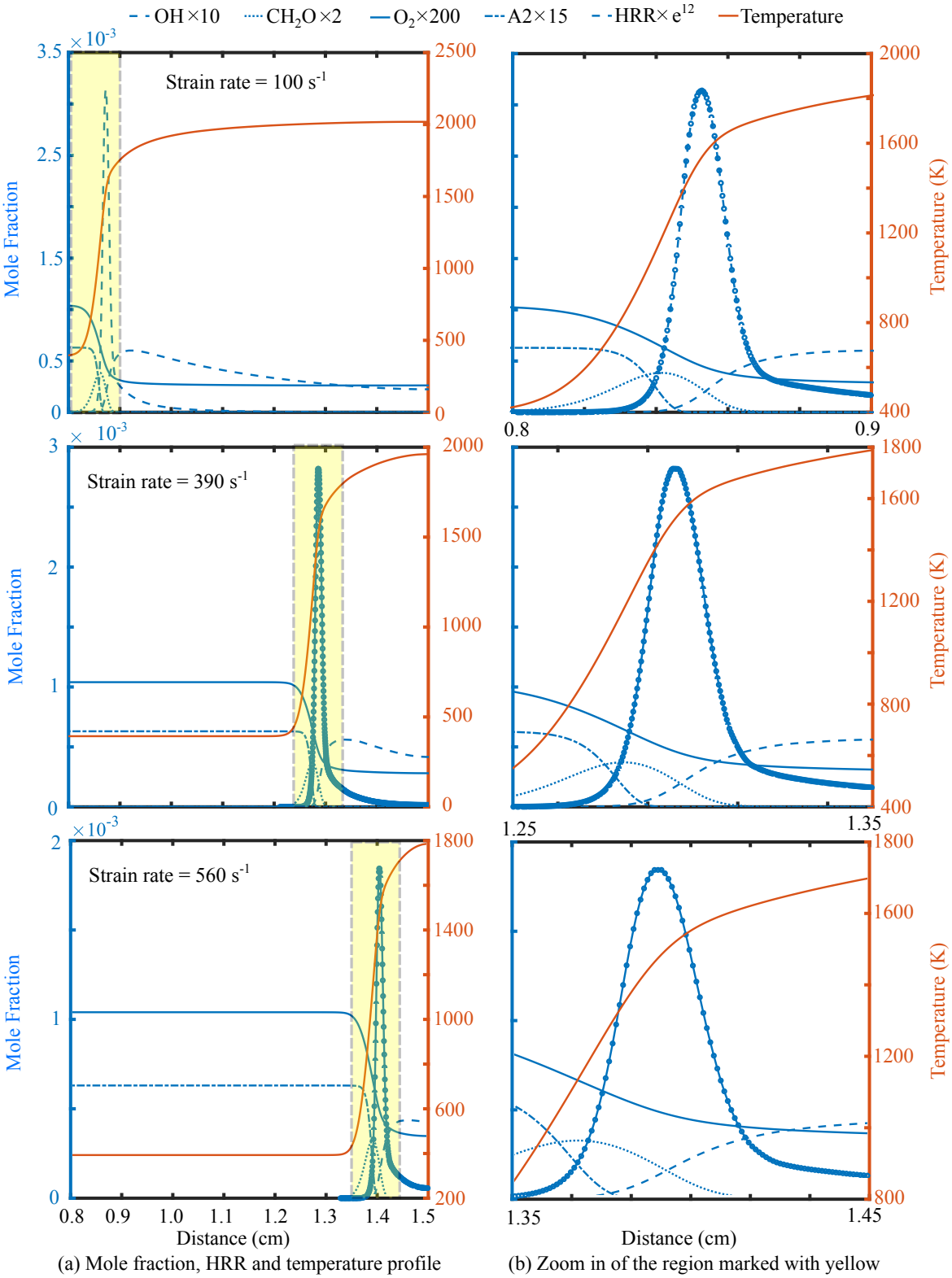

(a) Mole fraction, HRR and temperature profile (b) Zoom in of the region marked with yellow

Fig. 3.6 Plot showing the mole fraction with distance (a) Profile of OH, CH_2O, O_2, A2 (fuel), heat release rate (HRR) and temperature at ϕ=0.75 with A2. As the flame is symmetrical in nature, only left side of the flame is shown in this figure. (b) Zoom in view of the region marked with yellow color in Fig. 3.6a.

Figure 3.5 effect of strain on the mole fraction of OH and CH_2O in methane and A2 flame. Three strain rates were investigated: 100, 390, and 560 s^{-1}. The decrease in the mole fraction of OH and CH_2O was observed with an increase in strain rate. Similar trends were observed with ethanol, heptane, and C1. It was observed that the drop in peak OH and CH_2O was higher in A2 than methane at the same strain rate. It may be because of the proximity of the A2 flame close to extinction, as the A2 extinction strain (S_{lam}) at $\phi = 0.75$ is $\approx 560s^{-1}$ whereas in methane it was 5 times higher (see Fig. 4.3). Figure 3.5 shows that CH_2O peaks around 1200 K in the methane flame and kerosene peaks at around 1400 K, whereas OH is present in high-temperature regions. The similar behaviour of OH and CH_2O was observed in laminar flame simulation as reported in Section 3.2. The temperature at which peak OH and CH_2O occur does not show any dependency on strain rate.

Figure 3.6 presented the OH, CH_2O, O_2, A2 (fuel), heat release rate (HRR) and temperature at three stain rates: low (100 s^{-1}), medium (390 s^{-1}) and close to extinction (560 s^{-1}). As shown in Fig. 3.4, the flame is symmetrical. Only half of the domain is shown here. It was observed that the flame moved towards the center with an increase in strain rate, and extinction happened when the two flames from opposite sides merged. The decrease in HRR and temperature was noticed with an increase in strain rate. Figure 3.6b reports the zoom-in of the region marked with a yellow box in Figure 3.6a. Figure 3.6b shows that the OH, O_2 and A2 profile remain the same with an increase in strain rate. The broadening of the CH_2O profile was observed with an increase in strain rate. The extinction strain rate (S_{lam}) was evaluated with all five fuels at different ϕ and is presented in the next section.

3.4 Extinction strain rate in twin flame simulation

The laminar extinction strain (S_{lam}) rate was estimated with all five fuels listed in Table 3.1. The simulations were performed at blow-off equivalence ratio at different velocities shown in Fig. 4.1. The S_{lam} was estimated only from laminar twin flame simulations and not from the opposed flow flame consisting of an equilibrium product on one side and a premixed mixture on the other side. As the flame with reactant on one side and equilibrium product on the other side never extinguishes or has unrealistic S_{lam}. The laminar strain rate was defined as $\delta(v)/\delta(x)$ and extinction strain was calculated at the position of maximum strain rate ($\max(\delta(v)/\delta(x))$) as shown in Fig. 3.7. Figure 3.8 presents the extinction strain rate for all five fuels at $\phi = 0.65, 0.70, 0.75$. It can be seen that the laminar extinction strain rate increases with the equivalence ratio.

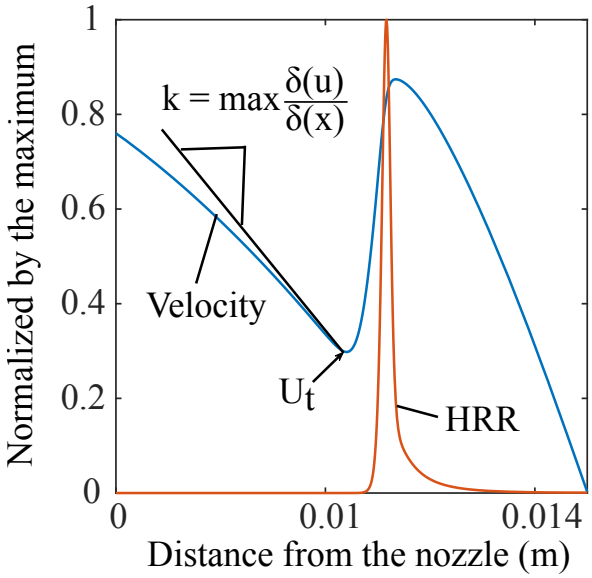

Fig. 3.7 Axial velocity and heat release rate (HRR) profile of counter flow twin flame simulation.

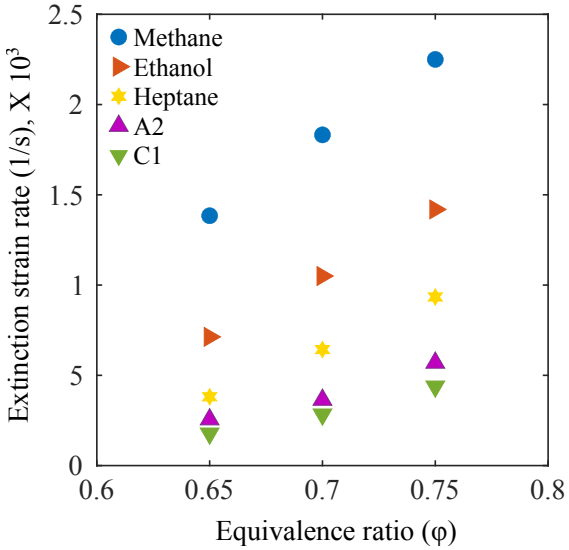

Fig. 3.8 Variation of extinction strain rate with equivalence ratio of counter flow twin flame simulation.

Kerosenes (A2 and C1) showed the lowest values of extinction strain rates than methane, ethanol, and heptane, as shown in Figure 3.8. Methane showed the highest strained laminar flame speed compared to kerosenes. As the highest values of simulated strained laminar flame speed and extinction strain rate were from methane, the results suggest that kerosenes are more prone to extinction than methane.

The purpose of performing the freely propagating laminar flame simulation was to determine the S_L. The S_L is used in the extinction correlation by Radhakrishan et al. [61] given in Eq. 2.1 and the results are presented in Chapter 4. In addition, S_L is used to normalize the local turbulent consumption speed $S_{T,LC}$. Furthermore, S_L was used to obtain the normalized turbulent intensity in Chapter 6 and plot the flames in this work on a theoretical regime diagram [135].

In section 6.5, the laminar flame thickness is used to normalize the experimentally obtained curvature of the turbulent premixed flame. The extinction strain is used in the correlation proposed by Shanbhogue et al. [23] in Chapter 4.

3.5 Summary

The results of unstrained and strained laminar flame simulations are presented in this chapter. Detailed mechanisms and transport properties were applied to methane, ethanol, heptane, and two kerosene (A2 and C1). Laminar flame speeds were obtained at various equivalence ratios. The flame structure of the laminar flame was discussed. It was observed that OH forms in a high-temperature region and is also present in the post-reaction zone. CH_2O is formed at low temperatures and consumed at high temperatures in premixed flames. For all five fuels, the extinction strain rate was calculated at different equivalence ratios. It was observed that kerosene is more prone to extinction in a twin premixed flame configuration than in a methane flame. The extinction strain rates for ethanol and heptane are between those of kerosene and methane.

Chapter 4

Lean blow-off limits and scaling

This chapter discusses the lean blow-off limits with ethanol, heptane, and two kerosene (A2 and C1) fuels and compares the results with methane flame[1]. The LBO limits are presented in Section 4.1 and to facilitate comparisons with gaseous flames, results were also obtained from methane flames. The results were evaluated based on a *Da* correlation based on laminar flame speed proposed by Radhakrishnan et al. [61]. The extinction strain rate obtained from the twin strained flame simulation is used to investigate the role of extinction and *Le* in governing the LBO.

[1] Some of the results of this Chapter have been published in: Rohit S. Pathania, Aaron W. Skiba, Jenni A. M. Sidey-Gibbons, Epaminondas Mastorakos, Lean blow-off scaling of turbulent premixed bluff-body flames of vapourised liquid fuels. *Journal of Propulsion and Power*, 2020.

4.1 Lean blow-off limits

Figure 4.1 shows the LBO curve for the kerosene (A2 and C1) and single-component fuels (methane, ethanol, and heptane). Based on the procedures described in Section 2.2.1, each experiment was performed 20 times. As observed in prior studies (e.g., Refs. [29, 28, 62]), the equivalence ratio at which the flames blow-off increases with higher U_b. Figure 4.1 indicates that the kerosene fuels are less stable than ethanol and heptane, with C1 flames being the least stable. As Fig. 4.1 shows, methane flames are found to be the most resilient, while the stability curves for ethanol and heptane fall between those for the methane- and the kerosene flames. Additionally, for the two kerosene flames, it was observed that the one with a higher DCN (A2 in this case) was more stable, which is consistent with the findings in Ref. [63].

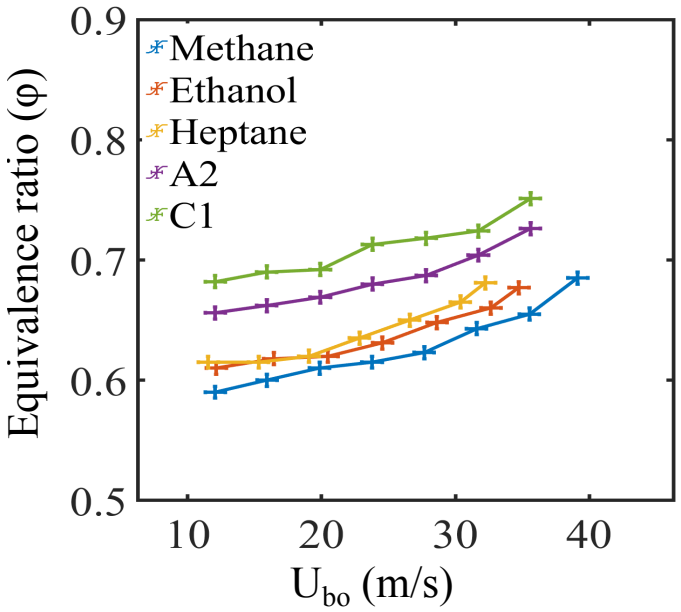

Fig. 4.1 Plots showing the LBO Limits (ϕ_{bo}) as a function of LBO velocity (U_{bo}). The each point on LBO curve represents the average of 20 measurements. The error bars (cross-marks) represents the uncertainty in experiments in velocity and equivalence ratio.

4.2 Lean blow-off scaling

For each of the LBO points, the corresponding laminar flame speed was estimated, and the LBO limits were evaluated with the correlation of Radhakrishnan et al. [61] derived in the context of turbulent premixed flames given in Eq. 2.1. Also, the correlation is applied to the methane flame LBO data measured by Kariuki et al. [29, 28]. Figure 4.2a shows these results. The slope of the curve in Fig. 4.2a is represented by Da_{bo}^{-2} (see Eq. 2.1) .

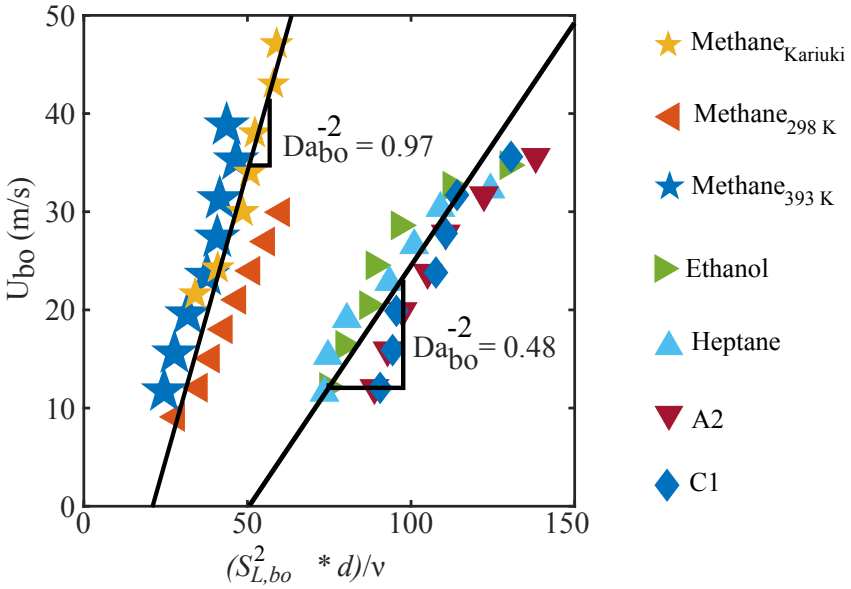

(a) Value of Da^{-2}_{bo} based on correlation of Radhakrishnan et al. [5].

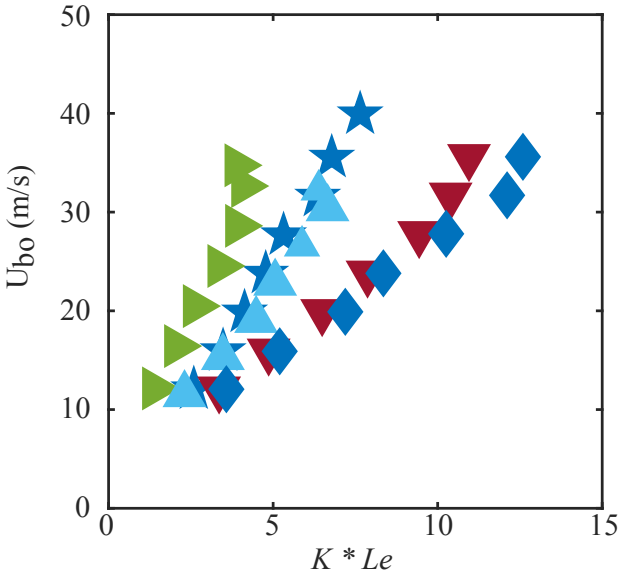

(b) Value of $K * Le$ based on Abdel-Gayed and Bradley's correlation [83, 84].

Fig. 4.2 Plots showing the Da_{bo}^{-2} and $K \times Le$ as a function of blow-off velocity (U_{bo}) for single-component and multi-component fuels.

The intercepts in Fig. 4.2a point out that they are non-physical merely because of the correlation in Eq. 2.1 does not apply to flames in laminar limits. The value of $1/Da$ varies between 0.82 and 0.88 for methane flames at the blow-off velocities considered here. In the

case of vaporised liquid fuels, this variation is from 0.38 to 0.52. The variation in the $1/Da$ values is not significant. Shanbhogue et al. [23] and Kariuki [28] reported a similar variation of $1/Da$, where this scaling was found to hold for methane flames. The solid black lines in Fig. 4.2a represent these Da values. It was observed that Da_{bo}^{-2} values collapse reasonably well for the separate liquid fuels and is ≈ 0.48 over the range of bulk velocities considered here. In contrast, the methane flames are found to have Da_{bo}^{-2} values of ≈ 0.97, which is consistent with the results of Kariuki et al. [28].

Since the vapourised liquid hydrocarbon fueled flames were operated at an elevated temperature (to ensure complete vaporisation), a series of stability tests were performed with methane at both ambient and elevated temperatures (298 K and 393 K, respectively), and the S_L was computed at the respective temperature. These results are also presented in Fig. 4.2a, which shows that an increased reactant temperature has little to no effect on the stability of the methane flames. Thus, the difference in stability between methane and the other fuels is not a consequence of the latter being preheated before combustion.

Shanbhogue et al. [23] and Radhakrishnan et al. [61] showed that for a particular bluff-body type (2-D vs axisymmetric), the LBO limits collapse around a single value of Da regardless of the gaseous fuel used. Since the methane and liquid fuel flames considered here do not collapse to a single value of Da, this correlation is not sufficient for predicting the LBO limit of heavier hydrocarbon fuels. Within this Da-based scaling correlation, aspects of the combustion chemistry are subsumed into one parameter: S_L. Yet, this correlation's inability to yield a proper collapse of the data suggests that S_L does not adequately capture the relevant combustion phenomena when complex hydrocarbon fuels are considered. Notably, this is supported by the fact that A2 and methane flames tend to have similar values of S_L (see Table 2.2), yet such flames possess drastically different LBO limits. Furthermore, the failure of simple S_L-based scaling laws to track observed results for complex hydrocarbon fueled flames was also reported in Ref. [38]. Hence, parameters beyond S_L are likely necessary to encapsulate the combustion chemistry associated with complex hydrocarbon-fueled flames fully.

Previous studies emphasized the role of extinction and Le in governing LBO [40, 38, 31]. Abdel-Gayed and Bradley [136] proposed a correlation based on the turbulent Karlovitz stretch factor (K) and Le. They reported that the flame quenches if $K \times Le > 1.5$. Here, K was estimated at LBO based on the assumptions used in Ref. [32]. They assumed that the average turbulent intensity is $u'/U_{bo} = 0.2$ (u' is the RMS of the velocity fluctuations), and that turbulent length scale (L) can be approximated by $d/5$. With this crude analysis, K is defined as $K = \delta u'(S_L \lambda_T)^{-1}$ and can be rewritten as $0.125(u'/S_L)^2(Re_t)^{-1/2}$ [137], where Re_t is the turbulent Reynolds number and δ_l is the laminar flame thickness. The variation

in Re_t is from 430 to 1450 for different velocity conditions. Based on these assumptions, K lies in the range of 1.08 - 2.30 for the different flames studied here, while their Le span from 0.98 to 5.0 (see Table 2.2). Figure 4.2b shows the value of $K \times Le$ at the LBO velocity for all five fuels. The estimated K numbers in the current study are higher than those ascribed to the limit above, which spherically expanding turbulent premixed flames cannot be sustained [136, 137]. Thus, based on Abdel-Gayed and Bradley's correlation, the extinction K for methane is ≈ 1.5 while that for A2 is ≈ 0.32. This implies that heavier hydrocarbon-fueled flames are more susceptible to extinction than methane, which may explain why kerosene flames blow-off at higher equivalence ratios than those produced with methane. Namely, the above analysis based on Abdel-Gayed and Bradley's results suggests that the Le of the fuel influences its propensity for extinction. In past studies, which primarily considered simple gaseous fuels, Le effects were negligible because the fuels had $Le \approx 1$. Moreover, Law [138] showed that flames with $Le > 1$ (e.g., heptane, A2, and C1) could experience extinction solely because of sufficient straining; however, flames with $Le \leq 1$ require incomplete combustion, heat loss, or high rates of curvature for extinction to occur. It is apparent from Fig. 4.1 and Table 2.2 that the LBO equivalence ratio increases with Le. Therefore, it can be assumed that vaporized liquid fuels with $Le > 1$ experience a higher degree of localized extinction, which causes these flames to blow-off at higher equivalence ratios than methane flames.

Twin counterflow strained laminar premixed flame simulations were performed to obtain the laminar extinction strain rates, S_{lam}, at the blow-off equivalence ratio for all five fuels. Shanbhogue et al. [23] suggested that the chemical time scale based on extinction strain rate may provide a better grouping of the data. Thus, the extinction strain rate was estimated at the blow-off equivalence ratio at each velocity condition for all fuels considered in the current study. Figure 4.3 shows the laminar extinction strain rate from the simulation as a function of the bulk velocity. Methane exhibits the highest value of extinction strain rate. Heptane and the two kerosenes (A2 and C1) possess nearly the same extinction strain rate, and ethanol has an extinction strain rate between those of methane and heptane and the kerosenes. The data in Fig. 4.3 demonstrate that the separate fuels considered here result in different values of $(d/U_{bo})/S_{lam}$, and hence the laminar flame extinction strain rate does not collapse well the blow-off condition of different fuels.

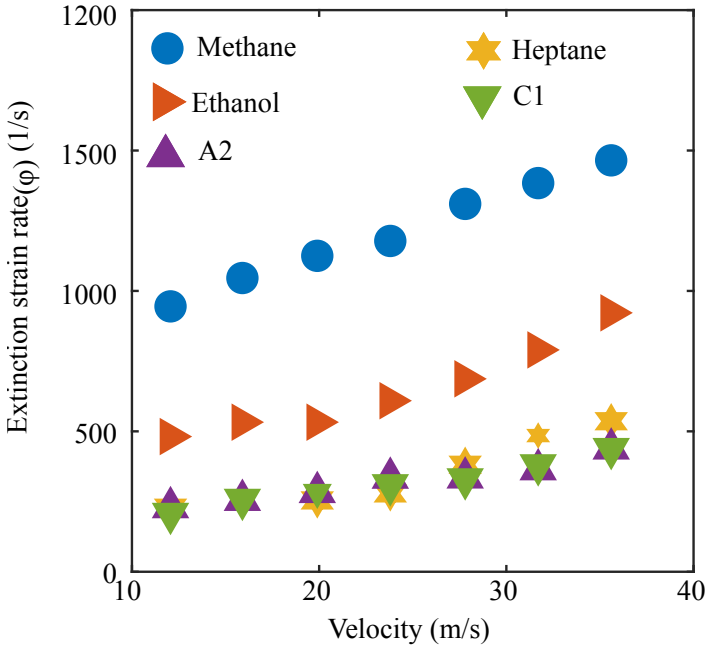

Fig. 4.3 Variation of simulated extinction strain rate from the twin flame simulation as the function of equivalence ratio with U_{bo}.

The analysis above attempts to correlate the onset of blow-off with terms like S_L, $K \times Le$, or S_{lam}; however, such efforts have failed to fully collapse the LBO data across the range of fuels studied here. This implies that the extrapolation of knowledge from flames of small hydrocarbons (e.g., methane, ethylene) to higher hydrocarbons (e.g., heptane, kerosenes) cannot simply be based on concepts where all the combustion chemistry is expressed through S_L, even after considering Le or strain effects.

4.3 Summary

The effect of fuel properties on the blow-off limits and flame shape were investigated for vapourised ethanol, heptane, and two separate kerosene fuels (A2 and C1) in a bluff-body burner. It was observed that the methane, ethanol, and heptane flames are more resilient to blow-off than the kerosene flames (i.e., A2 and C1). Also, the stability limits were evaluated using a correlation based on a characteristic Damköhler number (Da). The correlation was not successful in collapsing the liquid-fueled flames to the line derived from methane flames. This suggests that correlations wherein the combustion chemistry is solely subsumed within the laminar flame speed (i.e. that based on a characteristic Da) are not likely to be universally applicable. Ultimately, the results of this effort highlight the influence fuel-type has on the LBO of bluff-body stabilized flames. Moreover, this work indicates the LBO

behavior of flames produced with complex hydrocarbon fuels can not be fully understood by high-temperature chemistry concepts such as laminar flame speed.

Chapter 5

Blow-off duration and mechanism

Previously, we discussed the blow-off limits of different fuels, and found that kerosene is less resistant to blow-off than methane. Yet the blow-off mechanism was not explained in detail in that chapter. In this chapter, the blow-off mechanism, and blow-off duration[1] is discussed. Firstly, the flame structure is visualized with OH* imaging during blow-off. Those OH*-images are then used to calculate the blow-off duration. Different diagnostic techniques are used in the rest of the chapter to show species distribution inside the RZ during blow-off. In this study, only the A2 flame was studied because the A2 is the most complex fuel. OH-PLIF, CH_2O-PLIF, and Fuel-PLIF were used during blow-off. For the conclusions presented in this chapter, 10 blow-off events were recorded with each diagnostic technique. Lastly, imaging results are contrasted against those obtained from methane and ethylene flames in previous works [32, 29, 36, 17], highlighting differences in the structure of flames near LBO.

[1] Results of this Chapter have been published in: Rohit S. Pathania, Aaron W. Skiba, Roberto Ciardiello, Epaminondas Mastorakos, Blow-off mechanisms of turbulent premixed bluff-body stabilized flames operated with vapourised kerosene fuels. *Proceedings of the Combustion Institute*, 2020.

5.1 Blow-off duration

Figure 5.1a shows a temporal sequence of OH* chemiluminescence images with the A2-fuelled flame during a LBO event. During its approach to LBO, the flame became progressively shorter and survived for tens of milliseconds within the RZ. Additionally, the OH* chemiluminescence signal was confined to the RZ during the LBO event. Such images were used to evaluate the duration of the LBO event for all fuels. Namely, the OH* signal was integrated over the imaged area and plotted *vs.* time. The onset of the blow-off event was associated with a decrease in the OH* signal, which appears to be linked to flame shortening and fragmentation, as shown in Fig. 5.1a. The same procedure was followed by Dawson et al. [32] with methane flames, where the blow-off duration was found to be on the order of $15d/U_{BO}$, where U_{BO} was the bulk velocity at blow-off.

Figure 5.1b shows the average of five spatially integrated OH* signals during blow-off. The extinction duration, τ_{ext}, was quantified as the time it took the OH* signal to decay from 50 % to 5 % of the time-averaged level before LBO (the OH* signal never grows back if the signal drops lower than 50%). The results are presented in Table 5.1. Since the blow-off event was not directly controlled, the original OH* time series were shifted to coincide with the disappearance of OH* signal. The value of τ_{ext} depends on the threshold value used. However, choosing different thresholds did not affect the trends between τ_{ext} and fuel type. In the current study, τ_{ext} was $\approx$ 22 and 24 for methane and ethanol, respectively. Whereas, for heptane, A2, and C1 it was 64.60 ms, 63.20 ms, and 54.60 ms, respectively (around $60d/U_{BO}$).

This suggests that blow-off is more sudden in the methane and ethanol flames as compared to those operated with heavier hydrocarbons. It may be possible that during the LBO transient, the RZ contains fluid (discussed later through the PLIF images) spanning the whole range of possible values of the progress variable (i.e., fresh reactants, partially-burnt reactants, and fully-burnt products). Thus, some low-temperature chemistry that would be more pronounced in the large hydrocarbons compared to CH_4 and C_2H_5OH, may be present, which leads to a continuous re-ignition of flame fragments in the RZ hence prolonging the complete LBO event [63].

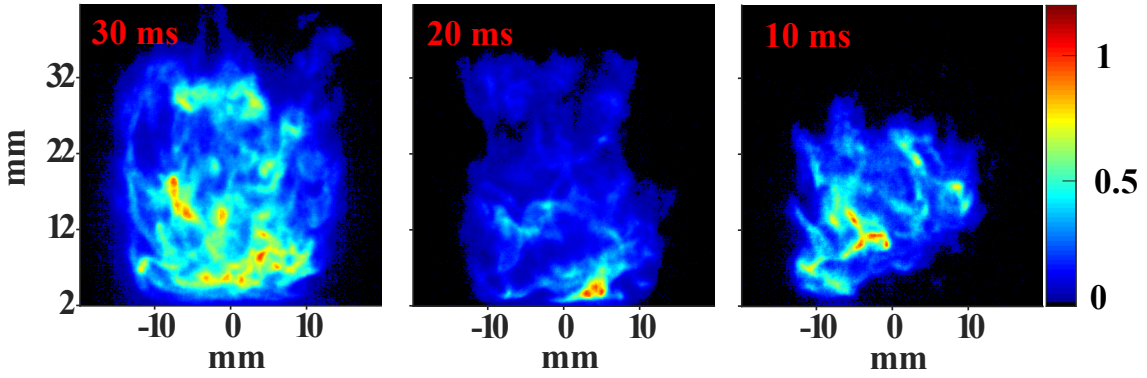

(a) OH* chemiluminescence images during LBO for A2. The time on each image (30 ms, 20 ms, and 10 ms) represents the OH* chemiluminescence structure at those instances before blow-off.

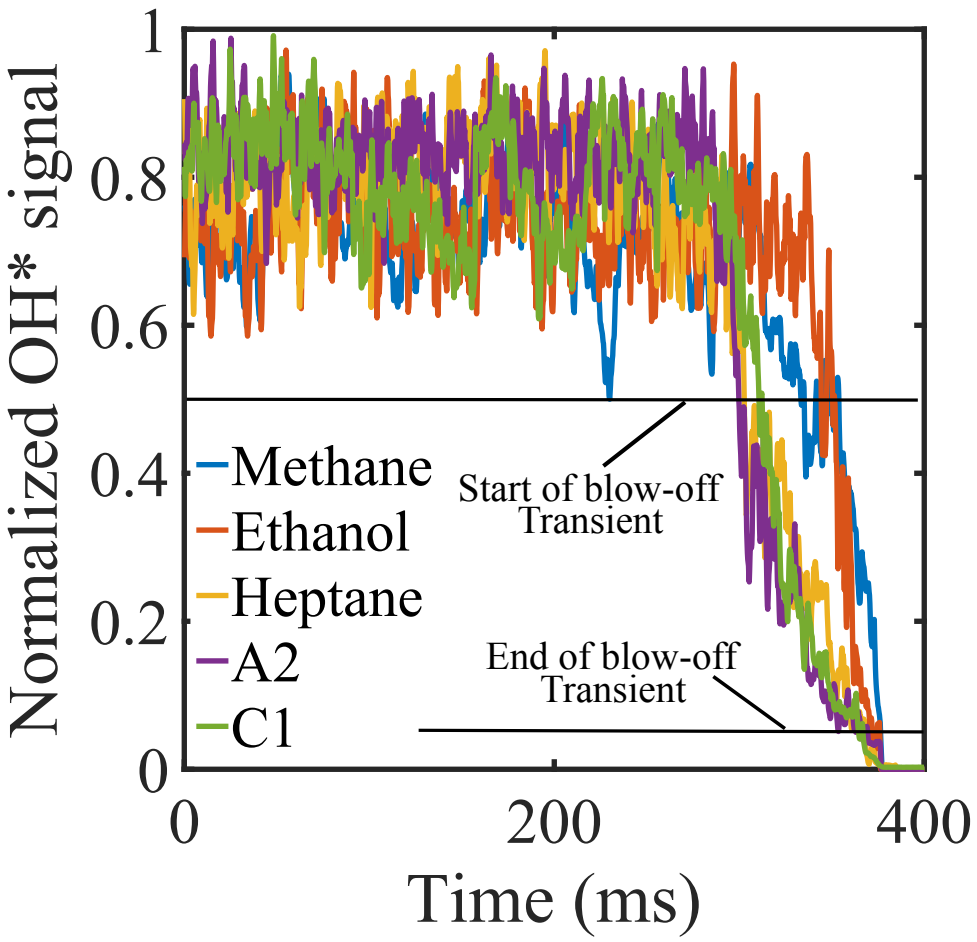

(b) Area-integrated OH* *vs.* time for all fuels.

Fig. 5.1 (a) OH* chemiluminescence Images of the LBO transient with A2 and (b) integrated OH* for methane, ethanol, heptane, A2 and C1. In (b), the data presented is the average of five LBO events.

Table 5.1 Values of τ_{ext} evaluated for different fuels for $U_b = 23.5 \pm 1.5$ m/s.

Fuel	$U_{BO}(m/s)$	ϕ	Le	τ_{ext} (ms)	τ_{ext}/(d/U_{bo})
Methane	24.8	0.615	0.98	22.70	23.50
Ethanol	24.5	0.63	1.68	24.40	26.00
Heptane	22.8	0.635	2.8	64.60	64.03
A2	23.8	0.68	4.6	63.20	65.40
C1	23.8	0.71	5.0	54.60	56.50

5.2 Species distributions during LBO

In this Section, the qualitative distributions of OH, Fuel, and CH_2O at various instants during LBO are described. Only images from A2 flames are considered as such flames permit fuel-PLIF imaging, and prior studies of methane flames have presented PLIF images of OH, and CH_2O [36] in this burner. Also, A2 is interesting as it is the most chemically complex fuel considered here. In interpreting the results, it might be convenient to consider that Fuel-PLIF represents low values of the progress variable; CH_2O comes from intermediate values, and OH comes from fluid particles with high progress variable values [97].

Figure 5.2 presents instantaneous OH-PLIF images before the blow-off event of an A2 flame, and the corresponding video can be accessed through the link provided in Appendix A. A substantial change in the flame structure was observed as LBO was approached with an overall OH signal decrease. The OH regions become distorted inside the RZ, and pockets filled with and void of OH were observed simultaneously. The flame becomes shorter with the peak OH-PLIF signal lying within the RZ above the bluff-body.

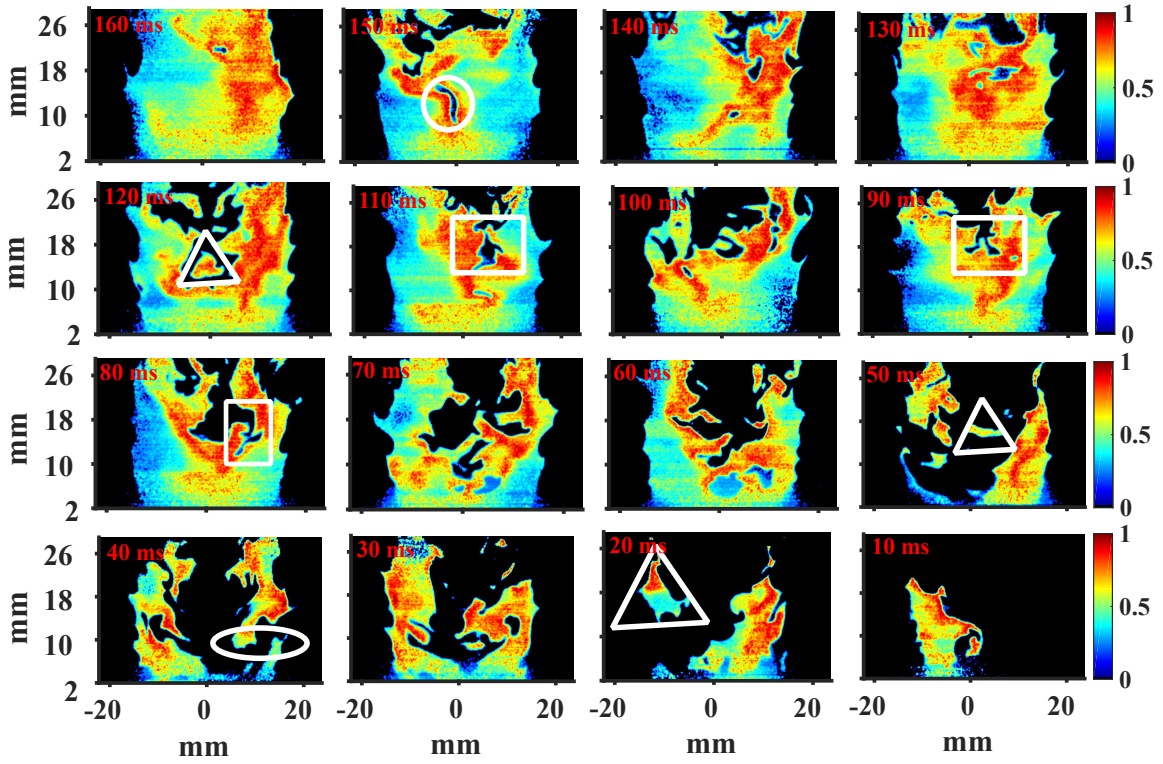

Fig. 5.2 OH-PLIF sequence during a blow-off event for A2-fuelled flame at $U_b = 23 \pm 1.5$ m/s.

Specifically, as LBO was approached, four dominant events were observed: (i) appearance of finger-like structures (marked with rectangles); (ii) formation of regions void of OH (marked with circles); (iii) breaks along the flame-front near the shear layer (marked with a white ellipse); and (iv) formation of pockets of OH-PLIF signal in the RZ (marked with triangles). The finger-like structures were noticed to enter into the RZ from its downstream end. Similar findings on the formation of finger-like structures (long ligaments void of OH) were reported in experimental studies with propane, ethylene, and methane [29, 17]. In our experiments, these structures were observed to enter from downstream and penetrate deep into the RZ and reach close to the bluff-body, as shown in the OH-PLIF video that can be accessed through the link provided in Appendix A. These voids burned out as they moved towards the bluff-body. In addition, it was found that sometimes the regions void of OH-PLIF travel towards the flame-front at the shear layer, causing what appears to be local extinction, which leads to further regions void of OH that are eventually convected into the RZ. The absence of OH in a specific region (e.g. lowest and left-most panel of Fig. 5.2) can only correspond to either extinction or the presence of reactants (fresh or with intermediate

species like CH_2O). The inclusion of CH_2O- and Fuel-PLIF imaging facilitates to distinguish between these two options.

Figure 5.3 shows sequences of CH_2O-PLIF images from methane and A2 flames during a blow-off event. Since the CH_2O-PLIF images were taken at 10 Hz, the error in determining the blow-off instant is $\sim$100 ms. However, comparison between the fuels is still instructive. It can be seen that CH_2O enters the RZ from the downstream region. Both fuels exhibit thin layer-like preheat zones in the anchoring region and in the shear layer up to a distance of $\sim$1 d from the bluff body. Further downstream, the CH_2O layers begin to broaden. Such broadening is limited to 2-3 mm in the methane flames, and the CH_2O occupies layer-like regions. In contrast, CH_2O layers in the A2 flame become so broad (i.e., $\sim$1 d thick) in the downstream region that they no longer exhibit layer-like features.

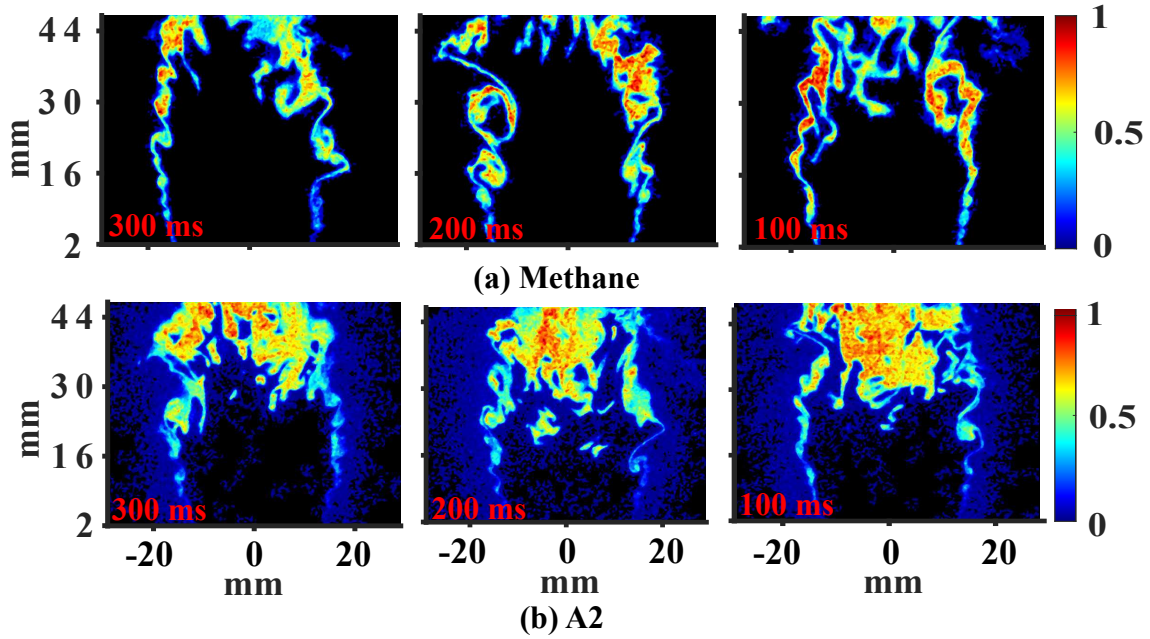

Fig. 5.3 CH_2O-PLIF sequences during a blow-off event for methane and A2-fuelled flames at $U_b = 23 \pm 1.5$ m/s. The images were taken at an frequency of 10 Hz.

The individual pockets of CH_2O-LIF signal inside the RZ confirm that the voids present in the OH-PLIF images (marked with circles on the OH-PLIF images, Fig. 5.2) likely consist of CH_2O. Furthermore, it can be seen from Fig. 5.3 that the CH_2O encapsulates the RZ through the merging of layers from opposite sides of the burner in the downstream region (size of the RZ can be around 1.5 to 2 the bluff-body diameter [29]), confirming that blow-off is associated with the merging of the flame branches from either side of the bluff body in this burner. Moreover, oxidation of heavy hydrocarbon fuels starts at low/intermediate

temperature (600 - 900 K) [139]. Thus, the presence of broad regions of CH_2O inside the RZ in A2 flame implies the dominance of low-temperature oxidation reactions.

Figure 5.4 shows Fuel-PLIF images from an A2 flame (a video of blow-off event with Fuel-PLIF can be accessed through the link provided in Appendix A). Prior to LBO, the fuel is confined to the annular jet, which appears continuous and uniform. The absence of breaking and reduction in intensity in the Fuel-PLIF signal suggests there is little entrainment of ambient air. Approximately 50 ms before LBO, pockets of Fuel-LIF signal were observed in the RZ and even near the bluff-body (see Fig. 5.4). The entry of fuel into the RZ can be correlated to the breaking in the flame-front, as shown in the OH-PLIF image at 50 ms (Fig. 5.2). Finally, at LBO, the RZ is filled with fresh reactants.

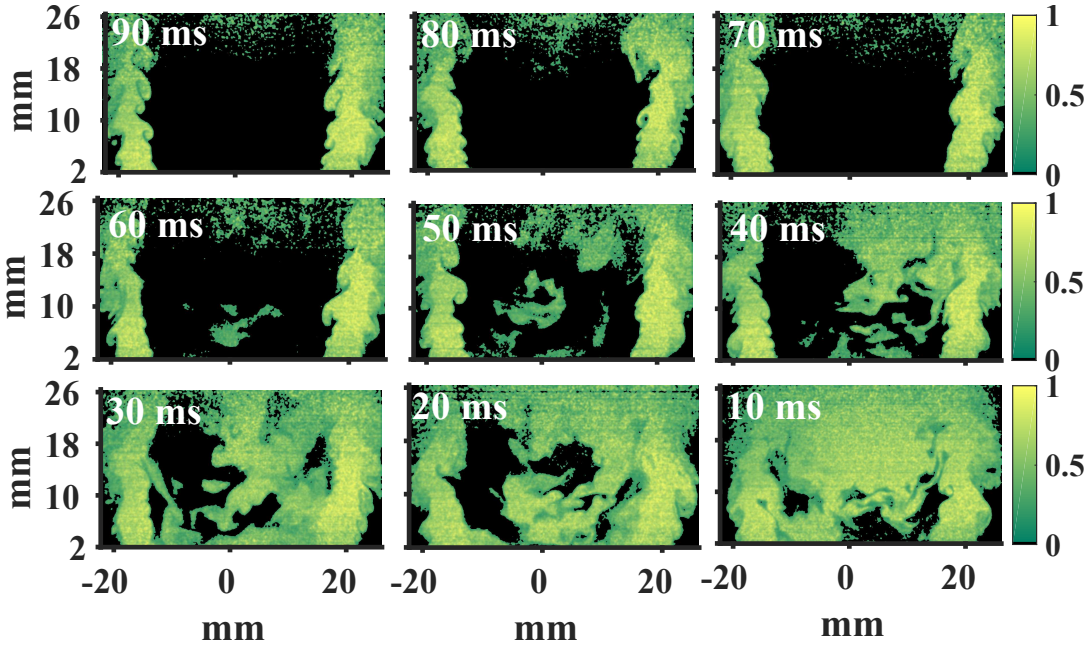

Fig. 5.4 Sequence of Fuel-PLIF images during a blow-off event for the A2-fuelled flame, at $U_b = 23 \pm 1.5$ m/s.

The OH-PLIF images were further analysed to estimate the number of OH-pockets that form during LBO. Figure 5.2 shows the RZ filled with OH, but as the flame approaches blow-off, the initially continuous OH region in the RZ shreds into many small pockets. Figure 5.5a shows the average (based on 10 blow-off events) number of OH-LIF pockets from the A2 and methane flames as they approached blow-off. To identify individual pockets, the OH-PLIF images were binarized based on their 10 % contour. Then the total number of individual islands of OH were counted in each instantaneous image. It can be observed that in both flames, there was a sudden rise in the number of OH pockets roughly 20 ms before

complete extinction, consistent with the insights obtained from the time sequence in Fig. 5.2 that the OH-containing region disintegrates before LBO.

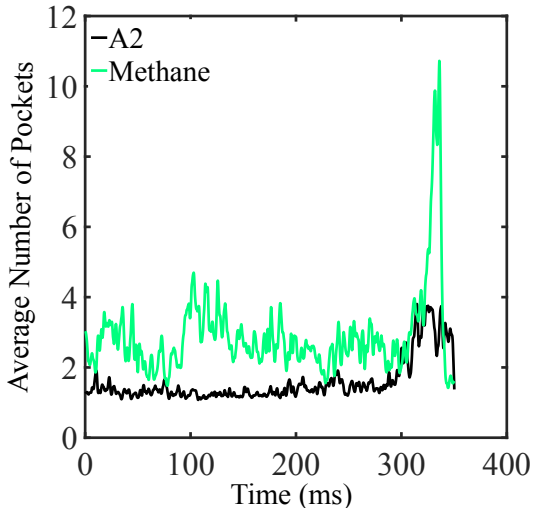

(a) Average number of pockets of OH-LIF signal.

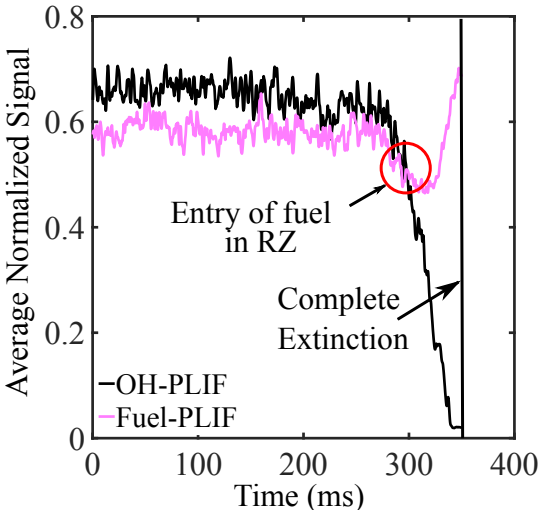

(b) Average OH- and Fuel-PLIF signal.

Fig. 5.5 Plot showing the time average of 10 blow-off events. (a) Variation of number of OH-LIF signal pockets as the blow-off was approached for methane and A2. (b) Variation of OH- and Fuel-PLIF signal with A2 as the blow-off was approached.

Figure 5.5b shows the area-integrated OH-PLIF and Fuel-PLIF (averaged over 10 LBO movies) from the A2 flame. The juxtaposition of these two-time series shows, on average, the relative instant at which fuel enters the RZ compared to the time the OH disappears. After a short transient, the Fuel-PLIF signal started increasing as the OH-PLIF signal kept decreasing. Based on these averages, the critical time at which the fuel begins entering the RZ was $\sim$45 ms before complete extinction.

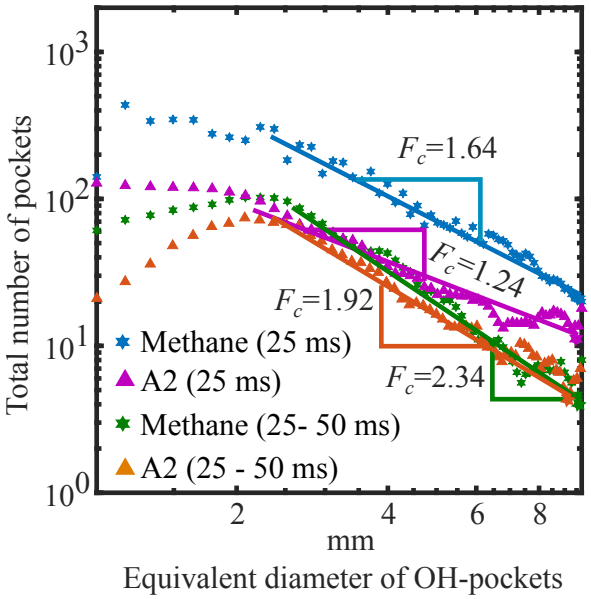

Fig. 5.6 Number of OH pockets *vs.* their equivalent diameter averaged over 10 blow-off events. The degree of fragmentation (F_c) is represented by the slope of the curves. Two set of images were analysed, 50 - 25 ms before LBO and 25 ms to LBO.

A further analysis was performed on the OH-PLIF images to quantify the fragmentation of the flames (F_c). The data was separately analysed for the period 25 ms before LBO to the moment of LBO and for the period 25 - 50 ms before LBO. The OH-PLIF images were converted into black-white images using 20 % contours to perform the fractal analysis. From the binarized instantaneous images, the area of individual pockets was calculated. Then the equivalent diameter of each area was evaluated. Each diameter's pockets were binned together from separate images and plotted on a log plot with the x-axis as the diameter of the pockets, and the y-axis corresponds to the number of pockets. A linear regression fitting was performed on the data, and the slope of the curve gives the F_c as shown in Fig. 5.6. It was observed that the methane flame experienced higher F_c than A2. These findings are consistent with the results presented in Fig. 5.5a. Moreover, F_c increases as LBO is approached, which may be due to the extinction of the small pockets of OH-PLIF as the flame approaches complete LBO (see Fig. 5.2).

5.3 Summary

The lean blow-off (LBO) behavior of unconfined lean premixed bluff-body stabilized flames with various fuels was investigated. Methane and vapourised ethanol, heptane, Jet-A1, and alternative alcohol-derived kerosene (Gevo) were used. OH* chemiluminescence (5 kHz),

OH- and Fuel-PLIF (5 kHz), and CH_2O-PLIF (10 Hz) were deployed. For all fuels, as the flame approached, LBO fragmentation was observed downstream. The two sides of the flame merged at the axis, pockets of OH and CH_2O were found in the recirculation zone (RZ), and eventually, the individual fragments were extinguished. The CH_2O seemed to enter into the RZ from downstream early in the LBO process, with reactants the following suit at times closer to LBO. During LBO, the integrated OH* signal decreased slowly to zero. The duration of this transition was $\sim$25 (d/U_{BO}) in the methane and ethanol flames and $\sim$60 (d/U_{BO}) in flames operated with heptane and the two kerosenes (where d is the bluff-body diameter and U_{BO} the LBO velocity). This large difference could be due to the re-ignitions of partially-quenched fluid inside the RZ during the LBO event. Additionally, for the same bulk velocity, the kerosene flames blow-off at higher equivalence ratios than the single-component fuelled flames, possibly due to the higher Lewis number and lower extinction strain rates of these fuels. The results suggest that the blow-off mechanism is qualitatively similar for each of the fuels; however, the complex chemistry associated with heavy hydrocarbons appears to result in a prolonged LBO event.

Chapter 6

Spatial flame structure

The LBO mechanism previously described showed that the blow-off duration of kerosene flames is longer than that of methane and ethanol. During blow-off in a kerosene flame, we observed broad regions of CH_2O within the RZ. As blow-off is an uncontrolled event, it is difficult to obtain statically quantities such as FSD and the thickness of CH_2O layers. For this reason, this chapter presents the flame structure at two conditions: far from blow-off ($\phi/\phi_{BO} = 1.20$)) and close to blow-off ($\phi/\phi_{BO} = 1.01$). The detailed flame structure was investigated with 5 kHz OH* chemiluminescence, OH-PLIF imaging, and 10 Hz CH_2O-PLIF imaging[1]. The details of optical setups are provided in Chapter 2. Four different fuels were considered, two of which comprised of a single component (ethanol and heptane), while the other two were multi-component kerosene blends (A2 and C1). The Chapter is organized as follows: i) Instantaneous and averaged OH*chemiluminescence images are presented with all four fuels. The results are compared with previous studies, then Abel transformed images are presented. ii) OH-PLIF flames are reported, and the effect of turbulent intensity on the flame structure is discussed. From the OH-PLIF images, average reaction progress, variable images were calculated and discussed. These images were used to evaluate the flame surface density (FSD) at far from and close to blow-off conditions. Additionally, they were used to compute the 2-D curvature of the flame. The local estimate of the average consumption speed was also reported in this Chapter. iii) The effect of turbulent intensity on the CH_2O-layer thickness. The CH_2O-thickness is calculated from CH_2O images, and the results are complied into PDF.

Lastly, the non-reacting and reacting flow velocity data is presented in non-reacting and vapourised heptane flames under stable and near blow-off conditions. Additionally, turbulent

[1] Some of the results of this Chapter have been published in: Rohit S. Pathania, Aaron W. Skiba, Epaminondas Mastorakos, Experimental investigation of unconfined turbulent premixed bluff-body stabilized flames operated with vapourised liquid fuels. *Combustion and Flame*, 2021.

intensity and turbulent length scale L_T are evaluated at different locations from the burner exit. The local Ka and Da are calculated. The details of the procedures used to compute L_T and Ka are provided in Sec. 6.10.

6.1 Flame shape

High-speed OH* chemiluminescence was used to characterize the flame shape. OH* can be used to roughly indicate the location of key chemical reactions within premixed flames [113, 140]. The average flame shape was obtained by averaging 5400 instantaneous OH* chemiluminescence images.

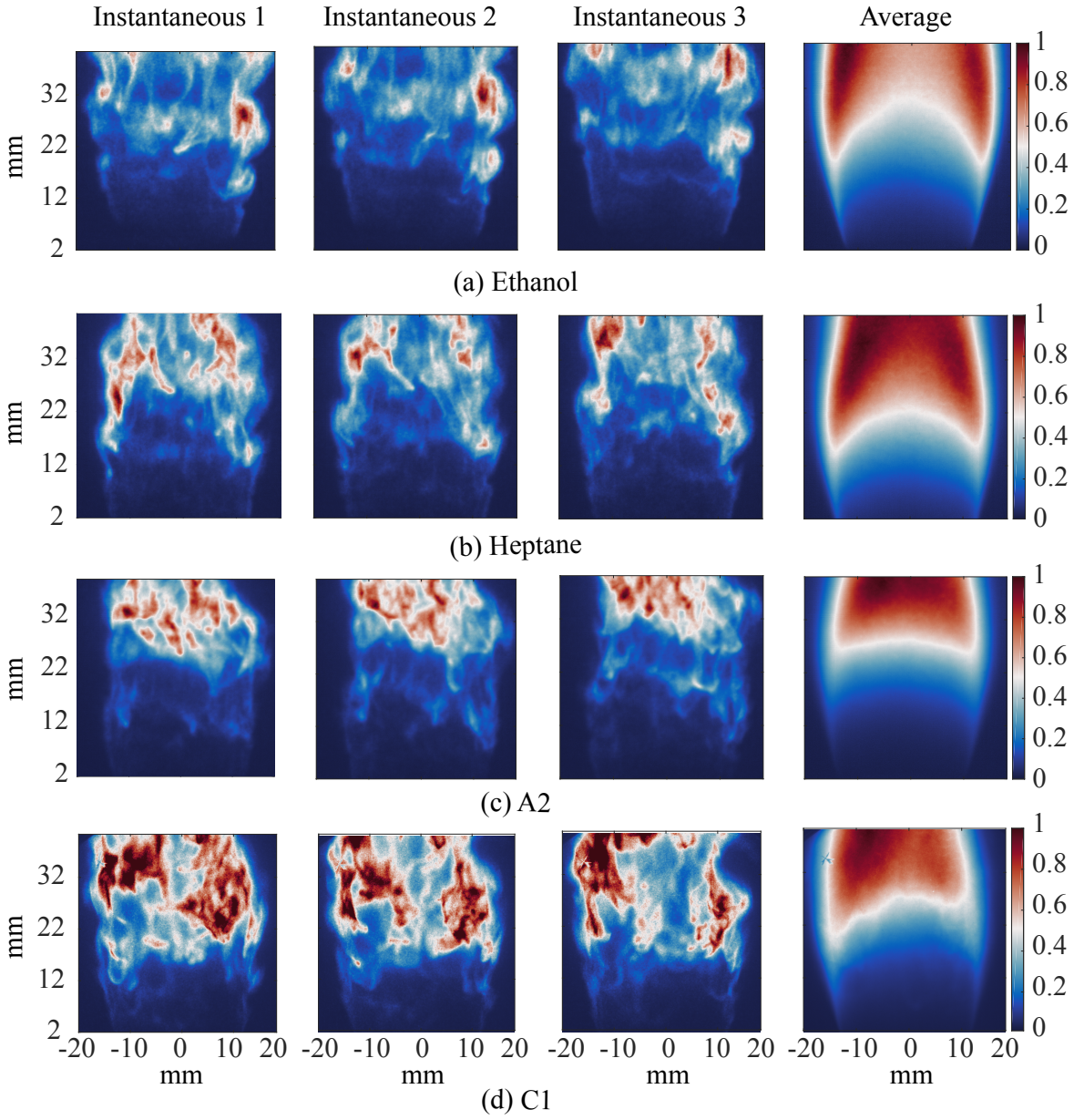

Fig. 6.1 OH* chemiluminescence images at far from blow-off. First, second and third column represents the statistically independent instantaneous images. Fourth column represents the average images obtained by averaging 5400 instantaneous images. The centre line of the bluff body is represented by the '0' in radial axis.

Figures 6.1 and 6.2 show the instantaneous and average images with ethanol, heptane, A2, and C1 from conditions far from and close to blow-off, respectively. The instantaneous images from conditions far from blow-off exhibit high intensity OH* chemiluminescence signal along the shear layer. The high-intensity island of OH* were observed in the instantaneous images with all four flames. These localized high-intensity islands of OH* were more pronounced in the kerosene and heptane flames. Such localized increase in OH* signal may be associated with the continuous re-ignition of the flame in RZ as observed by Ref. [63]. The average images are shown in the rightmost column of Fig. 6.1 highlight the features of the instantaneous images. Overall, when far from blow-off, all four flames display similar structure with low intensity OH* signal close to the bluff body and high intensities in the downstream regions.

Figure 6.2 shows similar information as Fig. 6.1, but from conditions close to LBO. It is evident from Fig. 6.2 that all four flames become shorter as ϕ was reduced. The highest intensity of the OH* signal was observed to exist in regions 30-40 mm downstream of the bluff body in the RZ. During blow-off, the methane flames exhibited a similar shortening and confinement within the RZ as in Ref. [29]. From the velocity field measurements presented in Ref. [29], the height of the RZ was determined to be 1.5 - 2 times the bluff-body diameter. Since the burner employed here is similar to that in Refs. [29], the RZ is estimated to extend 46 mm downstream of the bluff body. Thus, similar to the methane flames [29], vapourised liquid fuels close to blow-off (Fig. 6.2) exhibit a large amount of reaction within the RZ. These flames become narrow at their tip, implying that flame fronts from the opposite sides of the burner merge, leading to the closing of the RZ in the downstream region (see average images in Fig. 6.2). Similar behaviour was observed with methane-, propane-, and ethylene-fueled flames in Refs. [32, 29, 17, 31].

The average OH* images presented indicate that the flames are symmetric; thus, these images were Abel transformed to provide a projection of the mean reaction rate within a 2-D plane [32]. Figure 6.3a and b displays the Abel transformation of averaged OH* chemiluminescence images for all flames at conditions far from and close to blow-off. When far from blow-off, the Abel transformed images appear similar for all four flames. The primary reactions are concentrated along the annular jet of the reactants. Low signal intensity inside the RZ can be related to the burnt gases. At conditions close to blow-off, reaction zones are observed inside the RZ. Additionally, in the downstream part of the flames, the two flame brushes from both sides of the burner are observed to merge together. Moreover, flames operated with heptane and kerosene (A2 and C1) display average reaction regions closer to the bluff body than those fueled with ethanol. These findings are consistent with

those presented in Ref. [32, 29], where average reaction regions were observed within the RZ of methane flames.

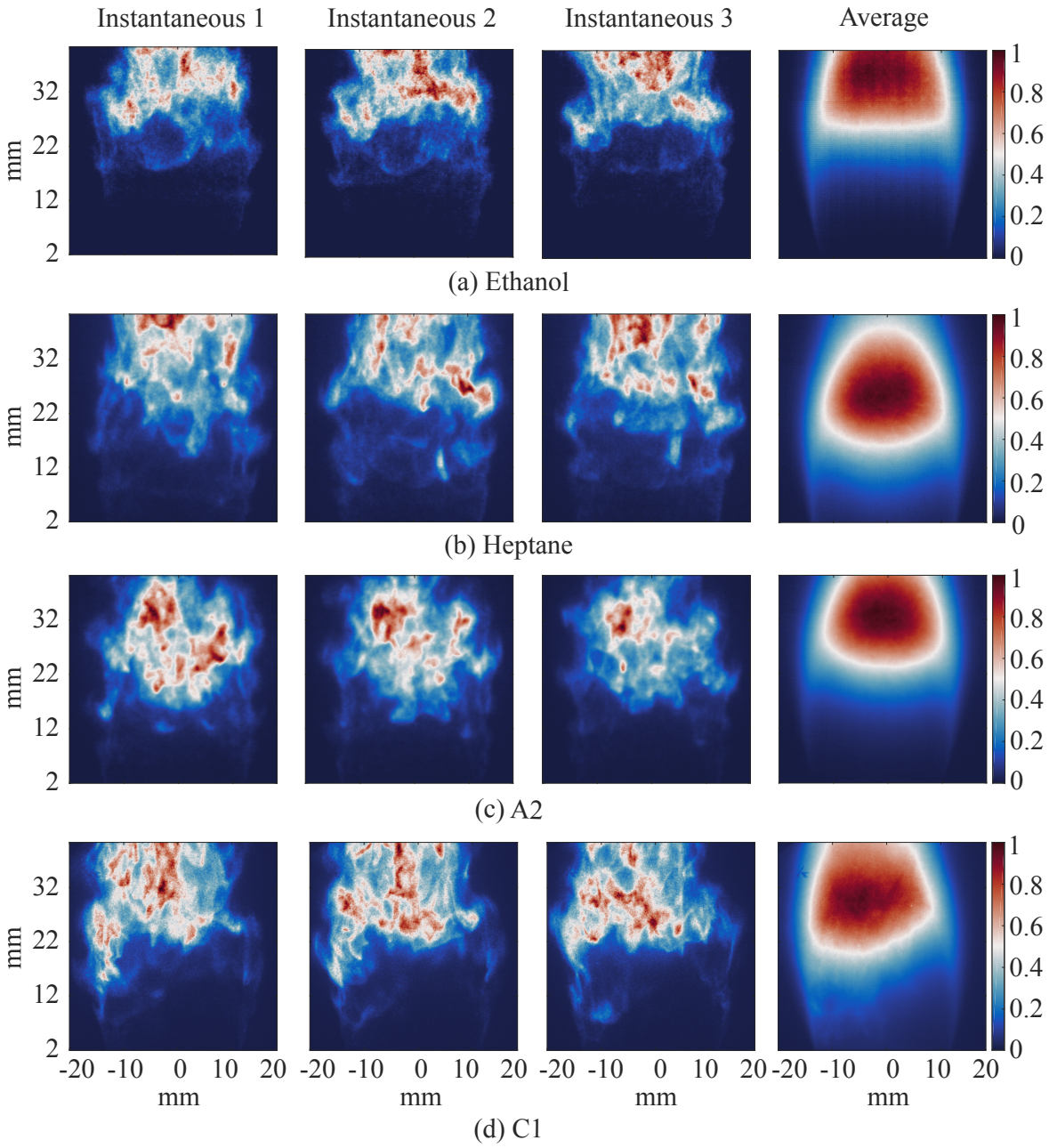

Fig. 6.2 OH* chemiluminescence images at close to blow-off. First, second and third column represents the statistically independent instantaneous images. Fourth column represents the average images obtained by averaging 5400 instantaneous images. The centre line of the bluff body is represented by the '0' in radial axis.

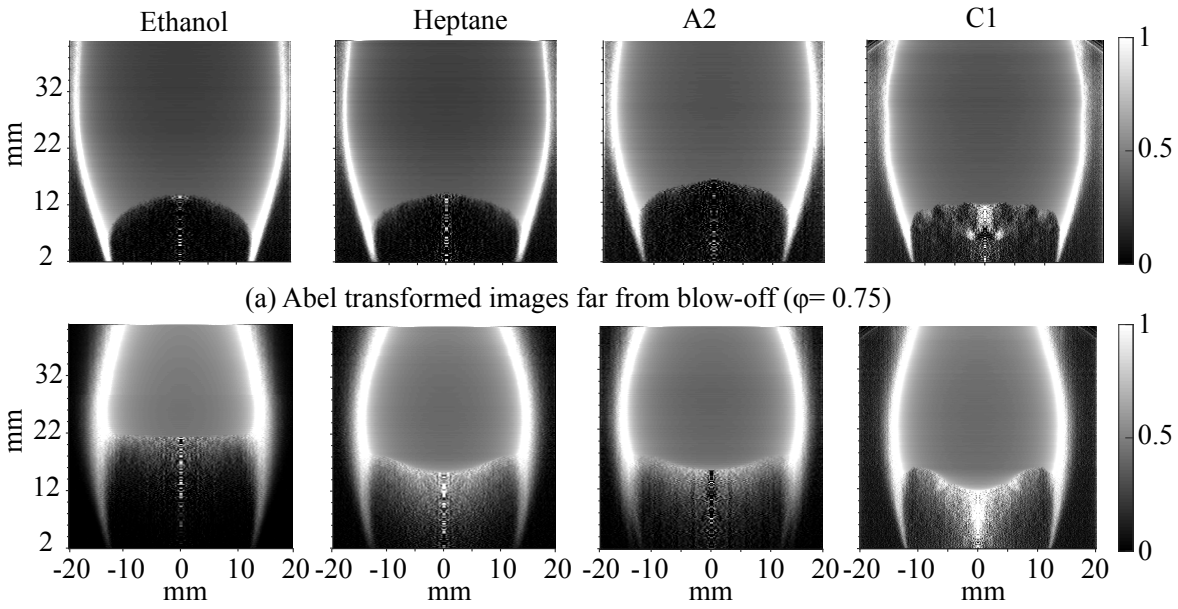

(a) Abel transformed images far from blow-off (φ= 0.75)

(b) Abel transformed images close to blow-off (φ/φ_{bo}= 1.01)

Fig. 6.3 Abel transformed images with ethanol, heptane, A2 and C1.

6.2 OH-PLIF structure

Figure 6.4 presents instantaneous and average OH-PLIF images at conditions far from blow-off ($\phi/\phi_{bo} = 1.20$). Higher intensity patches of OH-LIF signal are concentrated along the shear layer, while lower levels of signal fill the RZ region above the bluff body. At these stable burning conditions, the flame fronts near the bluff body showed the Kelvin-Helmholtz instability that is common to bluff body flames (see Refs. [31, 29, 17, 30]). These instabilities were observed to manifest in the form of roll-ups in the downstream region (22-32 mm) of the flame. This behaviour of the flame was observed with all fuels at stable conditions. Similar distributions of OH-LIF signal were observed in stable methane flames studied by Kariuki et al. [29].

Averaged images shown in the rightmost column of Fig. 6.4 exemplify the features displayed in the instantaneous images. The heptane-, A2-, and C1-flames exhibit large OH-LIF signal within the RZ. In contrast, the OH-LIF signals are concentrated along the annular jet of the ethanol flames, which is likely due to ethanol's chemical composition. Namely, each ethanol molecule contains OH through a single bond that likely breaks away from the rest of the molecule as the fuel cracks, resulting in a locally higher OH concentration near the flame front.

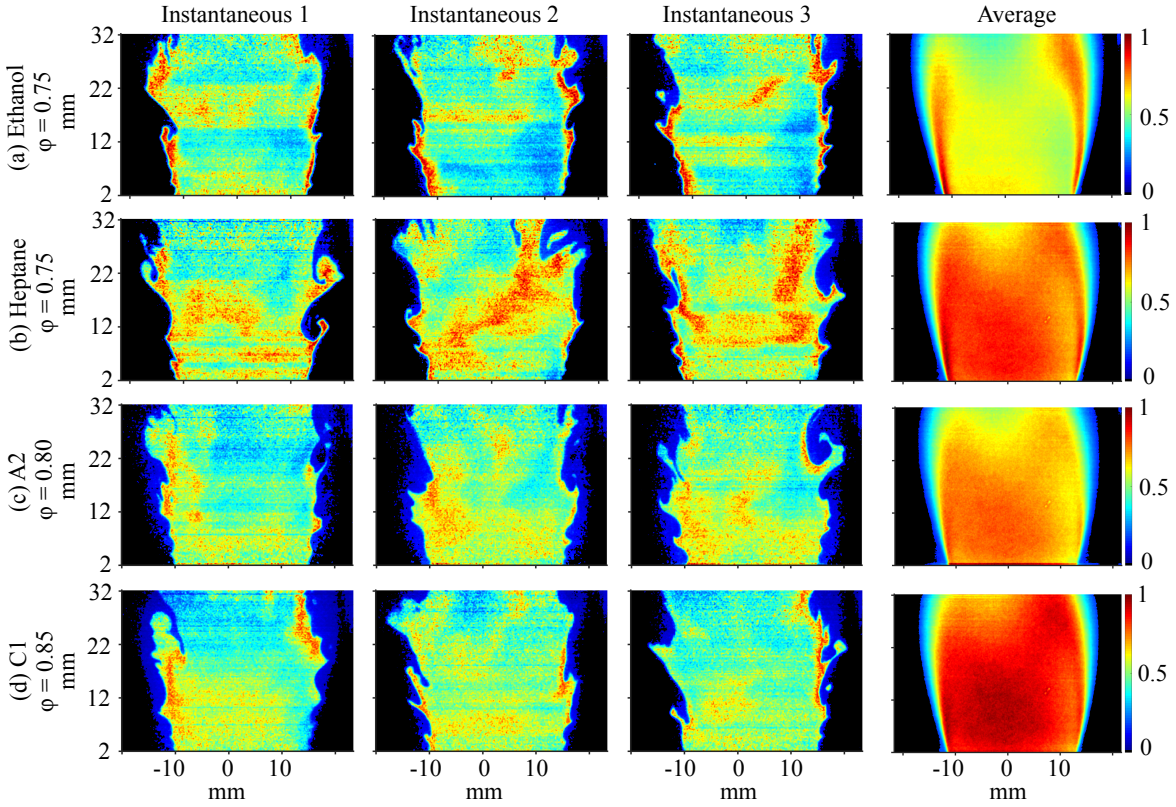

Fig. 6.4 Instantaneous and average OH-PLIF images at $\phi/\phi_{BO} = 1.20$ at $U_b = 23 \pm 1.5$ m/s with ethanol, heptane, A2 and C1. First, second and third column represents the statistically independent instantaneous OH-PLIF images. Fourth column represents the average images obtained by averaging 5000 instantaneous images.

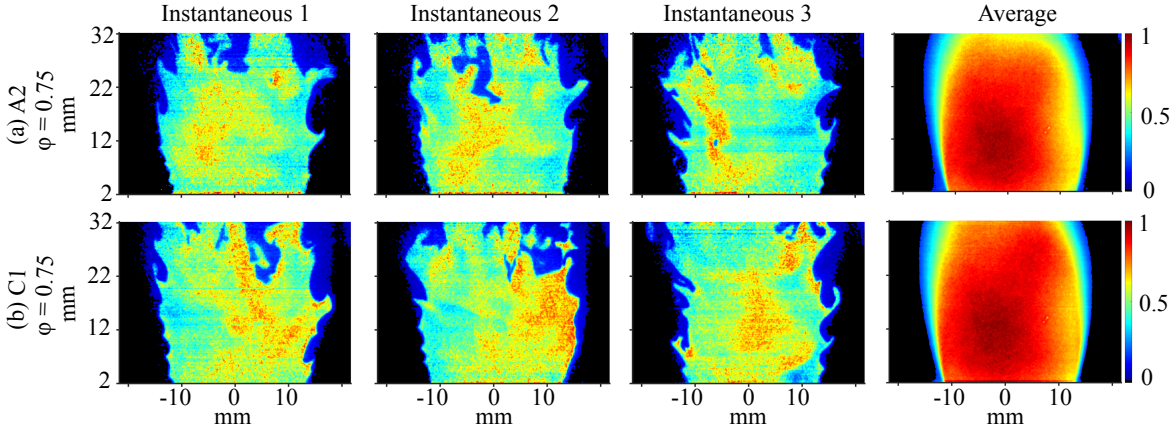

Fig. 6.5 Instantaneous and average OH-PLIF images with A2 and C1 at $\phi = 0.75$, corresponding to a ϕ/ϕ_{bo} of 1.09 and 1.05, respectively. First, second and third column represents the statistically independent instantaneous OH-PLIF images. Fourth column represents the average images obtained by averaging 5000 instantaneous images.

Figure 6.5 displays instantaneous images from A2- and C1-flames with $\phi = 0.75$, corresponding to a ϕ/ϕ_{bo} of 1.09 and 1.05, respectively. In comparison to the more robust flames in Fig. 6.4, in Fig. 6.5 the OH-LIF signal is observed to decrease along the flame front yet increase within the RZ. Also, the OH-LIF signal is fragmented in the downstream regions (20-32 mm) of the flame (see Fig. 6.5). Pockets void of OH-LIF signal are seen to enter from the downstream region of the RZ. The formation of these pockets may result from the entrainment of partially reacted or cold reactants into the RZ from the downstream regions of the flame. The average images presented in the rightmost column of Fig. 6.5 indicate that the peak OH-LIF signals are primarily concentrated within the RZ along the centerline of the bluff body.

Figure 6.6 presents instantaneous images obtained near the blow-off limit of the present flames. A substantial change in the flame structure was observed with all four fuels. The instantaneous images highlight an increase in OH-LIF signal intensity in the RZ. The OH-LIF signal becomes distorted (i.e. small pockets OH-LIF signal are observed in the region from $20-32$ mm), and the height of the OH-filled region decreases. The results are consistent with the time-averaged OH* chemiluminescence images reported in previous studies Refs. [29], which show the presence of reaction zones in the RZ above the bluff body and a shortening of the flame as it approaches blow-off. Pockets void of OH-LIF signal were observed in the downstream region (22-32 mm) of the flames considered. The regions void of OH-LIF signal may consist of preheated reactants that enter the RZ from the downstream region. As shown in Section 6.7, small patches of CH_2O signal are visible in the RZ at conditions close to blow-off. Thus, it is likely that the pockets void of OH in Fig. 6.6 are filled with CH_2O, which was the case for the methane flames studied in Ref. [36].

For all four flames in Fig. 6.6, three dominant events were observed. Such events are 1) the formation of pockets void of OH (marked by blue triangles), 2) the development of OH-filled pockets (marked by white circles), and 3) the production of finger-like structures (marked by magenta rectangles). For the ethanol flames, pockets void of OH are primarily confined to the region roughly $22-32$ mm downstream of the bluff body. However, such pockets are found closer to the bluff body (12-22 mm) for flames produced with the other three fuels (see Figs. 6.6b - 6.6d). Also, the heptane and two kerosene flames exhibited a higher tendency of forming pockets both filled with and void of OH-LIF signal. Notably, it was found that the A2 flames have almost three-times more OH-LIF pockets during a blow-off event than methane flames.

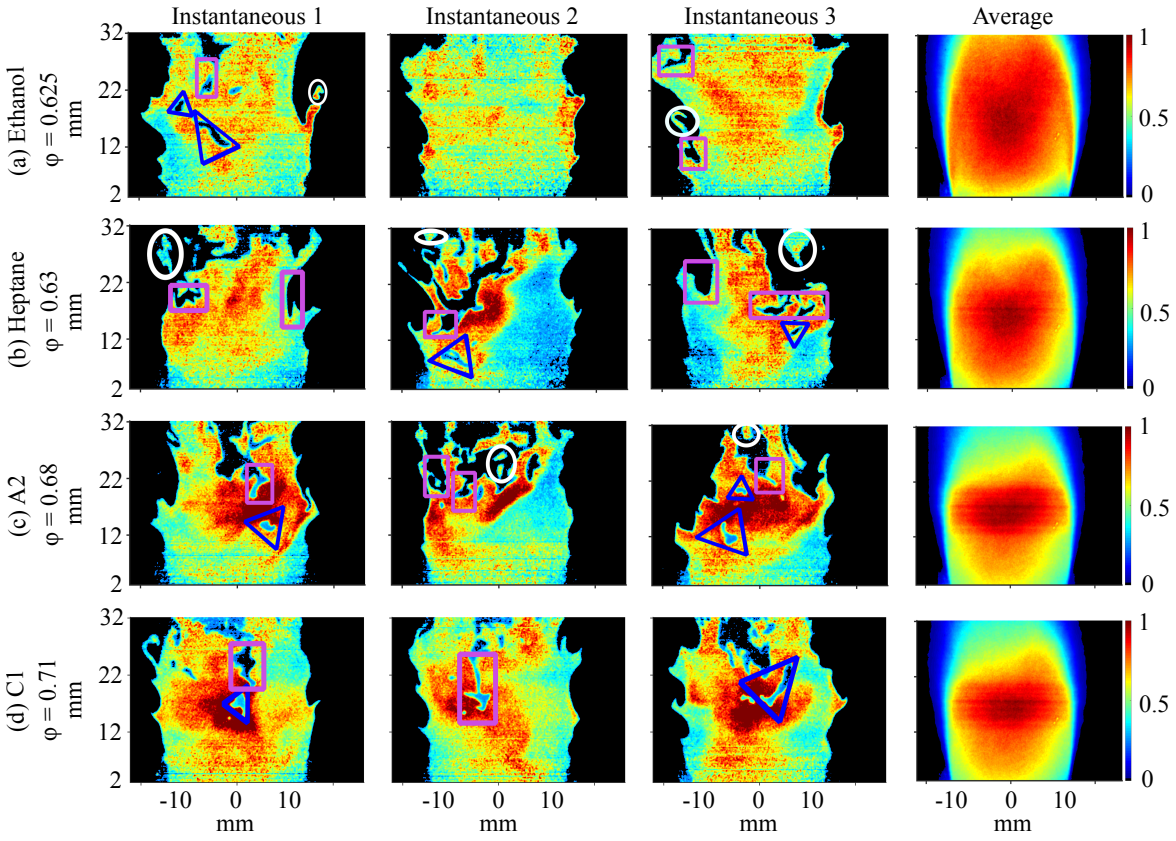

Fig. 6.6 Instantaneous and average OH-PLIF images at $\phi/\phi_{BO} = 1.01$ at $U_b = 23\pm1.5$ m/s with ethanol, heptane, A2 and C1. First, second and third column represents the statistically independent instantaneous OH-PLIF images. Fourth column represents the average images obtained by averaging 5000 instantaneous images.

The finger-like structures, separated by regions lacking OH signal, were also observed in Refs. [29, 17, 30]. These finger-like structures were observed to enter from the downstream region and penetrate the RZ to a point just above the bluff body. Kerosene (A2 and C1) flames have a higher propensity to form these fingers-like features. A similar observation of entrainment of partially burnt or unburnt reactants into the RZ and flame recession into the RZ was also observed in Refs. [29, 31]. Average OH-PLIF images presented in the right-most column of Fig. 6.6 are consistent with the instantaneous results, indicating that the highest intensity of OH-LIF signal is concentrated along the centerline of the bluff body in all four flames.

The OH-PLIF images presented here suggest that all flames exhibit similar flame structures under stable conditions. As indicated by Fig. 6.6, a change in flame shape is observed as blow-off is approached. The flame becomes shorter with the peak OH-LIF signal lying within the RZ above the bluff body. However, close to blow-off, kerosene flames (A2 and C1) appear shorter with more fragmented pockets of OH-LIF signal than the other flames.

Since the kerosene flames are the least stable, this observation suggests a link between an increase in the level of fragmentation due to local extinction and reduced stability limits.

6.3 Average reaction progress variable

As discussed in section 2.3.2, the mean progress variable ($\bar{c}$) was determined by averaging the complete data set of binarized OH-PLIF images. Figures 6.7a and 6.7b display $\bar{c}$-maps with contours of 0.2, 0.4, 0.6 and 0.8 (with 0.2 contour as the outermost line and 0.8 contour as the innermost line) superimposed for all four fuels at conditions far from and close to blow-off, respectively. The spacing in the $\bar{c}$ contours increases from the anchoring to the downstream region. However, regardless of fuel type, there is no significant difference between the $\bar{c}$-fields under stable burning conditions (top row). A similar trend in the $\bar{c}$ contours were observed in stable-burning methane flames [29, 37, 80].

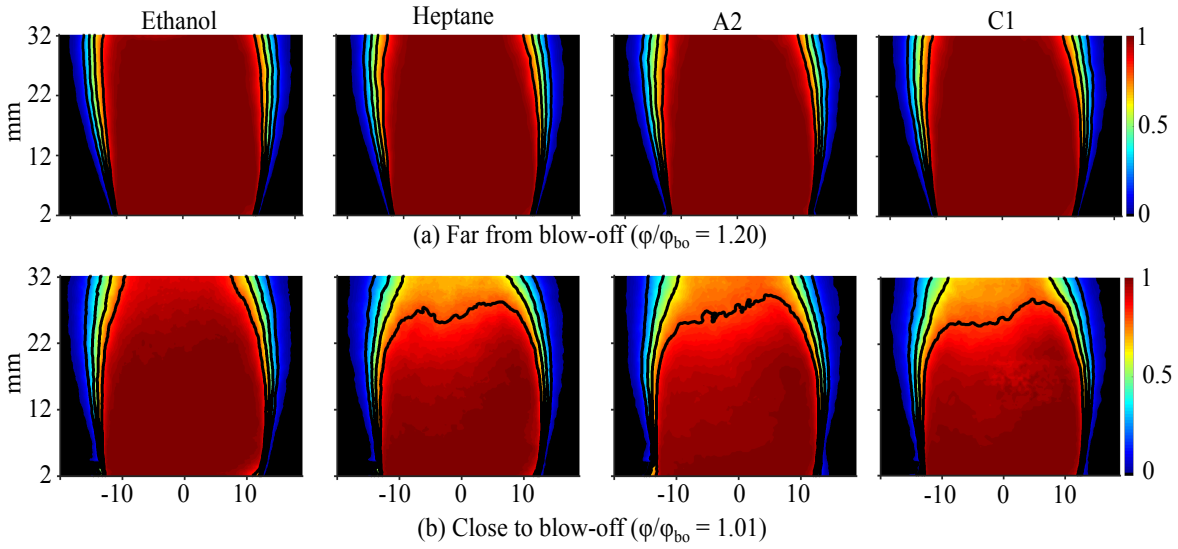

Fig. 6.7 Maps of average progress variable $\bar{c}$ with the $\bar{c}$ = 0.2 , 0.4, 0.6 and 0.8 isoline superimposed for ethanol, heptane A2 and C1 flames.

As shown in Fig. 6.7b, the mean flame surface changes as blow-off is approached. It was found that the $\bar{c}$ = 0.8 contour recedes to the RZ and is even observed in the downstream region. The spacing between the $\bar{c}$ contours increases significantly in the downstream part of the heptane- and kerosene-flames. The ethanol flame also exhibits an increased separation between the $\bar{c}$ contours in its downstream region, but the effect was not as significant as in the other three flames. Kariuki et al. [29] observed a similar recession into the RZ of the $\bar{c}$ contours in the downstream regions of methane flames close to blow-off.

6.4 Flame surface density

Figure 6.8 presents FSD as a function of $\bar{c}$ for all four flames in the anchoring and downstream regions. It is observed that the FSD peaks at $\bar{c} = 0.5$ for all four flames. As shown in Fig. 2.1b, the flames are divided into two regions. Figures 6.8a and 6.8b present the FSD in the anchoring and downstream region for stable flames, respectively. The peak FSD was reduced by $\sim$50% between the flame's anchoring and downstream regions. This trend of decreasing peak FSD with increased distance from the burner is also true for flames close to blow-off. Namely, the peak FSD values reduced by $\sim$33% when going from the anchoring to the downstream region of near-limit flames (see Figs. 6.8c and 6.8d). Additionally, within the anchoring region (Fig. 6.8a and c), the peak FSD values are found to decrease as blow-off is approached. A similar decrease in the peak FSD within the anchoring regions of methane flames approaching blow-off was reported in Refs. [29, 80, 37]. Yet, the peak FSD values within the downstream region are approximately the same regardless of the flames proximity to their lean blow-off limits.

In the downstream region of the heptane, A2, and C1 flames close to blow-off (see Fig. 6.8d), a decrease in the FSD value is observed at $\bar{c} \geq 0.7$. This decrease of FSD at $\bar{c} = 0.7$ may be due to the recession of the flame into the RZ or a higher degree of localized extinction events occurring in heptane and two kerosene flames than in the ethanol flame. Overall, it was observed that the FSD decreases as the flames approached blow-off, and this decrease can be as high as $\sim$50% in the anchoring region. A reduction in FSD with increasing u'/S_L^0 (see Table 2.2) as the flame approaches blow-off was observed by Kariuki et al. [29]. This reduction in FSD is may be due to the reduced burning rate. As indicated by Figs. 6.8, the FSD exhibit little to no dependence on fuel type. This is true regardless of measurement location and proximity of the flames to their LBO limits (See Fig. 4.1). Hence, this suggests that FSD is not a sufficient metric for indicating the onset of blow-off. However, it should be pointed out that this conclusion may be an artifact of the present OH-based definition of Σ, which is based on OH-PLIF that after binarization neglects regions of intermediate progress variable.

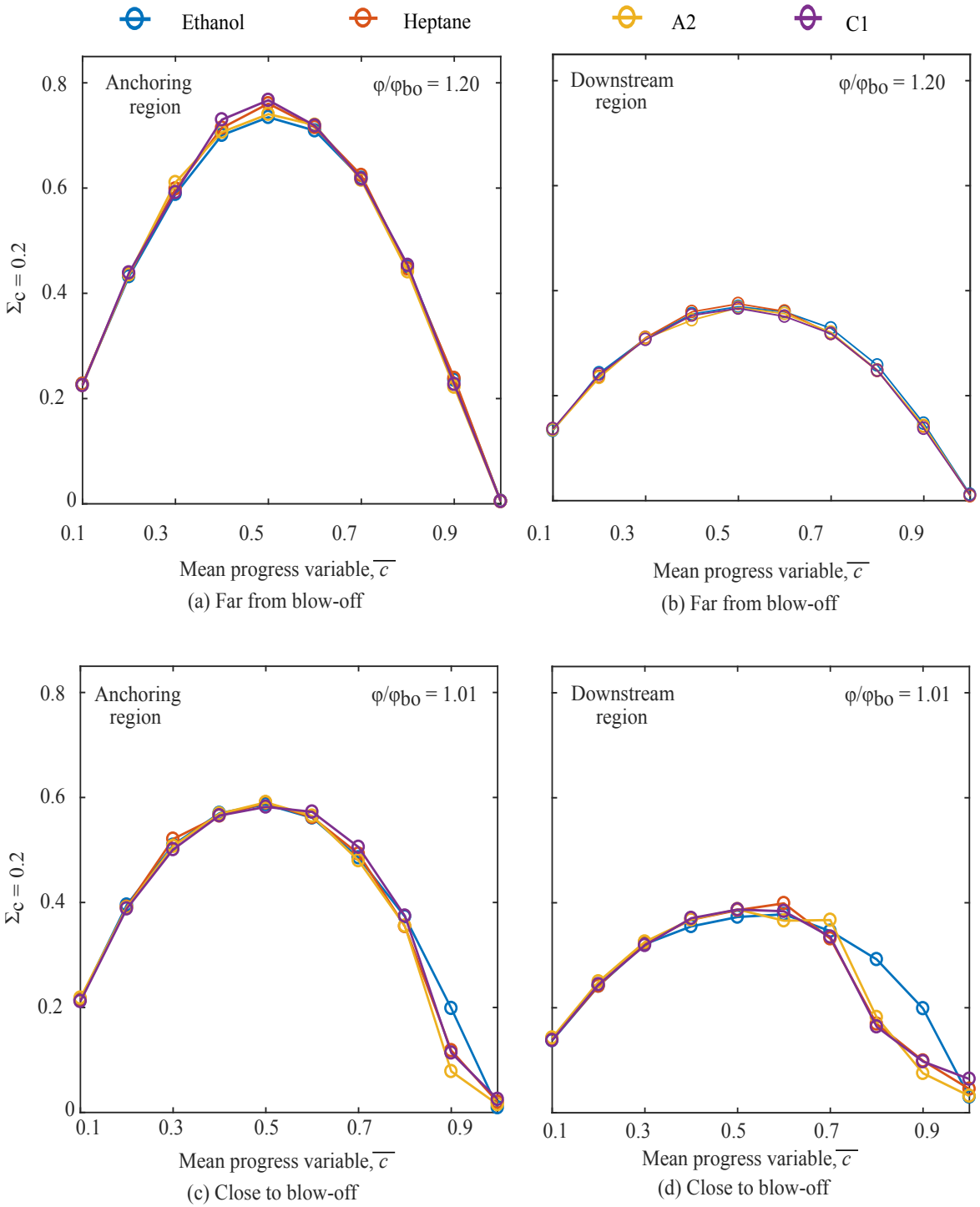

Fig. 6.8 FSD evaluated at 20 % contour (c=0.2) with ethanol, heptane, A2 and C1 in the anchoring region (2 – 15 mm) and downstream region (15 – 32 mm) of the flame.

6.5 2-D curvature

The instantaneous images (Figs. 6.4 and 6.6) suggested that flame wrinkling increased as the flames approached blow-off.

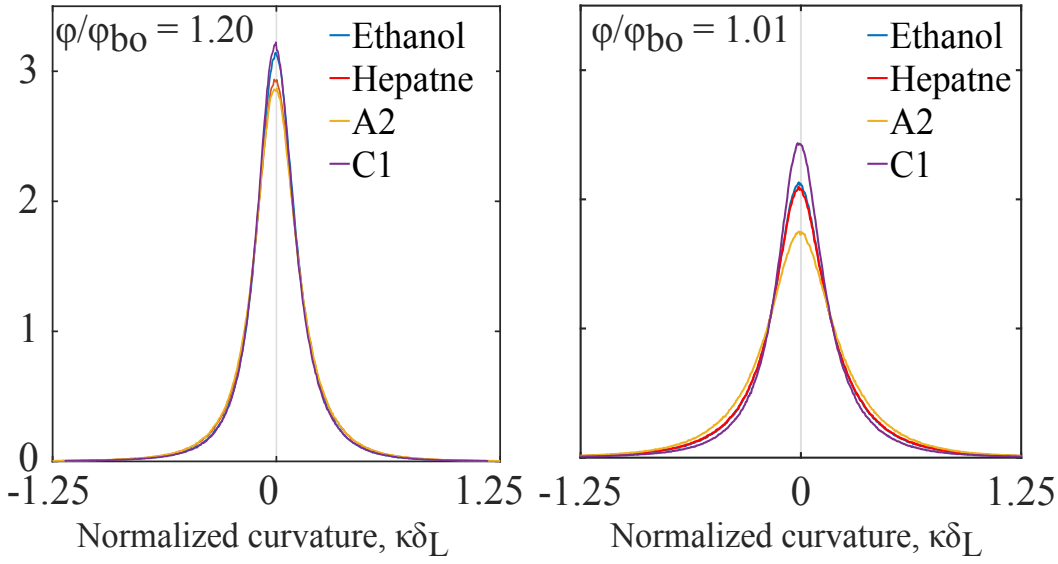

(a) Far from blow-off (b) Close to blow-off

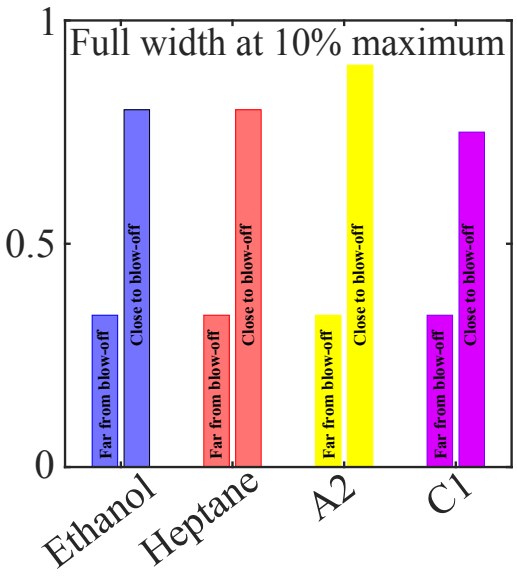

(c) Curvature PDF width

Fig. 6.9 Probability density functions of normalised curvature ($\kappa\delta_l$) for ethanol, heptane, A2 and C1.

To further assess this observation, the 2-D flame-front curvature (κ) at 20 % contour (c=0.2) was measured. Figure 6.9 presents PDFs of the normalized curvature ($\kappa\delta_L$). The

PDFs of $\kappa\delta_L$ are symmetric about $\kappa\delta_L \approx 0$, and the distribution appears Gaussian. Figure 6.9 indicates that, regardless of fuel type, the curvature distribution broadened as blow-off was approached.

To facilitate a more quantitative assessment of the PDFs in Fig. 6.9, their widths at 10% of maximum were extracted. Figure 6.9c displays the widths of the curvature PDFs for each fuel considered under conditions far from and close to blow-off. Under stable burning conditions, the widths are similar, yet they clearly increase as LBO is approached. Close to blow-off, A2 showed the maximum width of $\kappa\delta_L \sim 0.90$ and C1 exhibits a minimum width of $\kappa\delta_L \sim 0.75$, whereas, ethanol and heptane possessed $\kappa\delta_L$ of $\sim$0.80. The smaller width of the $\kappa\delta$-pdf associated with the C1-fueled flames implies they are less wrinkled than ethanol, heptane, and A2.

6.6 Local turbulent consumption speed

The OH-PLIF images were further analysed to obtain local turbulent consumption speed ($S_{T,LC}$). $S_{T,LC}$ represents a local estimate of a turbulent premixed flames average consumption speed. Damkhöler proposed that $S_{T,LC}$ increases with u', because higher turbulence results in larger flame surface generation [84]. Here, $S_{T,LC}$ was determined as in Refs. [37, 141], namely, it was evaluated by integrating 2-D FSD presented in section 6.4, and then accounting for angle between horizontal and average flame front ($\bar{c} = 0.5$; see Eq. A2 in Ref. [37]).

Figure 6.10 shows plots $S_{T,LC}/S_L$ vs. y (axial distance along the flame) from conditions far from and close to blow-off with all four fuels. At a condition far from blow-off, $S_{T,LC}/S_L$ was observed to increase with axial distance modestly and reaches a maximum value of $\approx$5.5 in the downstream regions. Likewise, $S_{T,LC}/S_L$ also increased with axial distance under conditions near blow-off. The increase in $S_{T,LC}/S_L$ with axial distance can be related to an increase in u'/U_b, which increased flame wrinkling (see Fig. 6.4 and 6.6). A similar increase in $S_{T,LC}/S_L$ with increasing u'/U_b was observed in Refs. [142, 30, 37, 141, 8]. Additionally, close to blow-off, $S_{T,LC}/S_L$ was increased by a factor of three. This increase in $S_{T,LC}/S_L$ can be related to a drop in S_L as blow-off was approached, as the variation of u'/U_b is similar for all flames since they had the same U_b (see Fig. 6.19a).

In the near field region (up to 20 mm), no significant difference in $S_{T,LC}/S_L$ was observed between all four fuels at both conditions. Trabold et al. [39] observed a similar value of integrated FSD in the near field for alcohol and methane flames. They hypothesized that in near field regions, the fame surface is mostly influenced by turbulent shear flow. The flames studied here are dominated by shear as well, and the shear rate is high close to the bluff body. Therefore, in these regions, the fuel type has little or no effect on

$S_{T,LC}/S_L$. In the downstream regions (beyond 20 mm), where the influence of shear starts to decrease, $S_{T,LC}/S_L$ start deviating amongst the different fuel types, with the effect being more pronounced at conditions close to blow-off. Note that close to blow-off, C1 exhibits a lower value of $S_{T,LC}/S_L$ in the downstream region as compared to the other flames. The drop-in $S_{T,LC}/S_L$ can be related to more local extinction in the downstream region of C1.

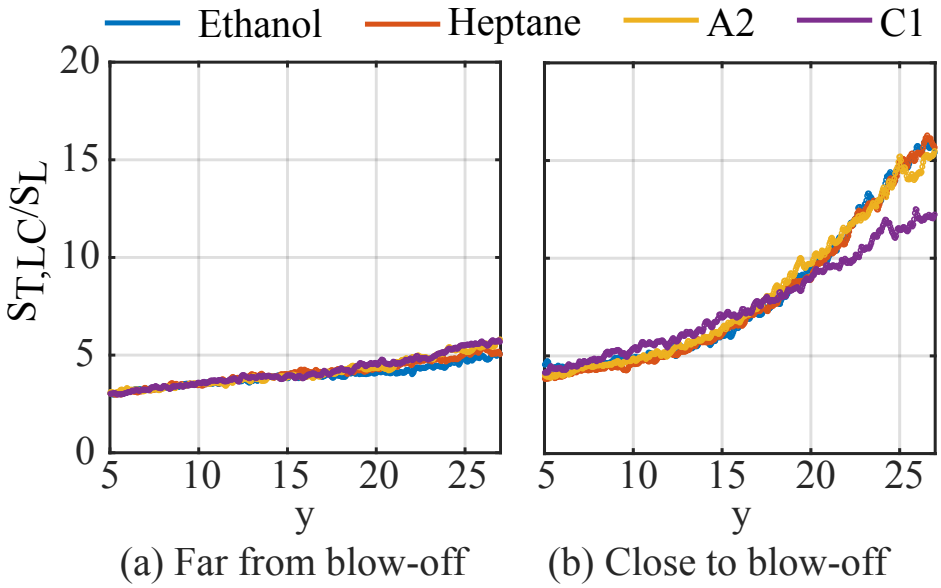

Fig. 6.10 Turbulent local consumption speed at condition far from and close to blow-off.

6.7 CH_2O-PLIF structure

Figure 6.11 shows instantaneous and average CH_2O-PLIF images from conditions far from blow-off. Regions of high-intensity CH_2O-LIF signal are seen to be concentrated along the shear layer with occasional vortex-like structures appearing in all four flames. The average images presented in the rightmost column of Fig. 6.11 depict the same CH_2O structure as observed in instantaneous images.

Figure 6.12 present CH_2O structure at the same $\phi = 0.75$ for the two kerosene flames (A2 and C1), yet note ϕ/ϕ_{BO} is not consistent between the two fuels in this figure. The pockets of preheated reactants were observed inside the RZ. These pockets appear to enter the RZ from the downstream region. Compared to the average CH_2O-PLIF images in the rightmost column of Fig. 6.12 to those corresponding to the kerosene flames in Fig. 6.11, it suggests that, on average, the CH_2O layers occupy a broader region as ϕ is decreased. This is particularly true in the downstream regions where the average CH_2O signal from opposing sides of the burner appears to merge and even enter the RZ. Additionally, though

$\phi = 0.75$ for both kerosene flames in Fig. 6.12 and both single-component fuels in Fig. 6.11, it is evident that, on average, the former exhibit more broadly distributed CH_2O layers. This, again, is predominantly true in the downstream region.

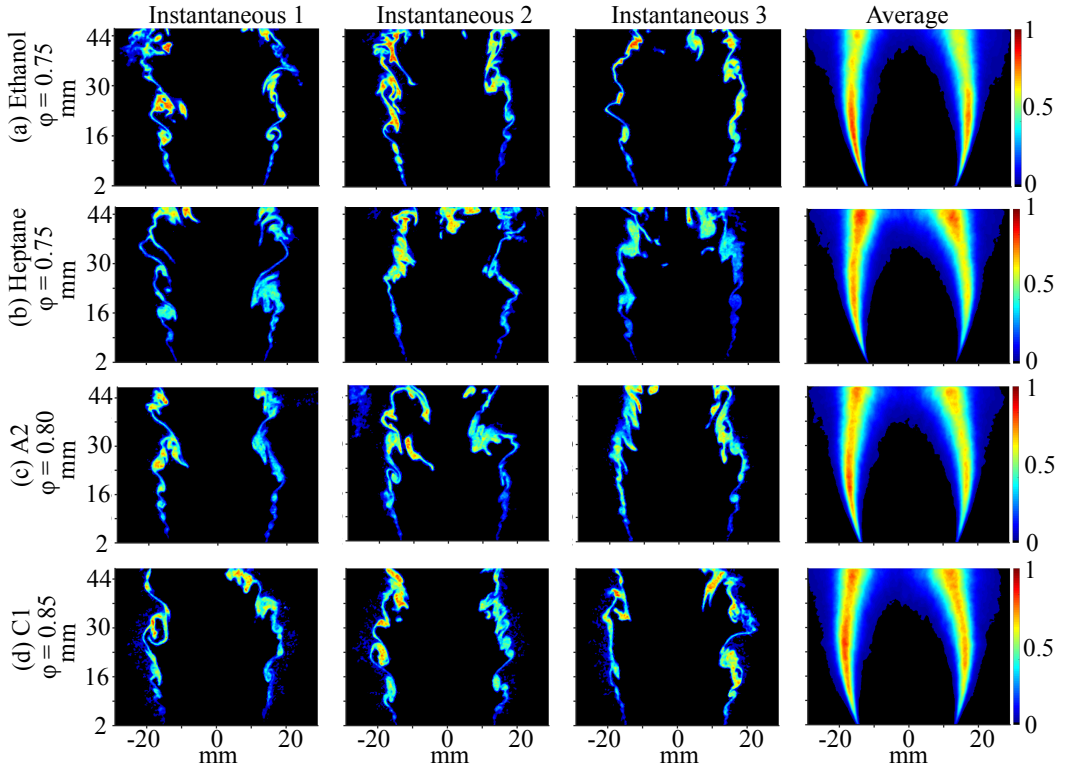

Fig. 6.11 Instantaneous and average images CH_2O images far from blow-off ($\phi/\phi_{bo} = 1.20$) at U_b = 23±1.5 m/s with ethanol, heptane, A2 and C1. First, second and third column represents the statistically independent instantaneous CH_2O-PLIF images. Fourth column represents the average images obtained by averaging 700 instantaneous images.

Figure 6.13 shows the CH_2O-PLIF images obtained from conditions close to blow-off ($\phi/\phi_{BO} = 1.01$). The CH_2O-LIF signal increased with axial distance from the bluff body, while broad regions of CH_2O are observed in the downstream part of the RZ for all four flames. Additionally, individual pockets and long peninsulas of CH_2O appeared in the RZ close to the bluff body. These pockets lend support to the aforementioned claim that voids in the OH-PLIF images likely consist of CH_2O.

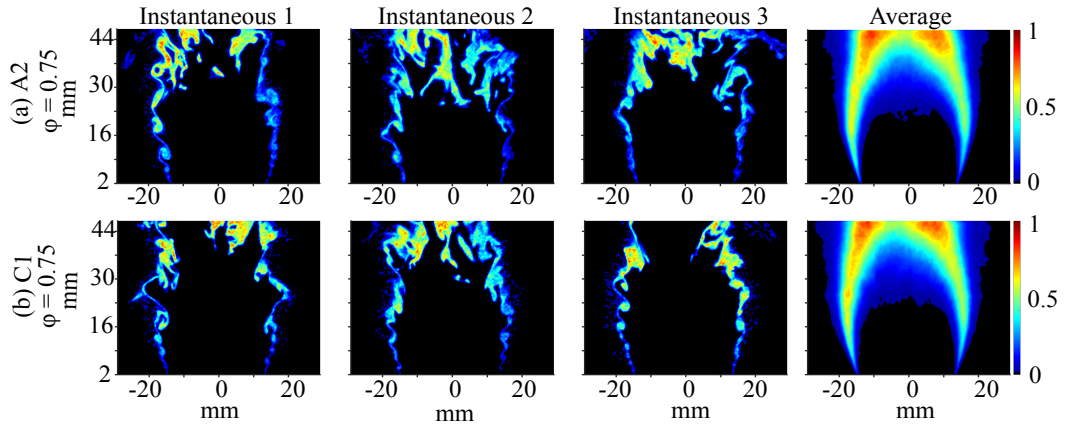

Fig. 6.12 Instantaneous and average CH_2O images with A2 and C1 at $\phi = 0.75$, corresponding to a ϕ/ϕ_{bo} of 1.09 and 1.05, respectively. First, second and third column represents the statistically independent instantaneous CH_2O-PLIF images. Fourth column represents the average images obtained by averaging 700 instantaneous images.

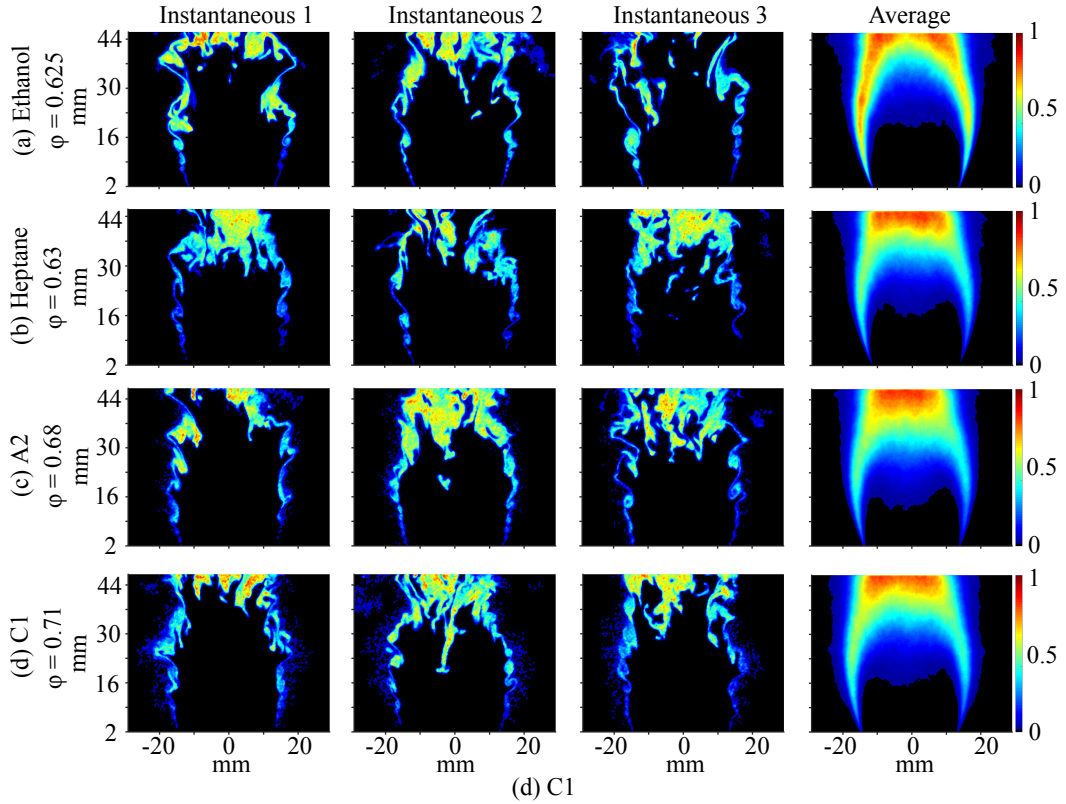

Fig. 6.13 Instantaneous and average CH_2O images at $\phi/\phi_{BO} = 1.01$ at U_b = 23±1.5 m/s with ethanol, heptane, A2 and C1.First, second and third column represents the statistically independent instantaneous CH_2O-PLIF images. Fourth column represents the average images obtained by averaging 700 instantaneous images.

Furthermore, it can be seen from the CH_2O-PLIF images that the CH_2O layers merge and cross across the bluff body in the downstream portion of RZ. For all fuels, conditions close to blow-off commonly possessed large pockets of CH_2O were frequently observed within the RZ above the bluff body as they approached blow-off. However, heptane and the two kerosene flames tended to have wider regions of CH_2O than the ethanol flame. The average CH_2O-PLIF images are shown in the rightmost column of Fig. 6.13 for each of the fuels with $\phi/\phi_{BO} = 1.01$. Overall, these average images appear quite similar for the different flames. Namely, relatively thin regions exist close to the bluff body, while a wider, more distributed region of average CH_2O-LIF signal is observed in the downstream locations (e.g. > 30 mm above the bluff body).

6.8 CH_2O-layer thickness

Figure 6.14 presents PDFs of CH_2O-layer thicknesses (as explained in Section 2.3.3) normalized by $\delta(l)^*_{CH_2O}$. Figures 6.14a and 6.14b display PDFs of the CH_2O-layer thickness obtained under stable conditions at two axial locations: $20-25$ mm and $35-40$ mm from the burner exit, respectively. Regardless of the fuel used, the CH_2O-layer thickness ranges from 2 to 6 $\times\delta(l)^*_{CH_2O}$ in the near-field region ($20-25$ mm) of the stable burning flames (Fig. 6.14a). Yet, the PDFs in Fig. 6.14b, indicate that the CH_2O layers exhibit a higher probability of being upwards of eight times larger than $\delta(l)^*_{CH_2O}$ in the downstream region ($35-40$ mm). This corroborates the observations in section 6.7, where the CH_2O layers were observed to broaden with increased axial distance. However, regardless of axial position in the flame, the most probable values of the measured CH_2O-layer thickness is found to be $\sim 2\times\delta(l)^*_{CH_2O}$. Note that the C1-fueled flames tend to have the thinnest CH_2O-layer thicknesses in both locations.

Under conditions close to blow-off (Fig. 6.14c and d), significant broadening of CH_2O-layer thickness can be seen in comparison to the condition far from blow-off. In the near field regions ($20-25$ mm, Fig. 6.14c), all four flames exhibit similar CH_2O-layer thickness, which range from 3 to 8 $\delta(l)^*_{CH_2O}$. In contrast, a considerable increase in the CH_2O-layer thickness is observed in the downstream regions with all four fuels. The PDFs of CH_2O-layer thicknesses extend up to $20\delta(l)^*_{CH_2O}$. Additionally, the PDFs for the heptane, A2, and C1 flames exhibit a double peak. The second peaks (marked by the blue circle) in these PDFs (towards high thickness values, $\sim 12\times\delta(l)^*_{CH_2O}$) likely result from flame merging at the top of the RZ, at both the large scale with the two sides of the flame merging and at the small-scale due to curvature and local extinction, phenomena that lead to the destruction of

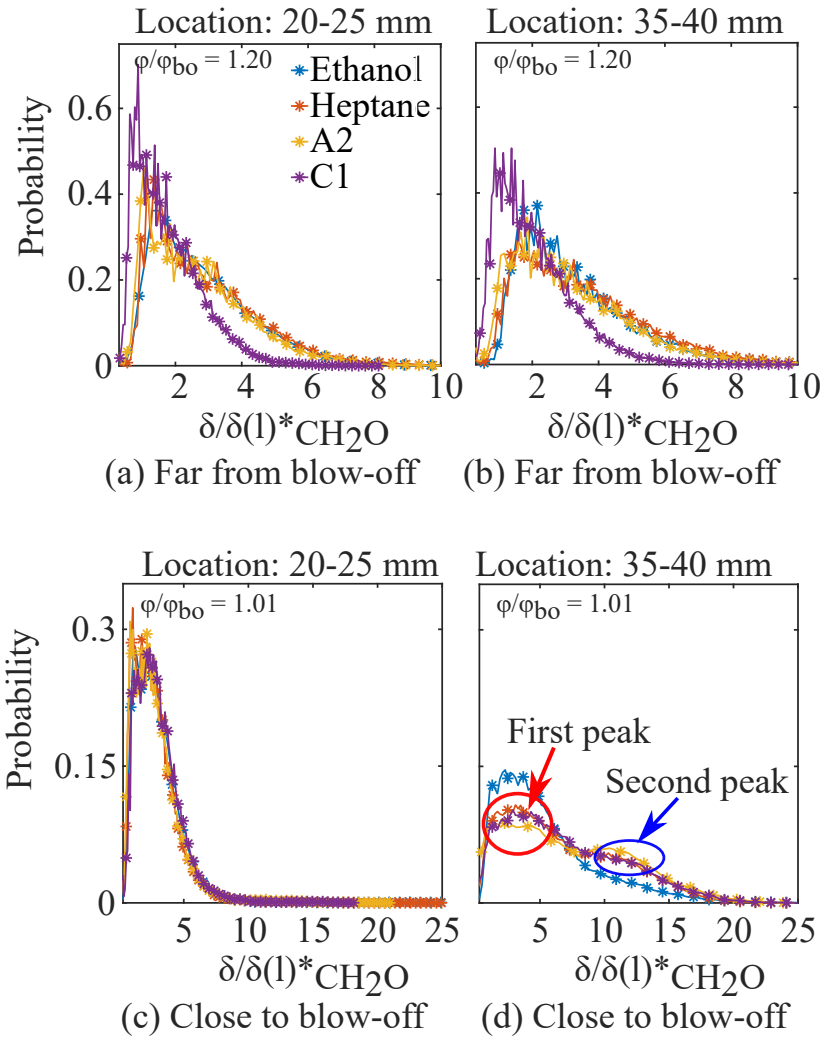

Fig. 6.14 Probability density function of CH_2O thickness at U_b = 23±1.5 m/s.

the local OH layer. The absence of OH leads to survival of the CH_2O and hence the larger CH_2O-regions observed.

The average and standard deviation of the CH_2O-layer thickness for all flames are presented in Table 6.1. At stable burning conditions, the mean and standard deviation of the CH_2O-layer thickness values were similar for the ethanol, heptane, and A2 flames, but were consistently lower for the C1-fueled flames. Regardless of the fuel used, an overall increase in the mean value of CH_2O-layer thicknesses was observed (i) as we go downstream, and (ii) as the flame approaches blow-off. Further, (iii) ethanol consistently has broader CH_2O layers compared to the other fuels, apart from the far-field location and close to blow-off, where it has the thinnest average CH_2O layer on average.

Table 6.1 Mean and standard deviation of CH_2O thickness at $U_bo = 23 \pm 1.5$ m/s at two location.

	$\phi/\phi_{BO} = 1.20$				$\phi/\phi_{BO} = 1.01$			
	20-25 mm		30-35 mm		20-25 mm		30-35 mm	
Fuel	Mean	Std	Mean	Std	Mean	Std	Mean	Std
Ethanol	3.25	2.29	3.50	2.25	3.36	3.22	5.68	3.92
Heptane	2.96	1.64	3.68	2.24	2.87	2.04	6.98	4.42
A2	2.70	1.50	3.18	1.82	2.92	2.03	7.65	4.82
C1	1.78	1.01	2.05	1.17	3.12	1.86	7.18	4.52

6.9 Velocity field

Velocity measurements were performed using Particle image velocimetry (PIV) in non-reacting and reacting conditions. In reacting condition heptane flame was investigated at condition far from and close to blow-off. Figure 6.15 shows the normalised mean axial ($\langle u \rangle / U_b$), and radial velocity ($\langle v \rangle / U_b$) obtained by averaging 1000 images with streamlines superimposed on $\langle u \rangle / U_b$ for non-reacting flow and the heptane flame.

The normalised RMS of axial (u_{rms}/U_b) and radial (v_{rms}/U_b) velocity fluctuations are also presented in Fig. 6.15. The magenta line in Fig. 6.15 (left column) marks the boundary of the RZ, which is defined by the location were $\langle u \rangle = 0$. The height of the RZ is ≈ 1.3 d in the non-reacting flow. For both reacting conditions, the height of the RZ is ≈ 2.4d, which is the maximum FOV of the present measurements. A similar increase in length of RZ was observed in the LES of Massery el al. [143]. Comparisons between the two reacting conditions indicate that the axial and radial velocity components do not significantly change as blow-off is approached. Under non-reacting conditions, u_{rms}/U_b was uniform within the RZ up to a distance of $0.4d$ from the burner. In contrast, under reacting conditions, u_{rms}/U_b was approximately constant up to a height of $0.8d$. Further downstream u_{rms}/U_b was observed to increase in the radial direction from a minimum value along the centerline of the burner and then peaks within the shear layer in both non- and reacting flows. Additionally, a drop in the axial velocity fluctuation was noticed in the annular region in both non-reacting and reacting flow. The radial velocity fluctuation in the RZ is not observed to vary significantly in the axial direction. The normalised radial velocity fluctuation was found to increase gradually from 0.2 in the anchoring region to 0.3 in the downstream regions. Like the axial velocity fluctuations, the radial velocity fluctuations are also maximum in the shear layer.

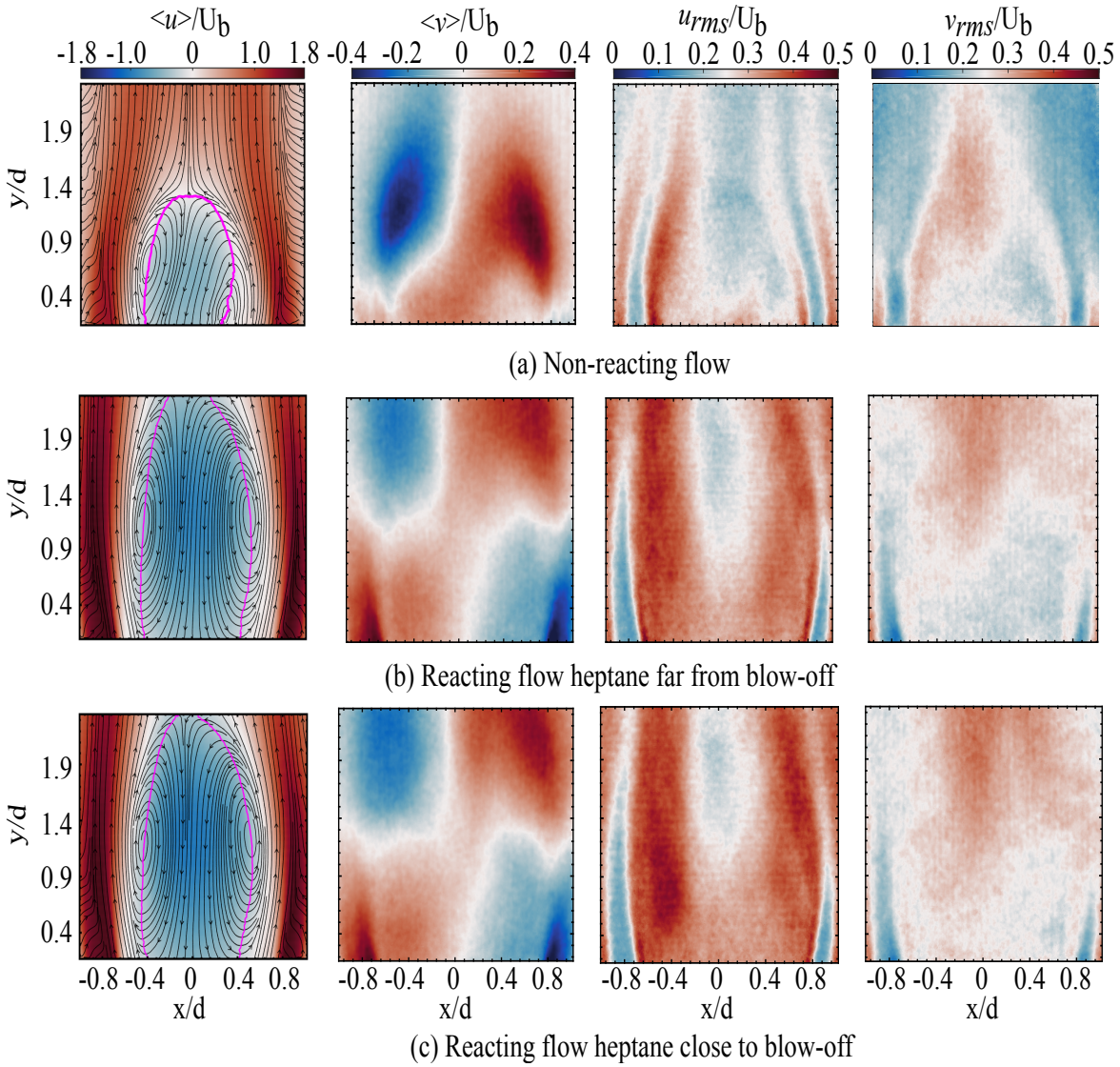

Fig. 6.15 Images of $\langle u \rangle / U_b$, $\langle v \rangle / U_b$, u_{rms}/U_b, v_{rms}/U_b in column from left to right. Row 1 represents the non-reacting flow. Row 2 and 3 shows the reacting flame with heptane at condition far from ($\phi/\phi_{bo} = 1.20$) and close to blow-off ($\phi/\phi_{bo} = 1.20$). x and y represent the radial and axial distance respectively. Magenta line in column 1 represents the boundary of the RZ, which is defined by the location were $\langle u \rangle = 0$.

Figure 6.16 presents the cross-section plots of normalised axial and radial velocities as well as rms of axial and radial velocity at a fixed height from the burner exit (y/d = 0.5, 1.0 and 1.5). The $\langle u \rangle / U_b$, and $\langle v \rangle / U_b$ were noticed to peaks within the shear layer, and their magnitude drops with height and in the RZ. Overall, both flow conditions, non-reacting, and reacting exhibit very similar velocity profiles. These results are echoed with the RMS of the radial and axial velocity fluctuations. Comparing the NRF and RF conditions, $\langle u \rangle / U_b$,

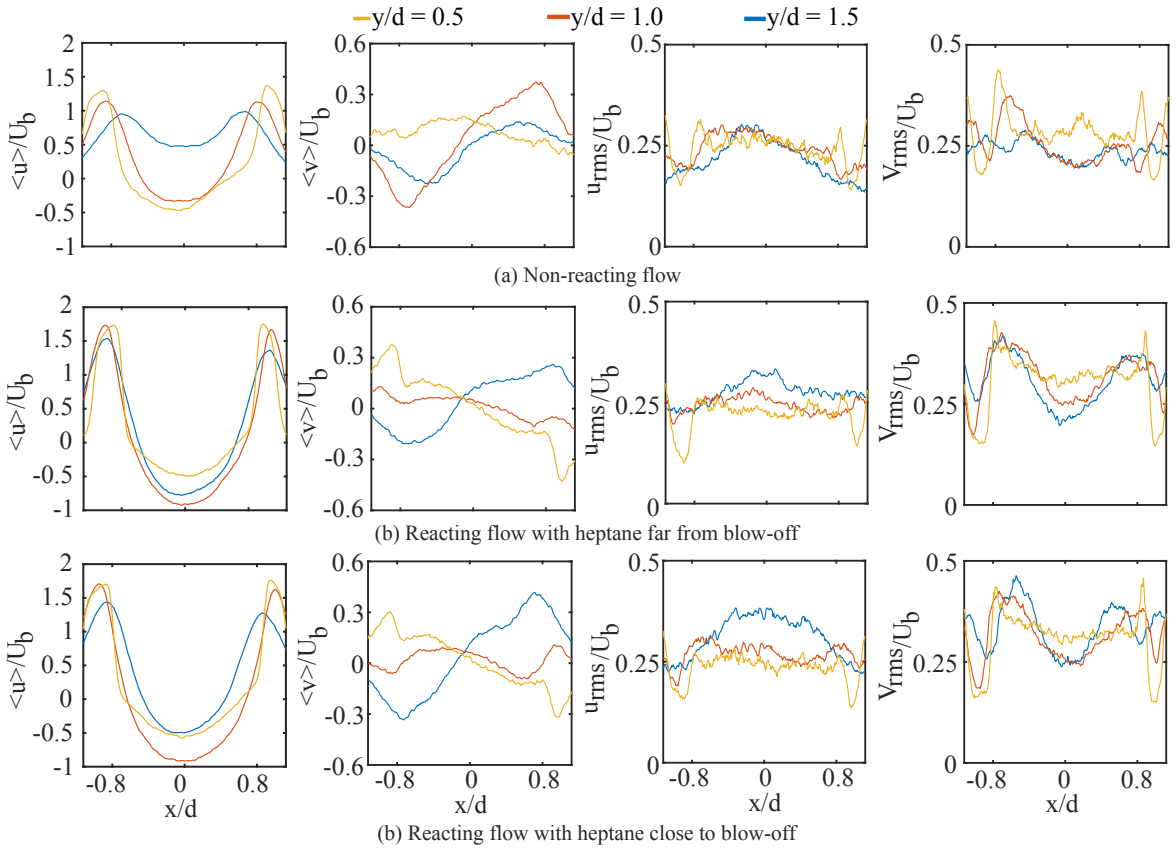

Fig. 6.16 Cross sections of $\langle v \rangle / U_b$, u_{rms}/U_b, and v_{rms}/U_b at y/d = 0.5, 1.0 and 1.5 in non-reactiing and reacting heptane flame.

and $\langle v \rangle / U_b$ is found to increase when the flame is present. Moreover, compared to the sable flames, $\langle u \rangle / U_b$ within the RZ increase as blow-off is approached. The increase in u'/U_B can be related to the rise in the local strain rate, leading to local extinction.

A spectral analysis was further performed on the velocity data. Power spectral densities (PSDs) were evaluated on the axial velocity fluctuations (u') at y/d = 0.5, 1.0, and 1.5 from the burner exit at six equally spaced points. PSD provides the distribution of the kinetic energy across the range of eddies present in the flow. All PSDs show a smooth decay towards small wave number (high frequency). The dashed black line in Fig. 6.17 represents the high-frequency decay at -5/3. As reported in a previous study in similar burner configuration Ref [29] no peaks were observed at any location with different cases. Reflecting non-presence of any dominant frequency, especially in the lower frequency range that might indicate the presence of instabilities in the flow.

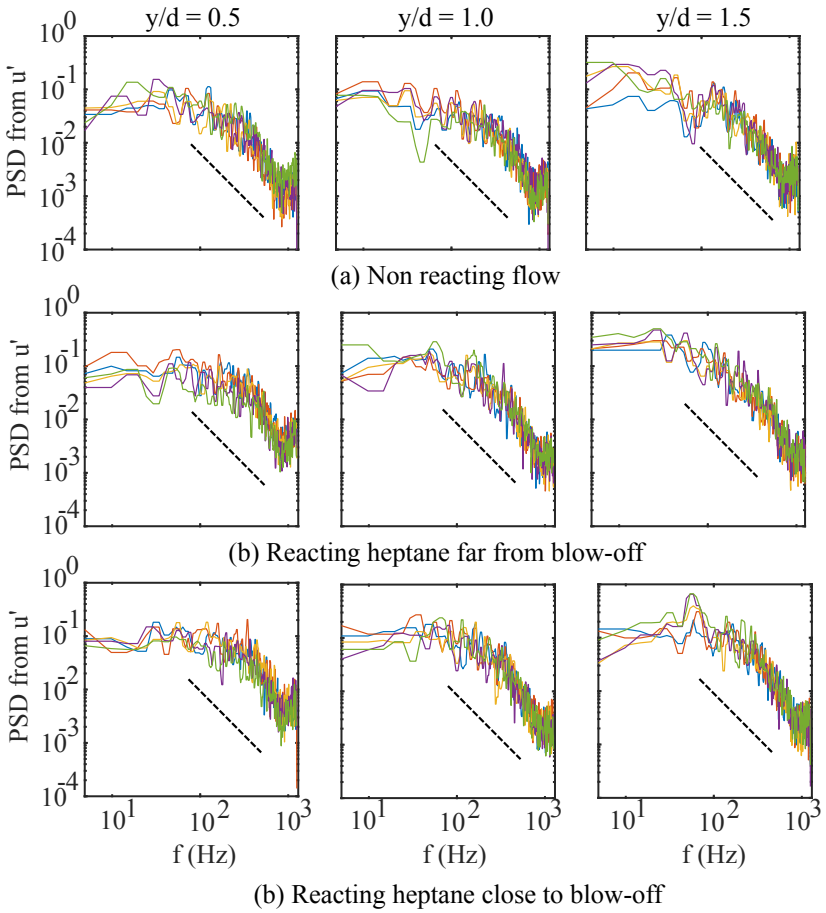

Fig. 6.17 PSDs of the non-reacting, reacting heptane (far from and close to blow-off) evaluated from the time series of axial velocity fluctuation (u'). The PSDs was performed at y/d = 0.5, 1.0 and 1.5 from the burner exit at six points equally spaced at each location. Where 'y' is the axial distance. The dashed line reflecting the -5/3 slope.

6.10 Turbulent length scale

The current flows have very inhomogeneous turbulence, and hence the integral length scale (L_T) is also expected to be direction-specific. To have a single value that can be used as a reference, L_T was determined following the same approach as in Ref. [29, 144], namely as the average of a characteristic turbulent length scale derived from 8 unique integral length scales derived from two-point correlation functions computed in eight separate lines from a given point. Four separate contours were identified based on the velocity data: maximum velocity ($|V|_{max}$), maximum shear based on the gradient of 2-D velocity field ($\bar{S}_{max}$), mid-profile between the maximum velocity and maximum shear ($mid-prof.$), and maximum velocity fluctuations (u'_{max}) (see Fig. 6.18a, 6.18b, and 6.18c). Where, $u'_{max} = max(u')$. Additionally,

$\bar{c}$ = 0.2 and 0.5 contours were obtained from the OH-PLIF and superimposed on the (u'/U_b). The (u'/U_b) images were cropped to have the same FOV as of OH-PLIF images (see Fig. 6.18d and 6.18e). The green dots in Fig. 6.18 mark the locations where the length scales were computed.

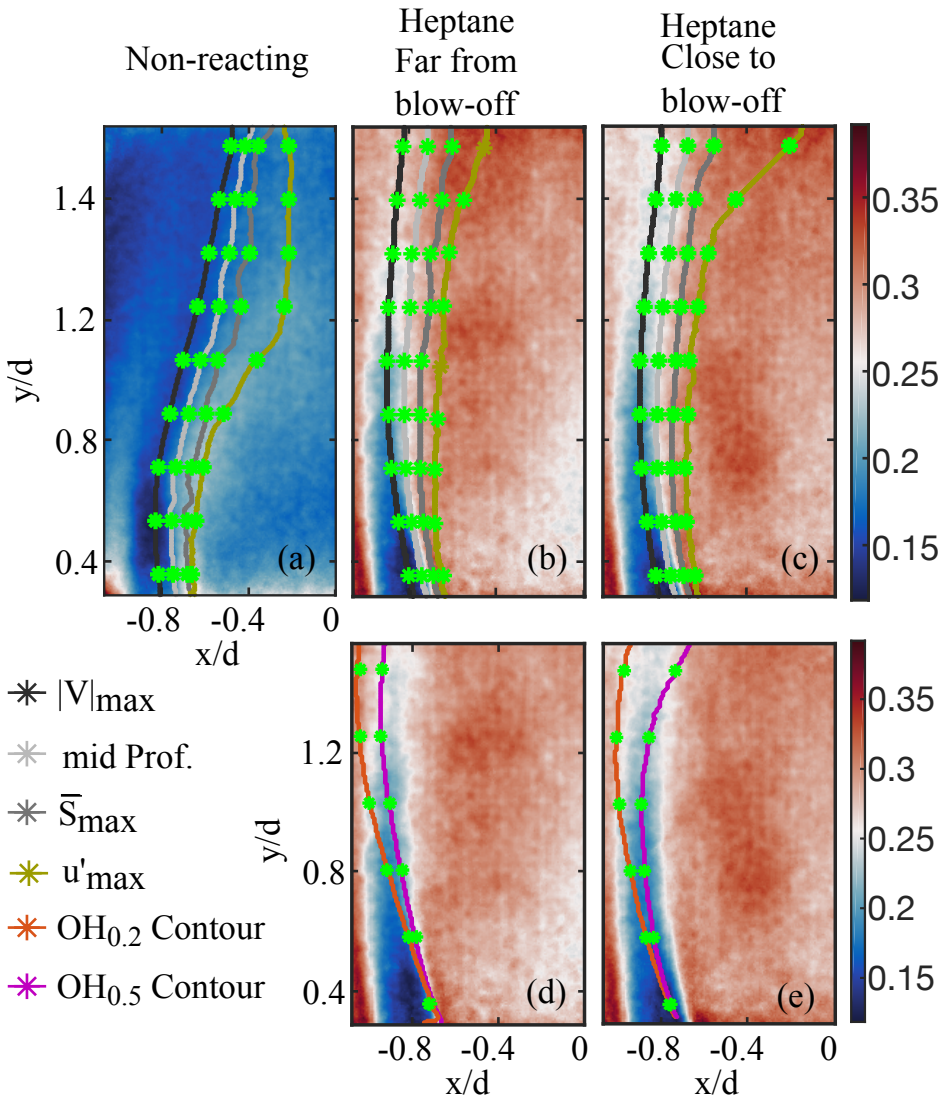

Fig. 6.18 Turbulent intensity (u'/U_b) top row superimposed by the contour of maximum velocity ($|V|_{max}$), maximum shear layer ($\bar{S}_{max}$), mid profile between the maximum velocity and maximum shear layer ($mid - prof.$), and maximum velocity fluctuations (u'_{max}). Bottom row represent with the $\bar{c}$ = 0.2 and 0.5 isolines from OH-PLIF images superimposed on (u'/U_b). Green marks on each represents the location at which the integral length scale (L_T) evaluated.

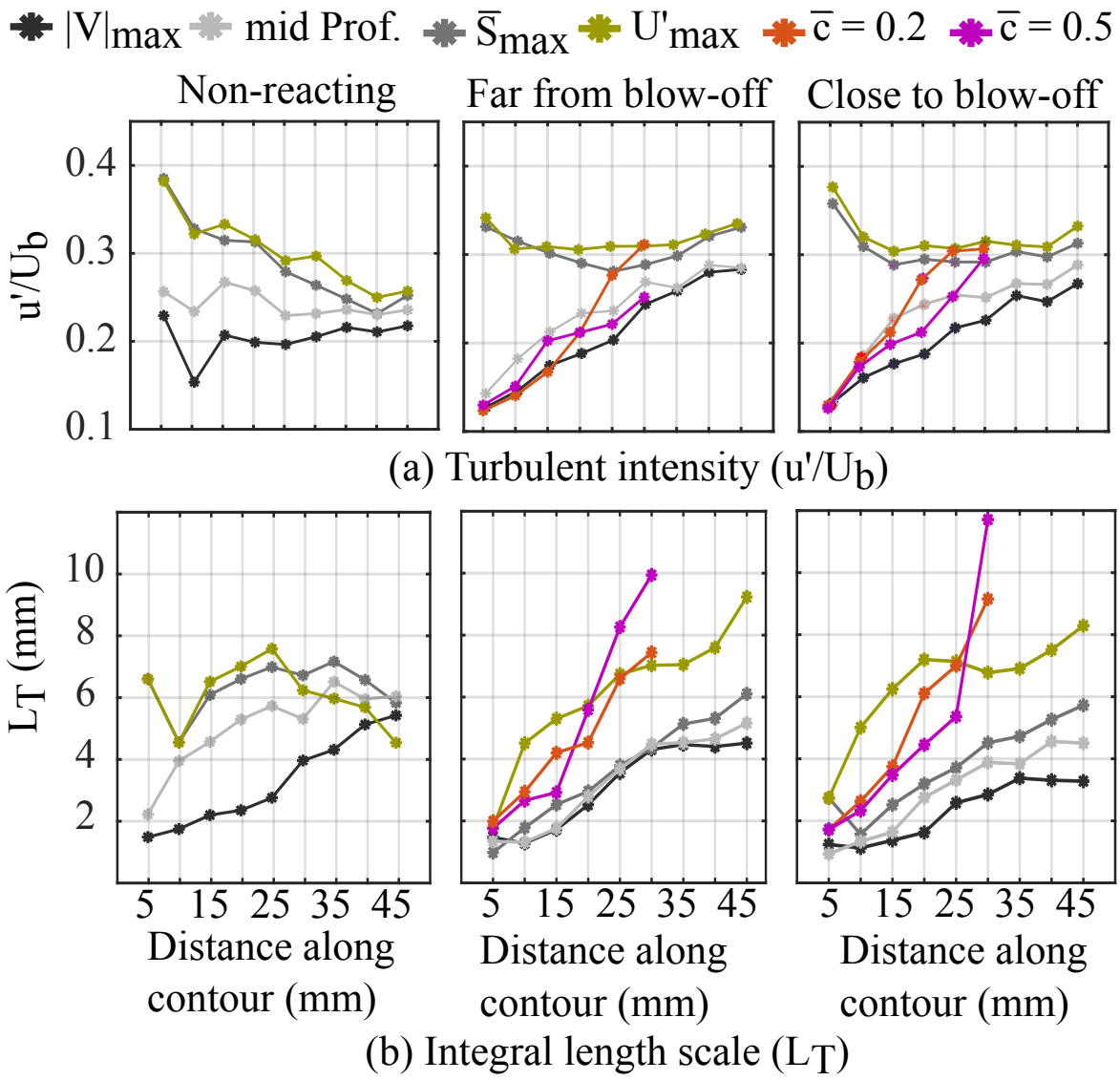

Fig. 6.19 Turbulent intensity (u'/U_b) and integral length scales evaluated along the six contours and locations shown in Fig. 6.18.

The value of L_T was estimated at nine locations along four contours based on velocity and at six locations along the $\bar{c}$ =0.2 and 0.5 isolines. Figure 6.19 presents the resulting u'/U_b and L_T values. In the non-reacting flow u'/U_b does not vary significantly along the $|V|_{max}$, and $mid-prof.$ lines. However, u'/U_b decreased along the $\bar{S}_{max}$ and u'_{max} contours. In the reacting flow, u'/U_b tended to increase along the $|V|_{max}$, $mid-prof.$, $\bar{c}$ =0.2 and 0.5 profiles, while it did not change much along the $\bar{S}_{max}$ and u'_{max} contours. The bottom row of Fig. 6.19 presents L_T in the non-reacting and reacting flow. It is evident that under non-reacting conditions L_T increases the $|V|_{max}$ contour up to 25 mm, thereafter it begins to

decrease along the $\bar{S}_{max}$, $mid-prof.$ and u'_{max}. Yet, in the reacting flow, L_T was observed to increase along all six contours. Values of L_T are comparable for conditions far from and close to blow-off and falls in the range of 2 - 11 mm at different locations of the flame. Additionally, values of u'/U_b and L_T obtained here were comparable with those reported by Kariuki et al. [29], who employed a similar bluff-body burner.

Figure 6.19 shows that the (u'/U_b) and L_T vary widely from the non-reacting to reacting conditions. Based on the location of the contours in the reacting condition the profiles of $|V|_{max}$, $mid-prof.$, $\bar{c}$ =0.2 and 0.5 were used to obtain local Ka values. To account for the changes in the flow structure induced by the flame, (u'/U_b) and L_T from reacting conditions were used to calculate Ka. Figure 6.20a and 6.20b show the variation of Ka along the four contours at far from and close to blow-off, respectively. Under conditions far from blow-off, Ka was observed to increase in the downstream regions of the flame. The Ka increased by a factor of two in the downstream region compared to the anchoring region and have a maximum value of ≈ 20 in the downstream region. Note, because values of S_L and δ_L are similar for the different fuels, Ka is approximately the same for each fuel considered here.

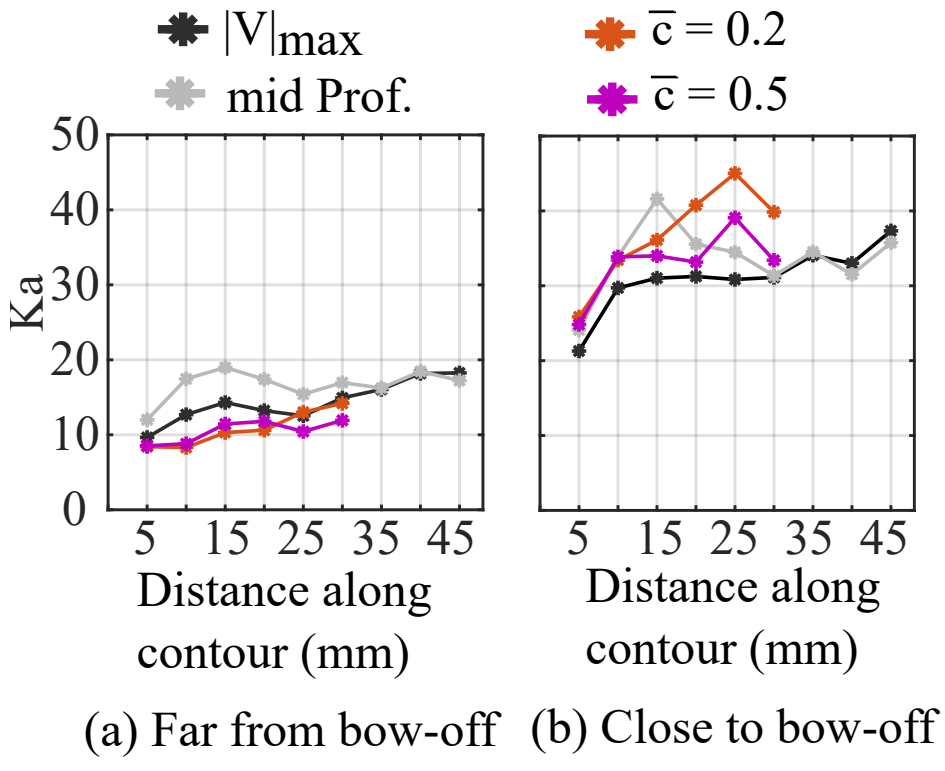

Fig. 6.20 Plots of Ka evaluated at location shown in Fig. 6.18 using the u' and L_T for non-reacting flow at condition far from and close to blow-off.

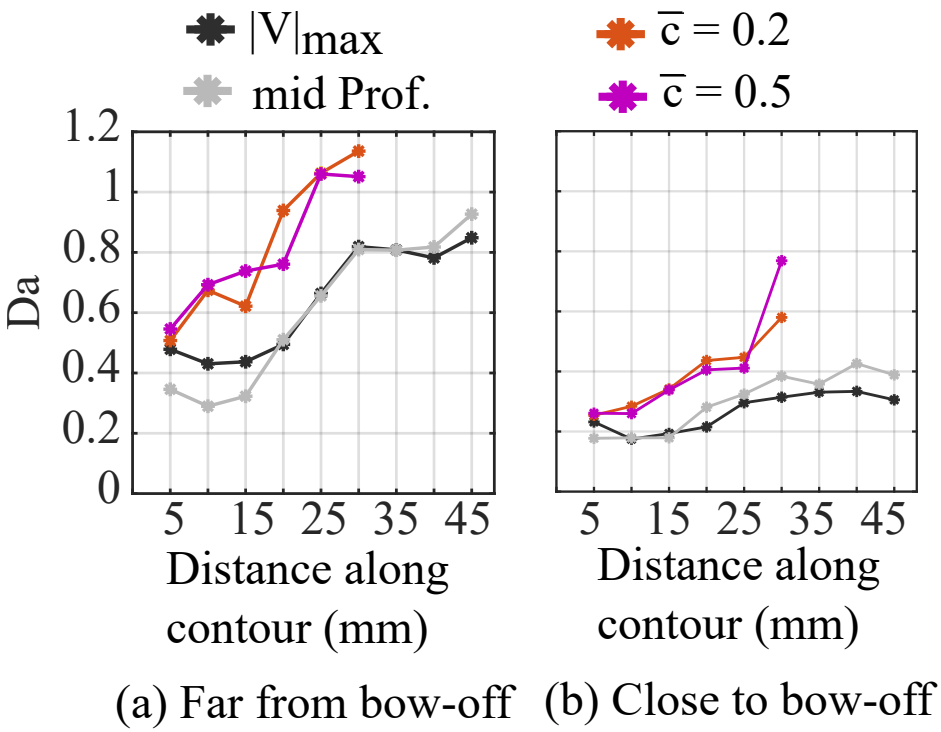

Fig. 6.21 Plots of *Da* evaluated at location shown in Fig. 12 using the u' and L_T for non-reacting flow at condition far from and close to blow-off.

As the flames approached blow-off, *Ka* increased by a factor of two achieving a maximum value of ≈ 41 (see Fig. 6.20b) in the downstream regions of the flame. A similar increase in *Ka* was observed in Ref. [29] as their flames approached blow-off. The increase in *Ka* as the flame approaches blow-off is a consequence of the lower S_L values. Similar to conditions far from blow-off, those near blow-off showed an increasing trend of *Ka* in the downstream regions. Suggesting flames experiences more stretch in the downstream regions, which leads to a higher probability for the occurrence of local extinction within such regions (see Fig. 6.6). Figure 6.21 shows the variation *Da* along the four contours at far from and close to blow-off. At far from blow-off, *Da* exhibited an increasing trend along the axis. As expected, *Da*, was found to reduce as the flames approached blow-off and dropped by a factor of two. A similar decrease in *Da* was observed in Ref. [29] as their flames approached blow-off.

6.11 Discussion

From the preceding presentation of OH*, OH-PLIF, CH_2O-PLIF, and Fuel-PLIF images, the blow-off mechanism can be divided into four steps: (i) fragmentation of the flame in the downstream region; (ii) entry of CH_2O into the RZ, forming the first pockets void of

OH-PLIF signal; (iii) breaking of the flame-front in the shear layer; (iv) fuel entry into the RZ as shown in Fig. 5.4, which mixes with the CH_2O and offers the second reason for the absence of OH.

Considering the first step, the change in flame shape and closing of the flame in the downstream region of the RZ as LBO was approached is consistent with previous studies [32, 29, 36, 31]. The blow-off event begins with the shredding of flame in the downstream region because of local extinction. The fragmentation of the OH structures in this region may be due to localised extinction. PIV measurements made in a methane flame (i.e. Ref. [29]) showed that the *ka* increases with distance along the flame brush, and hence the opportunity for extinction is expected to increase with axial distance. The results are consistent with the time-averaged OH* chemiluminescence images (Fig. 5.1a), which show the presence of reactions in the RZ above the bluff-body and shortening of the flame as it approaches blow-off. They are also similar to those in Refs. [29, 36, 17], which were acquired from methane and ethylene flames. Simultaneous measurement of OH and PIV in Ref. [31] suggested that these localised extinctions are due to locally high strain rates induced along the flame when they exceed the corresponding extinction strain rate. However, this explanation is probably insufficient for CH_4 flames in the presence of back-support from adiabatic hot products [29, 36]. Hence, it seems more likely that a CH_4 flame would extinguish locally due to flame-flame merging and loss of this back-support. Indeed, results in Ref. [145] indicate that local extinctions of highly turbulent methane flames are primarily promoted by reduction in back support.

Considering Step (ii), as described in Refs. [29, 31], as LBO was approached the flames begin to experience a higher degree of incomplete combustion, which allows partially-burnt reactants (e.g. CH_2O as shown in Fig 5.3) to enter the RZ. Ultimately, the smaller volume of fully-burnt hot products inside the RZ weakens the back support of the flame at the shear layer and leads to Step (iii), i.e. to an increased level of localised extinction events, and to the penetration of cold reactants into the RZ (Step (iv); Fig. 5.4) until the flame is globally extinguished.

Note from Table 5.1 that the LBO of the kerosene flames occurs at a higher equivalence ratio compared to the other fuels. Kerosene has a $Le \approx 4.6$, in contrast to the smaller hydrocarbons that have lower *Le*. Strained counterflow laminar premixed flame calculations (not shown here) suggest that in the back-to-back configuration, kerosene flames extinguish at a lower strain rate compared to the other fuels, consistent with the present stability trend.

The blow-off behaviour observed here has some similarities, but also some differences to the one proposed by Refs. [78, 31] for a propane flame. It was suggested that local extinction occurs in the shear layer due to high strain rate, which leads to the entry of

cold reactants into the RZ. In contrast, the current study with A2 and previous studies with CH_4 [29, 36, 17] showed that the LBO mainly begins in the downstream region of the RZ where local extinction is driven by flame-flame merging (see Fig. 5.2 at 120, 110, 90, 70 ms) or localised flame extinction in the shear layer due to high stretch; this leads to the substantial flow of partially-burnt and unburnt reactants into the RZ from the downstream stagnation point, further destabilising the flame close to the bluff body. The discrepancies in the behaviour of blow-off in Refs. [78, 31] to those of the current study may be due to the burner configuration [23], which can alter the level of strain "felt" by the flame in the shear layer; this is a function not only of the incoming turbulence and shear rate, but also of the angle the flame makes with the flow.

A clear difference between the A2- and methane- flames is that the former exhibit a higher degree of CH_2O-layer broadening. Such broad layers in the former are likely to interact with OH and fresh reactants within the RZ of such flames (see Figs. 5.2, 5.3 and 5.4). This combination is likely to promote the influence of low-temperature chemistry in A2 flames, which likely contributes to their longer blow-off duration. In other words, the combination of low-temperature reactions with intermittent product pockets likely increases the longevity of these more complex-fueled flames.

As is apparent from the results above and those in Refs. [29, 31, 32, 36], as blow-off is approached there are pronounced differences in flame structure. The blow-off limit plot and the subsequent analysis in Chapter 4 demonstrated that lean blow-off of higher hydrocarbon fueled flames cannot be subsumed solely into parameters like S_L, even after considering the effect of Le or strain rate, which is consistent with findings in Refs. [38, 39].

The data presented in this paper indicates that Σ_{2D}, κ, and $S_{T,LC}/S_L$, exhibit little to no dependence on fuel type. These quantities are strongly related to the level of wrinkling experienced by the flame and this suggests that the flames considered here exhibit similar degrees of wrinkling. However, since the Le of the separate fuels is quite different, this is unexpected. For example, results from a recent DNS [40] imply that higher $Le > 1$ dampens the wrinkling of the flame. Yet here the A2 flame, which has higher Le than ethanol and heptane, showed large κ. The reason for this is unclear, it may be due to the higher molecular complexity of A2, or its apparent higher propensity for extinction. Pinpointing the cause of this difference should be the subject of future work.

A classic tool often invoked to predict the structure of turbulent premixed flames is the theoretical regime diagram [52, 135]. This diagram is presented in Fig. 6.22a and its $y-$ and $x-$axis represent u'/S_L and L/δ_L, respectively. The critical boundaries in this diagram are marked by $Ka = 1$ and 100. The former is theoretically intended to delineate thin wrinkled flames from those with thin reactions yet broadened preheat layers, while the latter boundary

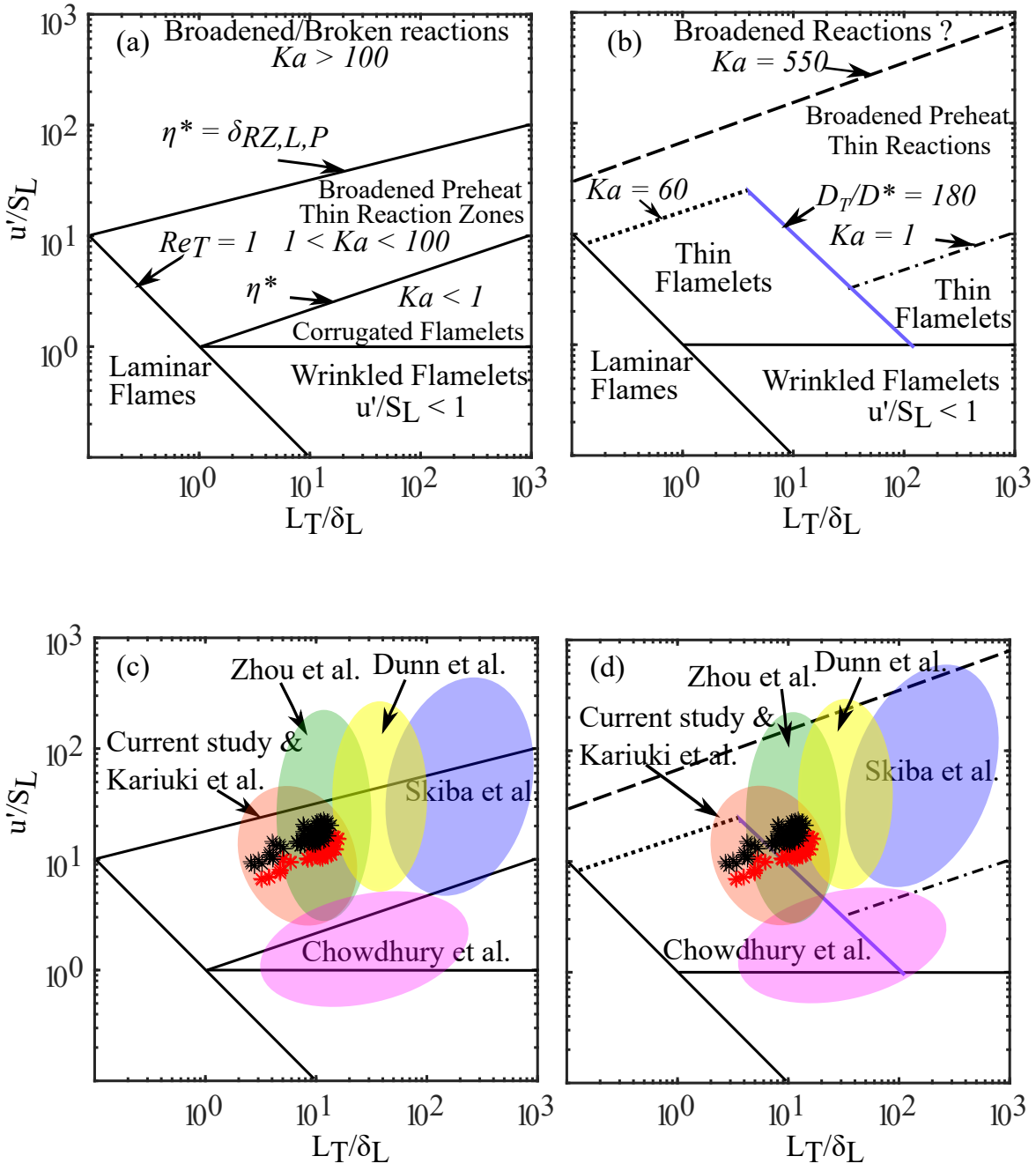

Fig. 6.22 (a) Theoretical regime diagram adapted from [52]. (b) The new modified regime diagram proposed by Skiba et al. [50]. (c) The same diagram including the points from previous [17, 29, 30, 46 - 51] and current study. (d) The new modified regime diagram with points from previous and current study. Red and black markers are far from and close to blow-off cases, respectively.

is meant to mark a transition to either broken or distributed burning [52, 135]. More recently, Skiba et al. [50] modified these boundaries based on a large compilation of experimental and numerical results. Figure 6.22b presents this modified (or measured) regime diagram, where the biggest difference is in the boundary defined to separate thin flamelets from those with broadened preheat layers.

The main utility of the regime diagram is to facilitate comparisons between results from separate studies and between such results and those proposed by theories. The present results were incorporated into the regime diagram based on the L_T and u' values estimated from the reacting velocity field measurements. As expected, the current conditions occupy a similar region of the regime diagram as those in Ref. [17, 29], which are broadly marked by the red ellipse in Figs. 6.22c and 6.22d. Additionally, for comparison, regions occupied by the conditions considered in the studies of Skiba et al. [50], Zhou et al. [47–49], Dunn et al. [46, 51], and Chowdhury et al. [30], are marked by the purple, green, yellow and pink ellipses, respectively.

Since these flames fall in the same region of the regime diagram, one should expect them to have similar structural features. Based on the location of the present cases in Fig. 6.22, it is expected for them to exhibit broadened preheat layers. Indeed, cases from other studies lying in the vicinity of those considered here observed broadened preheat (or CH_2O) layers. Namely, in Refs. [17, 30, 47–50, 146] CH_2O-layers were observed to broaden with increased u'/S_L^0. In a similar burner configuration, Kariuki et al. [29] showed that u'/S_L increases in the downstream region. The increase in u'/S_L with axial distance is one potential reason for the increased broadening with axial distance. However, note that Bunsen and jet flames (e.g., those in Refs. [146, 46, 47]) also exhibit CH_2O-layer broadening with axial distance even though their u'/S_L values tend to decrease in this direction. Thus, increased u'/S_L may not be the only reason for such CH_2O-layer broadening. As in the current study, heptane and kerosene fueled flames showed broad regions of CH_2O-layer than the ethanol flames, even when u'/S_L and L_T/δ_L is roughly the same for the separate flames.

As noted, CH_2O-layer broadening is associated with flames close-to and experiencing lean blow-off. As mentioned above the first step in blow-off is the shredding of the flame in the downstream region due to localised extinction. The PIV measurements presented above showed that local Ka number increases in the downstream, which makes the flame more susceptible to local extinction in the downstream regions, consistent with the increase in the CH_2O-layer width. The broad regions of CH_2O observed within the RZ (see Fig. 6.13), is likely a consequence of convection. Namely, local extinction in the downstream region as a result of flame-flame merging appears to lead to a build-up of CH_2O (i.e. the CH_2O-layers on opposite sides of the Burner are seen to merge in the downstream region in Fig. 6.13),

which is then likely convected into the RZ by the recirculating flow. Additionally, Fuel-PLIF imaging showed that the Fuel-PLIF signal is uniform and continuous in the annular region with very little entrainment of the ambient air. Fig. 6.13 suggests that the kerosene and heptane flames tend to exhibit broader regions of CH_2O within the RZ than the ethanol flames, even though their u'/S_L and L_T/δ_L values are roughly the same. This suggests that subtleties in the chemistry of the various fuels may also be influencing the propensity of the flames to exhibit broadened preheat layers. The DNS study of Aspden et al. [147] indicated that the CH_2O layer thickness might depend on fuel type. They showed that dodecane decomposes at low temperatures, which leads to the formation of unstable species such as pC_4H_9 and nC_3H_7. Subsequently, these species combine to form CH_2O, which is a stable molecule that, if prevented from reacting with other species like OH and H-atoms, can be transported to low-temperature regions of the flame. While DNS results merely represent a model of reality, they do provide detailed insights into the chemistry that cannot be measured directly. Therefore, in light of such DNS results and those presented in this study, the large regions of CH_2O present in the kerosene and heptane flames are likely the consequence of interactions of large scale eddies with chemistry that facilitates the transport of CH_2O to what are expected to be lower-temperature regions. Moreover, such broadening plays a role in dictating the blow-off event. Namely, as explored in Refs. [29], entrainment of unburnt species like CH_2O into the RZ can lead to further destabilisation of the flame if it mixes with and subsequently quenches the primary flame-front in the shear layer.

The results presented above corroborated by the CH_2O- and OH-PLIF images demonstrates that different fueled flames occupying the same region of regime diagram can exhibit different structural features. This finding is consistent with those in prior studies [29, 40, 38, 147] and indicates that caution should be expressed when utilizing simplified tools like the regime diagram to forecast the structure of flames produced with complex fuels.

The present data on flame location as a function of operating condition and approach to global blow-off, on FSD, and the width of CH_2O regions can be useful for modelling studies. Typical efforts for turbulent premixed flames include pre-tabulated approaches [8–10] and on-line solution of the chemical structures [11–14]. Both approaches could benefit from the present experimental data.

6.12 Summary

The structure of turbulent unconfined bluff-body flames of vapourised liquid fuels was investigated at two conditions: far from blow-off ($\phi/\phi_{BO} = 1.20$) and close to blow-off ($\phi/\phi_{BO} = 1.01$). Four different fuels were considered, two of which comprised of a single

component (ethanol and heptane) while the other two were multi-component kerosene blends (A2 and C1 from the National Jet Fuel Combustion Programme). The flame structure was studied with 5 kHz OH* chemiluminescence and OH-PLIF imaging. Additionally, 10 Hz CH_2O-PLIF imaging was used to study the impact of fuel composition on the CH_2O-layer. Averaged OH*chemiluminescence images are qualitatively similar for all four fuels at both conditions. Also, the flame brush was observed to be closing from the downstream end of the recirculation zone for all four flames at close to blow-off. The OH-PLIF images of ethanol flames far from blow-off display a high OH-LIF signal intensity along with the shear layer. In contrast, the OH-LIF signal was evenly distributed throughout the heptane and kerosene flames throughout the recirculation zone (RZ). Regardless of the fuel used, close to blow-off the flame becomes shorter with peak OH-LIF signal intensities lying inside the RZ. All four fuels showed a decrease in flame surface density (Σ_{2D}) and broadening of the 2-D curvature PDFs as their blow-off limits were approached. An increase in local turbulent consumption speed was observed in the downstream region as the flames approached blow-off. No significant variation in Σ_{2D}, curvature PDF, and local turbulent consumption speed was observed between the different fuel types. The average CH_2O-layer thickness was larger than the computed laminar flame value by a factor of two and six for conditions far from and close to blow-off, respectively. Moreover, heptane and kerosene flames showed more pockets of CH_2O-LIF signal within the RZ compared to ethanol, suggesting that considerably more partially-combusted fluid enters the RZ of the former than the latter. High-speed particle image velocimetry was performed to measure the local velocity fields. However, the fact that the fuel type results in differences in some structural features near blow-off suggests that flames produced with heavy hydrocarbon fuels involve chemistry effects at blow-off that are not fully characterized by laminar flame properties.

The non-reacting and reacting flow velocity data is reported in this chapter. Reacting conditions were conducted with heptane at two equivalence ratios (far from and close to blow-off). The height of the RZ was observed to increase in the reacting flow compared to a non-reacting flow case. The RZ was $\approx 1.3d$ in NRF and was $\approx 2.3d$ in reacting flow. As the blow-off approached, a rise in axial velocity fluctuations was observed. Turbulent length scales L_T in non-reacting conditions increases along the $|V|_{max}$ contour. Along the $\bar{S}_{max}$, $mid-prof.$ and u'_{max}, it was observed it increases up to a height of 25 mm, then decreases. In the reacting flow, L_T was observed to increase along all six contours. The L_T along the contour of $|V|_{max}$ and $mid-prof.$ from the non-reacting condition were used to obtain the local Ka and Da. It was observed that the Ka increase and Da decreases as the blow-off was approached.

Chapter 7

Final remark

This chapter presents the conclusions drawn from Chapters 4, 5, 6, and 7, and recommendations are provided for future work.

7.1 Conclusion

This dissertation examines the effect of fuel properties on the blow-off limits and flame shape for vaporised ethanol, heptane, and two different kerosene fuels. Kerosene fuels were comprised of a conventional Jet-A blend (A2) and an alternative Gevo ATJ blend (C1). The flame structure and blow-off duration of unconfined premixed vapourized fuel on a bluff-body burner were studied using OH* chemiluminescence, OH-, CH_2O- and Fuel-PLIF imaging.

7.1.1 Lean blow-off limits and scaling

In this chapter, the lean blow-off limits (LBO) for ethanol, heptane, and two kerosenes (A2 and C1) are discussed, and the results are compared to the methane flame. The results were evaluated with a *Da* correlation based on laminar flame speed proposed by Radhakrishnan et al. [61]. The findings are summarized below:

1. It was observed that the methane, ethanol and heptane flames are more resilient to blow-off than the kerosene flames (i.e., A2 and C1).

2. The stability limits were evaluated using a correlation based on a characteristic Damköhler number (*Da*). The correlation was not successful in collapsing the stability points associated with liquid-fueled flames to the line derived for methane flames. This suggests that correlations wherein the combustion chemistry is solely subsumed within the laminar flame speed (i.e. that based on a characteristic *Da*) is not likely to be universally applicable.

7.1.2 Blow-off duration and mechanism

In this Chapter the blow-off mechanism and blow-off duration is discussed. The blow-off duration was calculated with all four vaporised fuels and compared with the methane blow-off duration. The lean blow-off mechanism was studied with A2 flame and was divided into four steps. The details of each blow-off step are discussed above in the discussion section of this chapter. The conclusions in this chapter were made based on 10 independent blow-off events. The major findings are:

1. The duration of a LBO event was 2.5 times longer in the kerosene flame than in methane. This was also true for heptane and an alternative kerosene (C1). This long duration and the presence of large regions of CH_2O inside the RZ of more complex-fueled flames suggests the possibility of significant low-temperature reactions

occurring in the RZ during LBO. This indicates that LBO knowledge based on CH_4 can not be fully transposed to heavier hydrocarbon fuels that are ubiquitous in practice.

2. The OH* chemiluminescence, OH-, CH_2O- and Fuel-PLIF images, suggested that the flame is typically extinguished first in the downstream region (i.e. near the stagnation point above the bluff body). From there, CH_2O penetrates the RZ from there, which destabilise the shear layer flame, enabling a relatively long process where the flame is progressively eliminated and the RZ filled with CH_2O and fresh reactants. CH_2O regions were found to be much larger in kerosene (A2) as opposed to methane flames.

7.1.3 Spatial flame structure

In this chapter, we examined the impact of fuel type on the structure of turbulent premixed flames stabilized by a bluff-body burner. Four vapourised fuels were considered: ethanol, heptane, and two kerosene fuels (A2 and C1). The measurements were made at conditions close to and far from lean blow-off. OH* chemiluminescence, OH-PLIF imaging and 10 Hz CH2O-PLIF imaging were performed. The major findings of this study are:

1. OH* images showed that all four liquid fuels exhibit a similar flame shape at stable burning conditions. Close to blow-off, the flames become shorter with reaction zones lying inside the RZ. Moreover, the flame fronts from either side of the burner bent towards the axis and merged in the downstream region of the RZ.

2. The OH-PLIF images showed that all four liquid fuels exhibit similar flame structure and dynamics under stable burning conditions. Close to blow-off, the flames become shorter with peak OH-LIF signals lying inside the RZ. Pockets void of OH-LIF signal were also found within the RZ. These pockets result from entrainment of partially preheat/reacted or unburnt reactants into the RZ from the downstream regions of the flame.

3. A decrease in the peak 2-D FSD values with increasing u'/S_L was observed. However, the 2-D FSD values were approximately the same for all fuels considered. Since the separate fuels each possess different lean blow-off limits, 2-D FSD is not a reliable indicator of the onset of blow-off for the flame studied here. The broadening of curvature was observed as the flame approached blow-off, suggesting flames become more wrinkled with decreasing equivalence ratio. The local turbulent consumption speed increased in the downstream region as the flame approaches blow-off. However, the local turbulent consumption speed displayed no noticeable dependency on fuel type.

4. Close to blow-off, an increase in CH_2O-layer thickness was observed in all four flames. This observation was corroborated by the fact that PDFs of CH_2O-layer thickness broadened as the conditions approached lean blow-off. Furthermore, heptane, A2, and C1 displayed double peaks in their CH_2O-layer thickness PDFs when close to blow-off. This dual peak behaviour is likely linked to the increased probability of observing CH_2O-LIF signal within the RZ. Such occurrences may be a consequence of the heavy hydrocarbon flames experiencing incomplete combustion and the presence of pronounced low-temperature chemical reactions inside the RZ compared to unity *Le* flames such as methane.

5. Velocity measurements allowed the conditions to be considered in the context of the regime diagram. The cases fall within the same regime, yet display different structural features. Thus, simplistic scaling arguments based on laminar flame properties are insufficient to predict the nature of more complex fueled flames.

These measurements are useful for increasing our understanding of fuel composition effects on the structure and behaviour of lean turbulent premixed flames and highlight the fact that knowledge derived from flames produced with simpler fuels (e.g., methane) can not be transposed in a fully quantitative sense when considering the extinction of flames produced with heavy hydrocarbon fuels.

7.2 Future work

The work reports the unconfined bluff body flame structure with vapourised kerosene fuel at conditions far from and close to blow-off. The present data on flame location as a function of operating condition and approach to global blow-off, on FSD, and the width of CH_2O regions can be useful for modeling studies. Typical efforts for turbulent premixed flames include pre-tabulated approaches [8–10] and on-line solution of the chemical structures [11–14]. Both approaches could benefit from the present experimental data.

This dissertation discusses the blow-off limits, key stages of the blow-off mechanism, and blow-off duration with a kerosene-fueled flame. As the blow-off approached, the flame became shorter, and the reaction zone migrated from the shear layer into the recirculation zone. From the OH* chemiluminescence, OH-, CH_2O- and Fuel-PLIF images, it can be deduced that the flame typically extinguishes in the downstream regions, leading to the entry of CH_2O into the recirculation zone, destabilising the flame. The kerosene flame showed a broad region of CH_2O during blow-off in the recirculation zone. Also, blow-off duration quantification with different fuels raises some questions as the blow-off duration is 2.5 times

longer in kerosene than in methane flame. This long duration and broad regions of CH_2O may be due to the dominance of low-temperature chemical reactions in kerosene fuels. This research has also found that kerosene blows off more easily than methane. Understanding this and how this occurs in different burner geometry and flow conditions such as swirl is important. This will improve our understanding of flame behavior during blow-off in a realistic combustor geometry.

It was attempted to correlate the onset of blow-off with terms like S_L,$K \times Le$, or S_{lam}; however, such efforts failed to collapse the LBO data across the range of fuels studied here. This implies that the extrapolation of knowledge from flames of small hydrocarbons (e.g., methane, ethylene) to higher hydrocarbons (e.g., heptane, kerosenes) can not simply be based on concepts where all the combustion chemistry is expressed through S_L, even after considering Le or strain effects. A more detailed numerical and experimental study is required before a universal correlation can be proposed that incorporates the effects of low-temperature fuel chemistry, Le, or S_{lam}.

In this study, it was concluded that extinction in the downstream regions of the flame played a crucial role in triggering blow-off. It was determined from the velocity data that the local high Ka number is responsible for the extinction events that occur downstream. Furthermore, the width and height of the recirculation zone changed in reacting flow compared to non-reacting flow. As observed by Ref. [143], the velocity measurements performed in this study were critical to CFD model validity. The OH-PLIF results reported here have been treated very carefully to quantify the local extinction events, as it may be due to an out-of-plane motion. In order to reduce these uncertainties in measurements, simultaneous OH- and CH_2O-PLIF as well as simultaneous Fuel-PLIF and CH_2O-PLIF is required. The simultaneous measurements can help us to understand the blow-off mechanism's key stage. Simultaneous measurements are expected to provide valuable insight into how the reaction zones change close to and during blow-off. In addition, Ka and Da numbers were estimated from PIV data, and the locations of these points were estimated using the OH-PLIF images, which were not acquired simultaneously. It would be nice to determine Ka and Da at the flame front using simultaneous OH-PLIF and PIV measurements, so that a correlation can be derived between local extinction and Ka and Da.

References

[1] R. Cheng, H. Levinsky, 6 - lean premixed burners, D. Dunn-Rankin, P. Therkelsen (Eds.), Lean Combustion (Second Edition), Academic Press, Boston, second edition edition, 2016, pp. 203 – 229.

[2] Y. Liu, X. Sun, V. Sethi, D. Nalianda, Y.-G. Li, L. Wang, Review of modern low emissions combustion technologies for aero aas turbine engines, Prog. Aerosp. Sci. 94 (2017) 12 – 45.

[3] A. H. Lefebvre, Fuel Effects on Gas Turbine Combustion, Int. J. Heat Fluid Flow 5 (4) (1983) 183.

[4] S. M. Correa, A review of nox formation under gas-turbine combustion conditions, Combust. Sci. Technol. 87 (1-6) (1993) 329–362.

[5] T. Echekki, E. Mastorakos, Turbulent Combustion Modeling: Advances, New Trends and Perspectives, Fluid Mechanics and Its Applications, Springer Netherlands, 2010.

[6] A. T. Brimmo, G. Ospina, M. I. Hassan, Conically stabilized turbulent premixed lean-flames sustainability, Energy Procedia 142 (2017) 3820 – 3826. Proceedings of the 9th International Conference on Applied Energy.

[7] I. Glassman, R. Yetter, N. Glumac, Combustion: Fifth Edition, 2014.

[8] J. F. Driscoll, Turbulent premixed combustion: Flamelet structure and its effect on turbulent burning velocities, Prog. Energy Combust. Sci. 34 (1) (2008) 91 – 134.

[9] J. C. Massey, I. Langella, N. Swaminathan, Large Eddy Simulation of a Bluff Body Stabilised Premixed Flame Using Flamelets, Flow, Turbul. Combust. 101 (4) (2018) 973–992.

[10] R. Mercier, C. Mehl, B. Fiorina, V. Moureau, Filtered wrinkled flamelets model for large-eddy simulation of turbulent premixed combustion, Combust. Flame 205 (2019) 93 – 108.

[11] D. Farrace, K. Chung, S. S. Pandurangi, Y. M. Wright, K. Boulouchos, N. Swaminathan, Unstructured les-cmc modelling of turbulent premixed bluff body flames close to blow-off, Proc. Combust. Inst. 36 (2) (2017) 1977 – 1985.

[12] E. Hodzic, E. Alenius, C. Duwig, R. S. Szasz, L. Fuchs, A large eddy simulation study of bluff body flame dynamics approaching blow-off, Combust. Sci. Technol. 189 (7) (2017) 1107–1137.

[13] E. Hodzic, M. Jangi, R.-Z. Szasz, X.-S. Bai, Large eddy simulation of bluff body flames close to blow-off using an eulerian stochastic field method, Combust. Flame 181 (2017) 1 – 15.

[14] L. Esclapez, P. C. Ma, E. Mayhew, R. Xu, S. Stouffer, T. Lee, H. Wang, M. Ihme, Fuel effects on lean blow-out in a realistic gas turbine combustor, Combust. Flame 181 (2017) 82 – 99.

[15] R. Sankaran, E. R. Hawkes, J. H. Chen, T. Lu, C. K. Law, Structure of a spatially developing turbulent lean methane–air bunsen flame, Proc. Combust. Inst. 31 (1) (2007) 1291 – 1298.

[16] J. Kariuki, J. R. Dawson, E. Mastorakos, Measurements in turbulent premixed bluff body flames close to blow-off, Combust. Flame 159 (8) (2012) 2589 – 2607. Special Issue on Turbulent Combustion.

[17] J. Kariuki, A. Dowlut, R. Balachandran, E. Mastorakos, Heat release imaging in turbulent premixed ethylene-air flames near blow-off, Flow, Turbul. Combust. 96 (4) (2016) 1039–1051.

[18] B. R. Chowdhury, B. M. Cetegen, Experimental study of the effects of free stream turbulence on characteristics and flame structure of bluff-body stabilized conical lean premixed flames, Combust. Flame 178 (2017) 311 – 328.

[19] R. Yuan, J. Kariuki, A. Dowlut, R. Balachandran, E. Mastorakos, Reaction zone visualisation in swirling spray n-heptane flames, Proc. Combust. Inst. 35 (2) (2015) 1649–1656.

[20] D. E. Cavaliere, J. Kariuki, E. Mastorakos, A Comparison of the Blow-off Behaviour of Swirl-Stabilized Premixed, Non-premixed and Spray Flames, Flow, Turbul. Combust. 91 (2) (2013) 347–372.

[21] A. R. Masri, J. D. Gounder, Turbulent spray flames of acetone and ethanol approaching extinction, Combust. Sci. Technol. 182 (7) (2010) 702–715.

[22] C. K. Law, Combustion Physics, Cambridge University Press, 2006.

[23] S. J. Shanbhogue, S. Husain, T. Lieuwen, Lean Blowoff of Bluff Body Stabilized Flames: Scaling and Dynamics, Prog. Energy Combust. Sci. 35 (1) (2009) 98–120.

[24] J. P. Longwell, E. E. Frost, M. A. Weiss, Flame Stability in Bluff Body Recirculation Zones, Ind. Eng. Chem. 45 (8) (1953) 1629–1633.

[25] S. Yamaguchi, N. Ohiwa, T. Hasegawa, Structure and blow-off mechanism of rod-stabilized premixed flame, Combust. Flame 62 (1) (1985) 31–41.

[26] E. E. Zukoski, "Afterburners ," Aero-thermodynamics of gas turbine and rocket propulsion, edited by G. Oates, AIAA, Reston, VA (1997).

[27] J. Longwell, J. Chenevey, W. Clark, E. Frost, Flame stabilization by baffles in a high velocity gas stream, Symp. Combust. Flame Explos. Phenom. 3 (1) (1948) 40 – 44.

[28] J. Kariuki, Turbulent Premixed Flame Stabilization and Blow-off, University of Cambridge, Ph.D. thesis. (2012).

[29] J. Kariuki, J. R. Dawson, E. Mastorakos, Measurements in Turbulent Premixed Bluff Body Flames Close to Blow-off, Combust. Flame 159 (8) (2012) 2589–2607.

[30] B. Roy Chowdhury, B. M. Cetegen, Experimental study of the effects of free stream turbulence on characteristics and flame structure of bluff-body stabilized conical lean premixed flames, Combust. Flame 178 (2017) 311–328.

[31] S. Chaudhuri, S. Kostka, M. W. Renfro, B. M. Cetegen, Blowoff dynamics of bluff body stabilized turbulent premixed flames, Combust. Flame 157 (4) (2010) 790 – 802.

[32] J. R. Dawson, R. L. Gordon, J. Kariuki, E. Mastorakos, A. R. Masri, M. Juddoo, Visualization of Blow-off Events in Bluff-body Stabilized Turbulent Premixed Flames, Proc. Combust. Inst. 33 (1) (2011) 1559–1566.

[33] J. F. Driscoll, J. H. Chen, A. W. Skiba, C. D. Carter, E. R. Hawkes, H. Wang, Premixed flames subjected to extreme turbulence: Some questions and recent answers, Prog. Energy Combust. Sci. 76 (2020) 100802.

[34] P. Clavin, Dynamic behavior of premixed flame fronts in laminar and turbulent flows, Prog. Energy Combust. Sci. 11 (1) (1985) 1 – 59.

[35] A. Lipatnikov, J. Chomiak, Turbulent flame speed and thickness: phenomenology, evaluation, and application in multi-dimensional simulations, Prog. Energy Combust. Sci. 28 (1) (2002) 1 – 74.

[36] J. Kariuki, A. Dowlut, R. Yuan, R. Balachandran, E. Mastorakos, Heat release imaging in turbulent premixed methane–air flames close to blow-off, Proc. Combust. Inst. 35 (2) (2015) 1443 – 1450.

[37] S. Kheirkhah, Ömer L. Gülder, Consumption speed and burning velocity in counter-gradient and gradient diffusion regimes of turbulent premixed combustion, Combust. Flame 162 (4) (2015) 1422 – 1439.

[38] F. Carbone, J. L. Smolke, A. M. Fincham, F. N. Egolfopoulos, Comparative behavior of piloted turbulent premixed jet flames of C1-C8 hydrocarbons, Combust. Flame 180 (2017) 88 – 101.

[39] J. Trabold, S. Hartl, S. Walther, A. Johchi, A. Dreizler, D. Geyer, Fuel effects in turbulent premixed pre-vaporised alcohol/air jet flames, Flow, Turbul. Combust. (2020).

[40] A. Aspden, J. Bell, M. Day, F. Egolfopoulos, Turbulence–flame interactions in lean premixed dodecane flames, Proc. Combust. Inst. 36 (2) (2017) 2005 – 2016.

[41] A. N. Lipatnikov, J. Chomiak, V. A. Sabelnikov, S. Nishiki, T. Hasegawa, Unburned mixture fingers in premixed turbulent flames, Proc. Combust. Inst. 35 (2) (2015) 1401 – 1408.

[42] T. Edwards, Reference jet fuels for combusion testing, (2017) 100 – 146.

[43] M. Colket, J. Heyne, M. Rumizen, M. Gupta, T. Edwards, W. M. Roquemore, G. Andac, R. Boehm, J. Lovett, R. Williams, J. Condevaux, D. Turner, N. Rizk, J. Tishkoff, C. Li, J. Moder, D. Friend, V. Sankaran, Overview of the national jet fuels combustion program, AIAA Journal 55 (4) (2017) 1087 – 1104.

[44] O. Edenhofer, Special report on renewable energy sources and climate change mitigation: Summary for policymakers and technical summary, Intergovernmental panel on climate change (2011).

[45] Anon., U.S. aviation greenhouse gas emission reduction plan (2015).

[46] M. Dunn, A. Masri, R. Bilger, R. Barlow, G.-H. Wang, The compositional structure of highly turbulent piloted premixed flames issuing into a hot coflow, Proc. Combust. Inst. 32 (2) (2009) 1779 – 1786.

[47] B. Zhou, C. Brackmann, Z. Li, M. Aldén, X.-S. Bai, Simultaneous multi-species and temperature visualization of premixed flames in the distributed reaction zone regime, Proc. Combust. Inst. 35 (2) (2015) 1409 – 1416.

[48] B. Zhou, C. Brackmann, Q. Li, Z. Wang, P. Petersson, Z. Li, M. Aldén, X. song Bai, Distributed reactions in highly turbulent premixed methane/air flames: Part i. flame structure characterization, Combust. Flame 162 (7) (2015) 2937 – 2953.

[49] B. Zhou, C. Brackmann, Z. Wang, Z. Li, M. Richter, M. Aldén, X.-S. Bai, Thin reaction zone and distributed reaction zone regimes in turbulent premixed methane/air flames: Scalar distributions and correlations, Combust. Flame 175 (2017) 220 – 236. Special Issue in Honor of Norbert Peters.

[50] A. W. Skiba, T. M. Wabel, C. D. Carter, S. D. Hammack, J. E. Temme, J. F. Driscoll, Premixed flames subjected to extreme levels of turbulence part i: Flame structure and a new measured regime diagram, Combust. Flame 189 (2018) 407 – 432.

[51] M. J. Dunn, A. R. Masri, R. W. Bilger, A new piloted premixed jet burner to study strong finite-rate chemistry effects, Combust. Flame 151 (1) (2007) 46 – 60.

[52] N. Peters, Turbulent Combustion, Cambridge Monographs on Mechanics, Cambridge University Press, 2000.

[53] DE Cavaliere, Blowoff in Gas Turbine Combustors, June, 2013.

[54] H. M. Nicholson, J. P. Field, Some experimental techniques for the investigation of the mechanism of flame stabilization in the wakes of bluff bodies, Symp. Combust. Flame Explos. Phenom. 3 (1) (1949) 44–68.

[55] K. M. Kundu, D. Banerjee, D. Bhaduri, Theoretical analysis on flame stabilization by a bluff-body, Combust. Sci. Technol. 17 (3-4) (1977) 153–162.

[56] G. C. Williams, H. C. Hottel, A. C. Scurlock, Flame stabilization and propagation in high velocity gas streams, Symp. Combust. Flame Explos. Phenom. 3 (1) (1949) 21–40.

[57] E. A. D. Zubay, Aero Digest 61 (1950) 54–56.

[58] C. R. King, A semi empirical correlation of afterburner combustion efficiency and lean-blowout fuel-air-ratio data with several afterburner-inlet variables and afterburner lengths, NACA RM E57F26 National advisory committee on aeronautics (1957).

[59] D. R. Ballal, A. H. Lefebvre, A weak extinction limits of turbulent heterogeneous fuel/air mixtures, ASME. J. Eng. Power 102 (1980) 416–421.

[60] A. Ateshkadi, V. G. McDonell, G. Samuelsen, Lean blowout model for a spray-fired swirl-stabilized combustor, Proc. Combust. Inst. 28 (1) (2000) 1281 – 1288.

[61] K. Radhakrishnan, J. B. Heywood, R. J. Tabaczynski, Premixed Turbulent Flame Blowoff Velocity Correlation Based on Coherent Structures in Turbulent Flows, Combust. Flame 42 (C) (1981) 19–33.

[62] P. M. Allison, J. A. Sidey, E. Mastorakos, Lean blowoff scaling of swirling, bluff-body stabilized spray flames, AIAA, paper no. 1421 (2018).

[63] N. Rock, B. Emerson, J. Seitzman, T. Lieuwen, Near lean blowoff dynamics in a liquid fueled combustor, Combust. Flame 212 (2020) 53 – 66.

[64] S. Stouffer, T. Hendershott, J. R. Monfort, J. Diemer, E. Corporan, P. Wrzesinski, A. W. Caswell, Lean blowout and ignition characteristics of conventional and surrogate fuels measured in a swirl stabilized combustor, 55th AIAA (2017).

[65] D. Shin, A. J. Bokhart, N. S. Rodrigues, P. E. Sojka, J. P. Gore, R. P. Lucht, Nonreacting spray characteristics for alternative aviation fuels at near-lean blowout conditions, J. Propuls. Power 36 (3) (2020) 323–334.

[66] J. Trabold, S. Hartl, S. Walther, A. Johchi, A. Dreizler, D. Geyer, Fuel Effects in Turbulent Premixed Pre-vaporised Alcohol/Air Jet Flames, Flow, Turbul. Combust. (2020).

[67] N. Peters, Laminar diffusion flamelet models in non-premixed turbulent combustion, Prog. Energy Combust. Sci. 10 (1984).

[68] N. Peters, Laminar flamelet concepts in turbulent combustion, Symp Combust Proc 21 (1) (1988) 1231–1250.

[69] M. J. Russi, I. Cornet, R. Cornog, The influence of flame holder temperature on flame stabilization, Symp Combust Proc 4 (1) (1953) 743–748.

[70] F. Wright, Bluff-body flame stabilization: Blockage effects, Combust. Flame 3 (1959) 319–337.

[71] F. Filippi, L. Fabbrovich-Mazza, Control of bluff-body flameholder stability limits, Symp Combust Proc 8 (1) (1961) 956–963.

[72] G. Winterfeld, On processes of turbulent exchange behind flame holders, Symp Combust Proc 10 (1) (1965) 1265–1275.

[73] R. Pein, H. Peschel, F. Fetting, Recirculation zone concentrations and temperatures of bluff-body stabilized turbulent flames, Combust. Sci. Technol. 1 (4) (1970) 327–330.

[74] P. Walburn, Activation energies in a baffle stabilized flame, Combust. Flame 12 (6) (1968) 550–556.

[75] S. Yamaguchi, N. Ohiwa, T. Hasegawa, Structure and blow-off mechanism of rod-stabilized premixed flame, Combust. Flame 62 (1) (1985) 31 – 41.

[76] S. Nair, T. C. Lieuwen, Near-blowoff dynamics of a bluff-body stabilized flame, J. Propuls. Power 23 (2) (2007).

[77] S. Chaudhuri, S. Kostka, S. G. Tuttle, M. W. Renfro, B. M. Cetegen, Blowoff mechanism of two dimensional bluff-body stabilized turbulent premixed flames in a prototypical combustor, Combust. Flame 158 (7) (2011) 1358 – 1371.

[78] S. Chaudhuri, B. M. Cetegen, Blowoff characteristics of bluff-body stabilized conical premixed flames with upstream spatial mixture gradients and velocity oscillations, Combust. Flame 153 (4) (2008) 616 – 633.

[79] S. Chaudhuri, S. Kostka, S. Tuttle, M. Renfro, B. Cetegen, Blowoff dynamics of V-shaped bluff body stabilized, turbulent premixed flames in a practical scale rig, 48th AIAA (January) (2010) 2010.

[80] B. R. Chowdhury, B. M. Cetegen, Effects of fuel properties and free stream turbulence on characteristics of bluff-body stabilized flames, Combust. Flame 194 (2018) 206 – 222.

[81] T. Poinsot, D. Veynante, Theoretical and numerical combustion, 2001.

[82] S. Kheirkhah, L. Gülder, Turbulent premixed combustion in v-shaped flames: Characteristics of flame front, Phys. Fluids 25 (5) (2013) 055107.

[83] P. Tamadonfar, Ö. L. Gülder, Flame brush characteristics and burning velocities of premixed turbulent methane/air Bunsen flames, Combust. Flame 161 (12) (2014) 3154–3165.

[84] G. V. Nivarti, R. S. Cant, Scalar transport and the validity of damköhler's hypotheses for flame propagation in intense turbulence, Phys. Fluids 29 (8) (2017) 085107.

[85] E. Hawkes, R. Cant, A flame surface density approach to large-eddy simulation of premixed turbulent combustion, Proc. Combust. Inst. 28 (1) (2000) 51 – 58.

[86] I. Shepherd, Flame surface density and burning rate in premixed turbulent flames, Symp Combust Proc 26 (1) (1996) 373 – 379.

[87] A. Aspden, A numerical study of diffusive effects in turbulent lean premixed hydrogen flames, Proc. Combust. Inst. 36 (2) (2017) 1997 – 2004.

[88] A. Aspden, M. Day, J. Bell, Turbulence-chemistry interaction in lean premixed hydrogen combustion, Proc. Combust. Inst. 35 (2) (2015) 1321 – 1329.

[89] B. Savard, B. Bobbitt, G. Blanquart, Structure of a high karlovitz n-c7h16 premixed turbulent flame, Proc. Combust. Inst. 35 (2) (2015) 1377 – 1384.

[90] A. Aspden, M. Day, J. Bell, Lewis number effects in distributed flames, Proc. Combust. Inst. 33 (1) (2011) 1473 – 1480.

[91] B. Savard, G. Blanquart, Effects of dissipation rate and diffusion rate of the progress variable on local fuel burning rate in premixed turbulent flames, Combust. Flame 180 (2017) 77 – 87.

[92] P. D. Ronney, V. Yakhot, Flame broadening effects on premixed turbulent flame speed, Combust. Sci. Technol. 86 (1-6) (1992) 31–43.

[93] M. S. Mansour, N. Peters, Y.-C. Chen, Investigation of scalar mixing in the thin reaction zones regime using a simultaneous ch-lif/rayleigh laser technique, Symp Combust Proc 27 (1) (1998) 767–773.

[94] S. G. Davis, C. Law, Determination of and fuel structure effects on laminar flame speeds of c1 to c8 hydrocarbons, Combust. Sci. Technol. 140 (1-6) (1998) 427–449.

[95] X. You, F. N. Egolfopoulos, H. Wang, Detailed and simplified kinetic models of n-dodecane oxidation: The role of fuel cracking in aliphatic hydrocarbon combustion, Proc. Combust. Inst. 32 (1) (2009) 403 – 410.

[96] F. Dinkelacker, A. Soika, D. Most, D. Hofmann, A. Leipertz, W. Polifke, K. Döbbeling, Structure of locally quenched highly turbulent lean premixed flames, Symp Combust Proc 27 (1) (1998) 857 – 865.

[97] Y.-C. Chen, R. W. Bilger, Experimental investigation of three-dimensional flame-front structure in premixed turbulent combustion—i: hydrocarbon/air bunsen flames, Combust. Flame 131 (4) (2002) 400 – 435.

[98] S. Lapointe, B. Savard, G. Blanquart, Differential diffusion effects, distributed burning, and local extinctions in high karlovitz premixed flames, Combust. Flame 162 (9) (2015) 3341 – 3355.

[99] S. Lapointe, G. Blanquart, Fuel and chemistry effects in high karlovitz premixed turbulent flames, Combust. Flame 167 (2016) 294 – 307.

[100] J. Kariuki, A. Dowlut, R. Yuan, R. Balachandran, E. Mastorakos, Heat release imaging in turbulent premixed methane-air flames close to blow-off, Proc. Combust. Inst. 35 (2) (2015) 1443–1450.

[101] J. Griffiths, S. Scott, Thermokinetic interactions: Fundamentals of spontaneous ignition and cool flames, Prog. Energy Combust. Sci. 13 (3) (1987) 161 – 197.

[102] M. J. Dyer, D. R. Crosley, Two-dimensional imaging of oh laser-induced fluorescence in a flame, Opt. Lett. 7 (8) (1982) 382–384.

[103] E. P. Hassel, S. Linow, Laser diagnostics for studies of turbulent combustion, Meas. Sci. Technol. 11 (2) (2000) R37–R57.

[104] N. T. Clemens, Flow imaging, (2002) 390–419.

[105] G. H. Wang, N. T. Clemens, Effects of imaging system blur on measurements of flow scalars and scalar gradients, Exp. Fluids 37 (2) (2004) 194–205.

[106] M. J. Papageorge, T. A. McManus, F. Fuest, J. A. Sutton, Recent advances in high-speed planar Rayleigh scattering in turbulent jets and flames: increased record lengths, acquisition rates, and image quality, Applied Physics B 115 (2) (2014) 197–213.

[107] H. N. Najm, P. H. Paul, C. J. Mueller, P. S. Wyckoff, On the Adequacy of Certain Experimental Observables as Measurements of Flame Burning Rate, Combust. Flame 113 (3) (1998) 312–332.

[108] C. A. Fugger, S. Roy, A. W. Caswell, B. A. Rankin, J. R. Gord, Structure and dynamics of ch2o, oh, and the velocity field of a confined bluff-body premixed flame, using simultaneous plif and piv at 10khz., Proc. Combust. Inst. 37 (2) (2019) 1461 – 1469.

[109] J. Rosell, X.-S. Bai, J. Sjoholm, B. Zhou, Z. Li, Z. Wang, P. Pettersson, Z. Li, M. Richter, M. Alden, Multi-species plif study of the structures of turbulent premixed methane/air jet flames in the flamelet and thin-reaction zones regimes, Combust. Flame 182 (2017) 324 – 338.

[110] C. Brackmann, J. Nygren, X. Bai, Z. Li, H. Bladh, B. Axelsson, I. Denbratt, L. Koopmans, P.-E. Bengtsson, M. Aldén, Laser-induced fluorescence of formaldehyde in combustion using third harmonic nd:yag laser excitation, SAA 59 (14) (2003) 3347 – 3356.

[111] Z. Li, B. Li, Z. Sun, X. Bai, M. Aldén, Turbulence and combustion interaction: High resolution local flame front structure visualization using simultaneous single-shot plif imaging of ch, oh, and ch2o in a piloted premixed jet flame, Combust. Flame 157 (6) (2010) 1087–1096.

[112] M. Orain, P. Baranger, C. Ledier, J. Apeloig, F. Grisch, Fluorescence spectroscopy of kerosene vapour at high temperatures and pressures: potential for gas turbines measurements, Appl. Phys. B 116 (3) (2014) 729–745.

[113] H. N. Najm, O. M. Knio, P. H. Paul, P. Wyckoff, A study of flame observables in premixed methane - air flames, Combust. Sci. Technol. 140 (1-6) (1998) 369–403.

[114] T. M. Wabel, A. W. Skiba, J. F. Driscoll, Turbulent burning velocity measurements: Extended to extreme levels of turbulence, Proc. Combust. Inst. 36 (2) (2017) 1801 – 1808.

[115] I. E. Helou, A. Skiba, E. Mastorakos, J. A. Sidey, Investigation of the effect of dilution air on soot production and oxidation in a lab scale Rich-Quench-Lean (RQL) burner.

[116] J. A. M. Sidey, P. M. Allison, E. Mastorakos, The effect of fuel composition on swirling kerosene flames (January) (2017) 1–8.

[117] J. B. Bell, M. S. Day, J. F. Grcar, M. J. Lijewski, J. F. Driscoll, S. A. Filatyev, Numerical simulation of a laboratory-scale turbulent slot flame, Proc. Combust. Inst. 31 (1) (2007) 1299 – 1307.

[118] D. Veynante, G. Lodato, L. Vervisch, R. Hawkes, E., Estimation of three-dimensional flame surface densities from planar images in turbulent premixed combustion, Exp Fluids 57 (2010) 267–278.

[119] M. Haq, C. Sheppard, R. Woolley, D. Greenhalgh, R. Lockett, Wrinkling and curvature of laminar and turbulent premixed flames, Combustion and Flame 131 (1) (2002) 1–15.

[120] M. Papageorge, J. Sutton, Statistical processing and convergence of finite-record-length time-series measurements from turbulent flows, Exp Fluids 57 (2016).

[121] D. G. Goodwin, H. K. Moffat, R. L. Speth, Cantera: An Object-oriented Software Toolkit for Chemical Kinetics, Thermodynamics, and Transport Processes. Version 2.2.1, 2016.

[122] H. Wang, X. You, A. V. Joshi, S. G. Davis, A. Laskin, F. Egolfopoulos, C. K. Law, Usc mech version II. high-temperature combustion reaction model of h2/co/c1-c4 compounds (May, 2007).

[123] N. M. Marinov, A detailed chemical kinetic model for high temperature ethanol oxidation, Int. J. Chem. Kinet. 31 (3) (1999) 183–220.

[124] A. Smallbone, W. Liu, C. Law, X. You, H. Wang, Experimental and modeling study of laminar flame speed and non-premixed counterflow ignition of n-heptane, Proc. Combust. Inst. 32 (1) (2009) 1245 – 1252.

[125] H. Wang, R. Xu, K. Wang, C. T. Bowman, R. K. Hanson, D. F. Davidson, K. Brezinsky, F. N. Egolfopoulos, A physics-based approach to modeling real-fuel combustion chemistry - i. evidence from experiments, and thermodynamic, chemical kinetic and statistical considerations, Combust. Flame 193 (2018) 502 – 519.

[126] K. Wang, R. Xu, T. Parise, J. Shao, A. Movaghar, D. J. Lee, J.-W. Park, Y. Gao, T. Lu, F. N. Egolfopoulos, D. F. Davidson, R. K. Hanson, C. T. Bowman, H. Wang, A physics-based approach to modeling real-fuel combustion chemistry – IV. HyChem modeling of combustion kinetics of a bio-derived jet fuel and its blends with a conventional jet A, Combust. Flame (2018).

[127] A. W. Lefebvre, D. R. Ballal, Gas turbine combustion-Alternative fuels and emissions, CRC press, Taylor and Francis group, NY, 2010.

[128] D. C. Kyritsis, V. S. Santoro, A. Gomez, The effect of temperature correction on the measured thickness of formaldehyde zones in diffusion flames for 355 nm excitation, Exp. Fluids 37 (5) (2004) 769–772.

[129] B. Coriton, J. H. Frank, A. Gomez, Interaction of turbulent premixed flames with combustion products: Role of stoichiometry, Combust. Flame 170 (2016) 37 – 52.

[130] A. Steinberg, B. Coriton, J. Frank, Influence of combustion on principal strain-rate transport in turbulent premixed flames, Proc. Combust. Inst. 35 (2) (2015) 1287 – 1294.

[131] S. Popp, F. Hunger, S. Hartl, D. Messig, B. Coriton, J. H. Frank, F. Fuest, C. Hasse, Les flamelet-progress variable modeling and measurements of a turbulent partially-premixed dimethyl ether jet flame, Combust. Flame 162 (8) (2015) 3016 – 3029.

[132] R. Barlow, J. Frank, Effects of turbulence on species mass fraction in methane/air jet flames, Symp Combust Proc 27 (1998) 1087–1095.

[133] P. Versailles, G. M. Watson, A. C. Lipardi, J. M. Bergthorson, Quantitative ch measurements in atmospheric-pressure, premixed flames of c1–c4 alkanes, Combust. Flame 165 (2016) 109 – 124.

[134] H. N. Najm, O. M. Knio, P. H. Paul, P. Wyckoff, A study of flame observables in premixed methane - air flames, Combust. Sci. Technol. 140 (1-6) (1998) 369–403.

[135] R. Borghi, On the structure and morphology of turbulent premixed flames, (1989) 117 – 138.

[136] R. Abdel-Gayed, D. Bradley, Criteria for turbulent propagation limits of premixed flames, Combust. Flame 62 (1) (1985) 61 – 68.

[137] R. Abdel-Gayed, D. Bradley, F. K. K. Lung, Combustion regimes and the straining of turbulent premixed flames, Combust. Flame 76 (1) (1989) 213 – 218.

[138] C. Law, Dynamics of stretched flames, Symp Combust Proc 22 (1) (1989) 1381 – 1402.

[139] W. Liang, R. Mével, C. K. Law, Role of low-temperature chemistry in detonation of n-heptane/oxygen/diluent mixtures, Combust. Flame 193 (2018) 463 – 470.

[140] B. O. Ayoola, R. Balachandran, J. H. Frank, E. Mastorakos, C. F. Kaminski, Spatially resolved heat release rate measurements in turbulent premixed flames, Combust. Flame 144 (1-2) (2006) 1–16.

[141] A. W. Skiba, T. F. Guiberti, W. R. Boyette, W. L. Roberts, E. Mastorakos, On the bi-stable nature of turbulent premixed bluff-body stabilized flames at elevated pressure and near lean blow-off (accepted), Proc. Combust. Inst. (2020).

[142] A. Lipatnikov, J. Chomiak, Molecular transport effects on turbulent flame propagation and structure, Prog. Energy Combust. Sci. 31 (1) (2005) 1 – 73.

[143] J. C. Massey, I. Langella, N. Swaminathan, A scaling law for the recirculation zone length behind a bluff body in reacting flows, J. Fluid Mech. 875 (2019).

[144] S. B. Pope, Turbulent flows, Measurement Science and Technology 12 (11) (2001) 2020–2021.

[145] E. Mastorakos, A. Taylor, J. Whitelaw, Extinction of turbulent counterflow flames with reactants diluted by hot products, Combust. Flame 102 (1) (1995) 101 – 114.

[146] A. W. Skiba, C. D. Carter, S. D. Hammack, J. D. Miller, J. R. Gord, J. F. Driscoll, The influence of large eddies on the structure of turbulent premixed flames characterized with stereo-piv and multi-species plif at 20khz, Proc. Combust. Inst. 37 (2) (2019) 2477 – 2484.

[147] A. Aspden, M. Day, J. Bell, Three-dimensional direct numerical simulation of turbulent lean premixed methane combustion with detailed kinetics, Combust. Flame 166 (2016) 266 – 283.

Appendix A

Video

A sample video of the blow-off mechanism captured with OH* chemiluminescence, OH- and Fuel-PLIF is complied in a single video and can be access by the following link:

https://vimeo.com/519605314

The video consist of three parts:

Part I: Blow-off event with OH* chemiluminescence
Shows the sequence of images for the last 30 s of the blow-off event with A2. The images were taken at 5.4 kHz, and the video is played 5 frames/s.

Part III: Blow-off event with OH-PLIF
Shows the sequence of images for the last 60 s of the blow-off event with A2. The images were taken at 5.0 kHz, and the video is played 5 frames/s.

Part III: Blow-off event with Fuel-PLIF
Shows the sequence of images for the last 60 s of the blow-off event with A2. The images were taken at 5.0 kHz, and the video is played 5 frames/s.